

Copyright

by

Hui Dong

2018

**The Dissertation Committee for Hui Dong Certifies that this is the approved version
of the following Dissertation:**

**Ultra-stable nano-manipulation of mechanically-variable system:
optical forces and beyond**

Committee:

Zheng Wang, Supervisor

Edward Yu

Keji Lai

Neal A. Hall

Nanshu Lu

**Ultra-stable nano-manipulation of mechanically-variable system:
optical forces and beyond**

by

Hui Dong

Dissertation

Presented to the Faculty of the Graduate School of

The University of Texas at Austin

in Partial Fulfillment

of the Requirements

for the Degree of

DOCTOR OF PHILOSOPHY

The University of Texas at Austin

December 2018

Dedication

Dedicated to my family.

Acknowledgements

Firstly, I would like to express my wholehearted gratitude to my supervisor, Prof. Zheng Wang, for his continuous support and instruction of my Ph.D. research and related cooperation with other research groups. Without his immense knowledge, patience, and guidance, I could not find the viable ways to my goals in the area of numerical simulation and scientific computing.

Besides my supervisor, I would like to express my thanks to the rest of my committee: Prof. Edward Yu, Prof. Nanshu Lu, Prof. Keji Lai, and Prof. Neal Hall, for their encouragement and insightful comments on my research. Their valuable questions also incited me to widen my research from various other perspectives. The cooperation and discussions with them greatly broaden my skill set which will definitely benefit me in my future career development.

My sincere thanks also go to Prof. Edward Powers, Prof. Brian Evans, Prof. Julian Cheng, Prof. Aristotle Arapostathis and Dr. David Brown for picking me as the teaching assistant of their classes. I would like to thank Prof. Ahmed Tewfik and Prof. Jack Lee for their attention on my research progress. Also, I want to express my thanks to Dr. Hossein Mousavi, Dr. Ian Williamson, Dr. Thien-an Nguyen, Lu Zheng, Yifu Huang, Dr. Xiaoyu Wu, and Dr. Di Wu for their collaboration on the research. There are also too many other people I want to express my thanks to, I would like to give my deep appreciation to all the people helping me during my internships, all the classmates discussing with me on the projects, all the PhDs who acknowledged me in their dissertations, and all the friends along with me these years.

Finally, but the most importantly, without the strong backup support from my family, especially my parents, I could not persist until now. They teach me to be strong, kind, earnest and responsible.

Abstract

Ultra-stable nano-manipulation of mechanically-variable system: optical forces and beyond

Hui Dong, Ph.D.

The University of Texas at Austin, 2018

Supervisor: Zheng Wang

Optical force and acoustic force have been intensively investigated over the past several decades in the applications ranging from the optical/acoustic trapping, high-resolution biomedical imaging, sensing technology, signal processing to acoustic levitation, ultrasonic calibration, etc.

I started from the calculation of the optical force including both radiation pressure and electrostriction force in stimulated Brillouin scattering using finite-element method. Then I investigated the sufficient condition of creating conservative optical force field, which is hard to realize as the optical force generally contains inevitable rotational component in a multi-port system. To verify the conclusion, this condition has been subsequently applied to three scenarios, realizing auto-alignment of millimeter-scale photonic crystal slabs, simultaneously trapping and orientating nano-particles, and self-aligned topological photonic crystal. To overcome the material loss which breaks the conservativeness of the optical force, a compensating method using the gain media to recover the conservative optical force field is presented and verified by the vorticity ratio derived from Helmholtz-Hodge decomposition (HHD).

As an analog to the optical radiation pressure but generally millions larger in magnitude, the acoustic radiation pressure calculation using the response theory is also proposed, which perfectly agrees with the traditional Reynold stress tensor integration and, more importantly, reveals the sufficient condition of conservative acoustic force.

The contributions of this work are significant in four aspects in the area of numerical device simulation and parallel scientific computing: first of all, it paves the fundamental way to ultra-stable trapping by providing correct ways of numerically calculating optical/acoustic forces, which are corroborated by response theory developed in this work; secondly, the complete temporal coupled-mode theory unveils all spectral response of waveguide-resonator systems; thirdly, the parallel algorithm of HHD applied to periodic structure provides reliable metric to evaluate stability of trapping; finally, the newly developed weak-form formulation of topological photonic crystal with loss/gain helps design of novel photonic devices.

Table of Contents

Acknowledgments	v
Abstract	vii
List of Figures	xiv
Chapter 1. Introduction	1
1.1 Background	1
1.2 Motivation	2
1.2.1 Full vectorial calculation of the optical force	2
1.2.2 Sufficient condition of conservative optical/acoustic force	3
1.2.3 Response theory of acoustic force	4
1.3 Contributed work	4
1.3.1 Full vectorial calculation of SBS gain in nano-scale sus- suspended silicon waveguide	4
1.3.2 Conservative optical force in stacking photonic crystal slabs	5
1.3.3 Trapping and orientating nano-particles in one-way wave- guide	6
1.3.4 Self-aligned topological photonic crystal	7
1.3.5 Compensating loss in one-way waveguide	7
1.3.6 Auto-alignment of phononic crystal using acoustic force	8
1.4 Future work	8
1.4.1 Self-aligned topological photonic crystal with frequency modulation	8
1.4.2 Two-dimensional acoustic trap	9

Chapter 2. General framework of stimulated Brillouin scattering gain coefficient calculation in nano-scale systems	10
2.1 Stimulated Brillouin scattering in nano-scale systems	10
2.2 Calculating the SBS gain via overlap integral	12
2.2.1 General SBS gain induced by optical force	12
2.2.2 SBS gain of each elastic eigen-mode	13
2.3 Radiation pressure on discontinuous boundaries	16
2.3.1 General MST in homogeneous material	16
2.3.2 Decomposition of MST on discontinuous boundaries . .	17
2.4 Electrostrictive force in bulk and on boundaries	19
2.5 SBS gain coefficient in suspended silicon waveguide system . .	21
2.5.1 Optical and elastic eigen-modes in suspended rectangular silicon waveguide	22
2.5.2 Intra-modal coupling versus Inter-modal coupling	23
2.6 Concluding remarks	29
Chapter 3. Self-alignment of millimeter-scale photonic crystal slabs with sub-nanometer resolution	30
3.1 Automatic self-alignment technologies using optical forces . . .	30
3.1.1 Brief overview of optical manipulation techniques	31
3.1.2 The advantage of conservative optical force	31
3.1.3 Organization of this chapter	33
3.2 Conservative optical force established in stacked photonic crystal slabs system	35
3.2.1 One-port system guaranteeing conservative optical forces	35
3.2.2 Port number in various stacking photonic crystal slabs systems	40
3.2.3 Inevitable non-conservative optical force in multi-port system	45
3.2.4 Tailoring conservative optical force field established in one-port system	48
3.3 Quantification of conservativeness of optical force via Helmholtz-Hodge decomposition	54
3.3.1 Introduction to Helmholtz-Hodge decomposition	55

3.3.2	Helmholtz-Hodge decomposition using Green's function method	56
3.3.3	Uniqueness of Helmholtz-Hodge decomposition of periodic vector field	58
3.3.4	Error convergence of Helmholtz-Hodge decomposition	59
3.4	Computation Concerns	64
3.5	Conclusion Remarks	66
Chapter 4. Novel optical trapping in topological photonic integrated system		68
4.1	Introduction	68
4.2	Simultaneously trapping and orientation of asymmetric particle in unidirectional waveguide-resonator system	69
4.2.1	Conservative optical force in unidirectional waveguide-resonator system	69
4.2.2	Trapping the particle	74
4.2.3	Orientating the particle	75
4.2.4	Tuning the resolution of the optical trap	78
4.3	Vorticity residual in one-port and two-port system	80
4.4	Conclusion remarks	83
Chapter 5. Compensating material loss in topological one-way waveguide		86
5.1	Introduction	86
5.2	Compensating the material lossy using active medium	87
5.2.1	Weak-form formula for topological waveguide	90
5.2.2	Complex dispersion relation of lossy one-way waveguide with loss compensation	91
5.3	Recovering force conservativeness using active media	93
5.3.1	Choosing active medium for the operating frequency	95
5.3.2	Reduction of vorticity ratio with appropriate active medium	97
5.4	Conclusion remarks	101

Chapter 6. Self-aligned topological photonic crystals	102
6.1 Introduction	102
6.2 Mode profiles in topological photonic crystal with honeycomb lattice	103
6.2.1 K-group rods and K'-group rods in row-by-row fabrication procedures	104
6.2.2 Edge-mode profiles of boundary rods of K-group and K'-group	104
6.2.3 Self-assembled bulk-mode profile	106
6.3 RTOF based on phase response as a function of floquet wave vector	110
6.3.1 Spatial phase response derived from floquet wave vector	110
6.3.2 Optical force exerted by edge topological modes	118
6.3.3 Optical force exerted by “perfect” bulk modes	119
6.4 Force potential as a function of operating frequencies for bulk modes	122
6.5 Conclusion remarks	125
Chapter 7. Acoustic trapping of phononic crystal slabs	127
7.1 Introduction	127
7.2 Response theory of acoustic force – RTAF	128
7.2.1 Reynold stress tensor: traditional way of calculating the acoustic radiation pressure	129
7.2.2 Agreement between RTAF and Reynold stress tensor . .	130
7.3 Conservative acoustic force in single-port system	133
7.3.1 Phase response predicted by temporal coupled mode theory	137
7.3.2 System characterization using temporal coupled mode theory	139
7.3.3 Realization of 1D acoustic trapping along the longer side of phononic crystal unit cell	139
7.4 Computation Concerns	143
7.5 Conclusion Remarks	143
Appendices	145

Appendix A. General stress tensor expressions in COMSOL	146
A.1 General Maxwell Stress Tensor in COMSOL	146
A.2 General Reynold Stress Tensor in COMSOL	148
Appendix B. Time reversal symmetry	150
Appendix C. Upper limit of truncation error in periodic Helmholtz-Hodge decomposition	153
Appendix D. Weak-form formula for electromagnetic fields	156
D.1 Weak form for E-field	156
D.2 Weak form for H-field	157
Appendix E. MATLAB codes for HHD	160
E.1 Sequential program	160
E.2 Parallel program	163
Appendix F. Parallel HHD in C++ using OpenMP and MPI	168
F.1 Head File	168
F.2 Class File	171
F.3 Main File	181
Bibliography	189
Vita	202

List of Figures

2.1	<p>Typical SBS process in guided-wave system. (a) Energy level of the stimulated Brillouin scattering process, where ω_p, ω_s, and Ω are angular frequencies of pump photon, Stokes photon, and phonon. (b) Phase matching condition of forward SBS process, and (c) Phase matching condition of backward SBS process, where k_p, k_s, and K are wave number of pump wave, Stokes wave, and acoustic wave.</p>	12
2.2	<p>The guided optical and elastic modes of a silicon rectangular waveguide. Optical frequency is in unit of $2\pi c/a$, while elastic frequency is in unit of $2\pi V_L/a$. $V_L = \sqrt{E/\rho} = 8.54 \times 10^3 \text{m/s}$ is the velocity of longitudinal elastic waves in bulk silicon. (a) Dispersion relation of optical modes E_{y11} and E_{z11}. (b) Dispersion relation of elastic modes which have even symmetry with respect to both $y = 0$ and $z = 0$ planes. E-modes (black lines) are the eigen-modes of the actual silicon waveguide, with silicon-air interfaces treated as free boundaries. For comparison, the dispersion relations of purely longitudinal modes (designated as P-modes, blue curves) and purely transverse modes (designated as P-modes, red curves) are included. They are constrained respectively with x-only displacement, and y-z-only movements. At $q = 0$, E-modes manifest as either P-modes or S-modes. (c) The displacement profiles of mode E1 through E5 at $q = 0$, with the peak deformation shown. The color represents y-displacement (u_y) for S-like E modes and x-displacement(u_x) for P-like E modes. Blue, white, and red correspond to negative, zero, and positive values respectively. Mode E1 experience a DC longitudinal offset at $\Omega = 0$.</p>	24

- 2.3 Optical force distributions and the resultant gain coefficients of the Forward SBS. In panels (a) and (b), the width of the waveguide is $a = 315\text{nm}$, and the incident optical waves have $\omega = 0.203(2\pi c/a)$, and $k = 0.75(\pi/a)$. The elastic waves are generated at $q = 0$. (a) The force distribution of electrostriction body force density, electrostriction surface pressure, and radiation pressure respectively. All three types of optical forces are transverse. (b) Calculated FSBS gains of the elastic modes, assuming mechanical $Q = 1000$. Blue, red, and green bars represent FSBS gains under three conditions: electrostriction-only, radiation-pressure-only, and the combined effects. Only the S-like E modes have non-zero gains. (c) The scaling relation of FSBS gains as the device dimension a is varied from $0.25\mu\text{m}$ to $2.5\mu\text{m}$. Solid and dotted curves correspond to the gain coefficients for mode E2 and E5 respectively. 25
- 2.4 Optical force distributions and the resultant gain coefficients of the Backward SBS. In panels (a) and (b), the width of the waveguide is $a = 315\text{nm}$, and the incident optical waves have $\omega = 0.203(2\pi c/a)$, and $k = 0.75(\pi/a)$. The elastic waves are generated at $q = 1.5(\pi/a)$. (a) The force distribution of electrostriction body force density, electrostriction surface pressure, and radiation pressure respectively. Electrostriction have both longitudinal and transverse components. Radiation pressure are purely transverse. (b) Calculated BSBS gains of the elastic modes, assuming mechanical $Q = 1000$. Blue, red, and green bars represent BSBS gains under three conditions: electrostriction-only, radiation-pressure-only, and the combined effects.(c) The scaling relation of BSBS gains related to mode E1 as a is varied from $0.25\mu\text{m}$ to $2.5\mu\text{m}$. Gain coefficients predicted by conventional fiber BSBS theory are shown as the solid black curve. The dotted black curve represents the electrostriction-only BSBS gain of mode P1. Black circles represent the largest electrostriction-only BSBS gain coefficient among all E-modes for a given a . (d) BSBS spectra near the anti-crossing between mode E4 and E5 around $q = 1.66(\pi/a)$. The mechanical quality factor Q is assumed to be 100. The red lines represent the total BSBS gain. The blue and green lines represent contributions from mode E4 and E5. 26

2.5	Optical force distributions, relevant elastic modes, and the resultant gain coefficients of inter-modal FSBS between E_{y11} (pump) and E_{z11} (Stokes). The width of the waveguide is set to be $a = 315\text{nm}$. The incident optical waves have $\omega = 0.203(2\pi c/a)$, with the pump-wave propagation constant at $k_p = 0.750(\pi/a)$, and the Stokes-wave propagation constant at $k_s = 0.665(\pi/a)$. The elastic waves are generated at $q = 0.085(\pi/a)$. (a) The force distribution of electrostriction body force density, electrostriction surface pressure, and radiation pressure respectively. The longitudinal forces (not shown here) are negligible, in comparison to the transverse forces. All optical forces are anti-symmetric with respect to plane $y = 0$ and plane $z = 0$, exciting elastic modes with the matching symmetry (designated as O-modes). (b) Calculated inter-modal SBS gains, assuming mechanical $Q = 1000$. The insets illustrate the displacement profiles of mode O1 through O5 at $q = 0.085(\pi/a)$, at peak deformation. "Jet" colormap is used to show the amplitude of <i>total</i> displacement. Blue and red correspond to zero and maximum respectively.	28
3.1	(a) Schematics of two photonic crystal slabs (a dielectric one shown in yellow and a metallic one shown in grey) to be self-aligned optically in the xy-plane. The incident light is a plane wave from the top along z-direction, and travels through a polarizing reflector (shown in blue). (b) Calculated optical force (x-component) on the upper photonic crystal slab and (c) the negative phase response of the reflection, as a function of its displacement along x direction as shown in the inset. Y-displacement is set to be 0	38
3.2	Polarization rotation happening in stacking photonic crystal slabs at resonances. (a) The top and bottom slabs (inset) are both made of silicon with $\epsilon_r = 12.25$, and with identical thickness of $0.55a$ and air holes with radius of $0.1a$, where a is the lattice constant. The incident plane wave has polarization along x-direction, and the sum of reflection and transmission polarized along x-direction is calculated in finite-element method when x-displacement = $0.11a$ and y-displacement = $0.17a$, which is less than 1 when polarization rotation happens as a result of coupling between resonant modes and propagating modes. (b) perfect agreement between finite-element calculation and 4-port coupled-mode theory in computing transmission coefficient along x-polarization.	42

3.3	Calculated phase spectra of the reflected light at three lateral offsets: $(0a, 0a)$ (blue), $(0.5a, -0.7a)$ (green), and $(0.25a, -0.35a)$ (red). Insets show the relative positions of the two photonic crystal slabs. Results from first-principle finite-element calculations (dots) are fitted to the coupled-mode theory (curves). .	49
3.4	Calculated displacement-dependent resonance frequency, decay rate and phase response (optical potential) (a-d) Resonant frequency ω and decay rate γ for Mode A and B as a function of the x-y displacement of the upper photonic crystal slab. The frequency contour of frequency of $0.3762(c/a)$ is plotted in yellow in (a) with corresponding decay rates in yellow in (b). The cyan frequency contour in (a) corresponds to frequency of $0.3781(c/a)$ with the corresponding decay rates in cyan as well in (b). The frequency contour of $0.3807(c/a)$ is plotted in cyan in (c) with corresponding decay rates plotted in cyan in (d). (e) (g) Corresponding phase response of the reflection for frequencies of $0.3762(c/a)$, $0.3781(c/a)$, and $0.3807(c/a)$	51
3.5	Decomposed curl-free potential Φ and divergence-free potential Ψ for conservative optical force and non-conservative optical force, and error convergence plot with respect to resolution m on longer side $[0, b]$ and truncation period N , respectively. (a)-(b) Decomposed potentials for conservative optical force in one-port system, and the divergence-free potential is almost flat when plotted in the same scale as non-conservative optical force in system without polarizer. (c)-(d) Decomposed potentials for non-conservative optical force with truncation period=20, and the vortex is obvious on divergence-free potential; (e) Error convergence with respect to number of grids on longer side in log-log scale. Due to existence of relatively large truncation error, both errors stop decreasing at the magnitude of truncation error. (f) Error convergence with respect to truncation period in log-log scale with resolution $m=3000$. Obviously, the error of conservative case linearly decrease with increasing truncation period.	63

4.1	Trapping and orientating an L-shaped particle using resonator-enhanced conservative optical force in a single-port system. The single-port condition is realized by the single-mode one-way waveguide which is formed between the metal wall and the magnetized (+z) YIG photonic crystals (light blue). The light is coupled from the one-way waveguide to the square metal-box resonator (inset) through a small gap opened on the domain wall. The side length of the resonator is chosen to be $1.16a$ to ensure the resonant frequency always falls into the band gap of magneto-optical photonic crystal wherever L-shaped particle moves and orients. The rotation angle is defined as the angle between longer side of L-shaped particle and y-axis anticlockwise (inset).	70
4.2	Trajectories of 10 trials of releasing L-shaped particle at 10 different initial locations at $x = (0.1a, 0.3a, 0.5a, 0.7a, 0.9a)$ and $y = (0.1a, 0.9a)$ (the orientation of particle is always kept at 0°). The L-shaped particle has a permittivity of 6.25, and a longer side of $0.0667a$ and a shorter side of $0.0333a$. Four snapshots of particle locations (black dots) at $t = 0ms$, $t = 0.1ms$, $t = 0.5ms$, and $t = 3ms$ are shown in (a)–(d) (the dynamic viscosity is set to be $10^{-6} Pa \cdot s$). The color scale of the trajectories denotes the magnitude of particle velocities. In all trials, the particle is always stably trapped to the same position. . .	75
4.3	Variable optical potential bottom locations for different rotation angles at the frequency of $0.5838(c/a)$. (a) Color representation of twelve optical potentials at rotational angles equally spaced from 0° to 330° , which indicates that particle with different rotational angles will be ultimately trapped to different locations. (b) Projection of optical force potential minima on xy-plane for twelve rotational angles. The arrows denotes the rotational angle increases clockwise. (c)–(d) projection of optical force potential minima on x- and y-planes, respectively.	77

- 4.4 Frequency-dependence of the conservative optical force field. (a) Perfect agreement of negative phase response calculated through finite-element method (earth yellow curves) and single-mode temporal coupled-mode theory (curved surface) in the frequency range of $(0.58c/a, 0.6c/a)$ and y-displacement range of $(0, 1.16a)$. The x-displacement is $0.4648a$, and the corresponding negative phase response at the frequency of $0.5838c/a$ is highlighted by the red curve. (b) The negative phase response as a function of particle position over the whole square metal-box resonator at the frequency of $0.5838c/a$. The red and blue lines indicate the vertical movements of particle moving along $x = 0.4648a$ and $x = 0.6285a$, and purple and green lines indicate the horizontal movements of particle along $y = 0.4648a$ and $y = 0.6558a$. (c) (d) Perfect agreement of optical forces calculated through RTOF (solid curves) and MST (dots) as the particle moves along the paths plotted in the same color indicated in (b). In RTOF calculation, the phase response in (b) is used to derive the phase gradient. 81
- 4.5 Discrete Helmholtz-Hodge decompositions (HHD) for single-port system and two-port system. (a) Reconstructed curl-free potential and divergence-free potential from HHD in single-port system. The rotational angle of L-shaped particle is 0o and the frequency is $0.5838c/a$. (b) reconstructed curl-free potential and divergence-free potential from HHD in two-port system. The two-port system is constructed by replacing the one-way single-mode waveguide by a regular two-way single-mode waveguide. To do the comparison with one-port system, the L-shaped particle has the same rotational angle and the system is operated at the same frequency as well. Compared with one-port case, the curl-free potential has worse confinement, and the divergence-free potential is obviously larger than that in one-port system. (c) Vorticity ratio calculated through normalized Frobenius norm after HHD for one-port system and two-port system. In one-port system, the vorticity ration decreases linearly with the increasing resolution in log-log scale until reaches the error limit (the error comes from the non-zero optical forces on L-shaped particle even when it touches the resonator walls). In two-port system, on the other hand, the vorticity ration hardly drops with increasing resolution. 84

5.1	Lossy topological photonic crystal (blue rods) with shells made of gain medium (orange shells). The lattice constant a is 0.04, the radii of lossy blue rods are $0.0978a$, and the thickness of the orange shells is $0.0196a$. The complex permittivity of the topological photonic crystal is set to be $14.63 - 0.5i$, and the complex permittivity of the active shells is $1 + \varepsilon''_{shell}$ where the suitable value of ε''_{shell} will be studied. The L-particle in the optical resonator is shown as well, which is kept identical to the that in Fig. 4.1.	88
5.2	Decay of the optical power along propagation direction when the magneto-optical photonic crystal is lossy. The structure is exactly the same as the structure in Fig. 4.1 except the permittivity now is $14.63 - 0.5i$. Since the resonant frequency of the square optical resonator depends on the location and orientation of the L-particle, the amount of optical power trapped by the optical resonator is varied by the L-particle. This will result in a fluctuation in the output power on the right and thus break the optical force conservativeness as the gradient of the output optical power is not zero, according to the conclusion of force conservativeness based on RTOF in Ch.3.	89
5.3	Correctness of weak-form simulation of lossy topological waveguide with active shell verified by COMSOL native eigensolver. (a) the z-component (out-of-plane component) of electric field, E_z , calculated by eigensolver at the floquet $k = 25rad/m$, and the eigenfrequency is calculated as $f = 4.5775 - 0.021662iGHz$. (b) E_z profile calculated from weak-form simulation for $f = 4.5775 - 0.021662iGHz$, and the result of floquet wave vector is $25rad/m$. The identical field profile also verifies the correctness of the weak-form simulation.	92

5.4	Dependence of the real part of complex wave vector k'_x and the imaginary part of complex wave vector k''_x on the permittivity of the active shell. The light grey bands are either bulk bands or left-propagating modes at the bottom of the structure calculated from the COMSOL eigensolver. The red dashed bands are the one-way waveguide modes calculated for the lossless topological photonic crystal waveguide. (a) complex wave vector computed by weak-form simulation within the frequency range of one-way waveguide mode when shell permittivity has no gain, i.e. $\epsilon_{shell} = 1$. k'_x is the real part of the wave vector shown in blue and k''_x is the imaginary part of the wave vector shown in green. (b) the complex wave vector computed from weak-form simulation for $\epsilon_{shell} = 1 + 2.2105i$. In this case, the imaginary part of k_x is reduced to zero for a wide range of frequency. (c) the complex wave vector computed from weak-form simulation for $\epsilon_{shell} = 1 + 3i$ at which the imaginary part of k_x becomes positive. The conservativeness of the optical force is broken as well in this case because the power gained at the output port also depends on the movement and orientation of L-particle in the optical resonator.	94
5.5	$freq - \epsilon''_{shell}$ relationship when $k''_x = 0$. (a) the curved surface is the dispersion relation of frequency with respect to the imaginary part of floquet wave vector k''_x within the range of ϵ''_{shell} from 0 to 3. The cutting plane at $k''_x = 0$ is shown in semi-transparent light gray. (b) the cross section between the plane and curved surface in (a), which is the $freq - \epsilon''_{shell}$ relationship we want to derive. At the frequency of $0.583(c/a)$ when the bottom of the optical potential in the square resonator is a tip rather than flat corresponds to the most proper imaginary part of shell permittivity equal to 2.25.	96
5.6	Norm of E-field along the waveguide. (a) the permittivity of the active shells is $1 + 1.2i$ and the operating frequency is $0.583(c/a)$. The optical power decays along the waveguide because of small imaginary part of the shell permittivity. (b) the permittivity of the active shells is $1 + 2.25i$ and the operating frequency is still $0.583(c/a)$. The optical power keeps constant along the optical waveguide.	97

5.7	<p>Irrotational potential and rotation potential derived by using Helmholtz-Hodge decomposition. (a) and (b) are irrotational potential Φ and rotational potential Ψ for the case when the active shell permittivity is $1+1.2i$ at the frequency of $0.583(c/a)$. (c) and (d) are irrotational potential Φ and rotational potential Ψ for the case when the active shell permittivity is $1 + 2.25i$ at the frequency of $0.583(c/a)$. The irrotational potential when $\epsilon''_{shell} = 2.25$ is one time deeper than that when $\epsilon''_{shell} = 1.2$ by comparing (c) with (a), while the rotational potential when $\epsilon''_{shell} = 2.25$ is a bit shallower than that when $\epsilon''_{shell} = 1.2$. Therefore, the vorticity ratio when $\epsilon''_{shell} = 2.25$ is expected to be about half of that when $\epsilon''_{shell} = 1.2$.</p>	99
5.8	<p>Vorticity ratio for different values of ϵ''_{shell}. When $\epsilon''_{shell} < 1.7$, most optical power is absorbed before reaching the square optical resonator and therefore the vorticity ratio changes slowly with ϵ''_{shell}. The vorticity ratio is minimized when ϵ''_{shell} is around 2.25, and then increases as the gained power at the output port breaks the force conservativeness again.</p>	100
6.1	<p>Categorization of ferrite rods in honeycomb lattice. The categorization is determined by the nearest row of rods to the further metal wall along +y-direction. (a) ferrite rods of group K (shown as white rods) are adjacent to the metal wall further along +y-direction; (b) ferrite rods of group K' (shown as gray rods) are adjacent to the metal wall further along +y-direction. The definition of lattice constant a is also labeled in the corresponding top-view illustrations in the bottom of corresponding devices.</p>	105
6.2	<p>Band diagram and mode profile of chiral edge state when K-group rods are the nearest to the top metal wall. Left: band diagram when the x-displacements of boundary rods and y-displacements of boundary rods are both 0. The normalized electric field intensity distribution corresponding to frequency of $0.2807(c/a)$ and floquet wave vector of $0.4774(2\pi/a)$ is plotted on the right half of the figure. The dispersion relation of one-way chiral edge mode depends on the displacements of the boundary rods.</p>	107

6.3	Band diagram and mode profile of chiral edge state when K'-group rods are the nearest to the top metal wall. Left: band diagram when the x-displacements of boundary rods and y-displacements of boundary rods are both 0. The normalized electric field intensity distribution corresponding to frequency of $0.2397(c/a)$ and floquet wave vector of $0.5226(2\pi/a)$ is plotted on the right half of the figure. The dispersion relation of one-way chiral edge mode also depends on the displacements of the boundary rods.	108
6.4	Band diagram and mode profile of "perfect" bulk mode. Left: band diagram when the x-displacements of boundary rods and y-displacements of boundary rods are both 0. The normalized electric field intensity distribution corresponding to frequency of $0.4084(c/a)$ and floquet wave vector of $1(2\pi/a)$ is plotted on the right half of the figure. The dispersion relation of this "perfect" bulk mode also depends on the displacements of the boundary rods.	109
6.5	Dependence of dispersion relation of chiral edge state when the boundary magneto-optical rods belonging to K-group. At the operating frequency of $0.27(c/a)$, the floquet wave vector corresponding to different displacements can be found from the intersections between the dispersion relation curves and the isofrequency line shown as green dashed line. The dispersion relation is more sensitive to y-displacement, which results in larger vertical optical force along y-axis according to RTOF.	112
6.6	Dependence of dispersion relation of chiral edge state when the boundary magneto-optical rods belonging to K'-group. At the operating frequency of $0.27(c/a)$, the floquet wave vector corresponding to different displacements can be found from the intersections between the dispersion relation curves and the isofrequency line shown as green dashed line. In this case, the dispersion relation is not quite sensitive to x-displacement, which results in horizontal optical force along x-axis very small . . .	113
6.7	Dependence of dispersion relation of "perfect" bulk mode when the boundary ferrite rods belong to K-group. The floquet wave vector corresponding to different combinations of (x,y)-displacements can be found from the intersections between the dispersion curves and the isofrequency line in green. Since the dispersion relations of displacements $(0.08a, 0.03a)$ and $(0, 0)$ do not have intersections with the dashed green line, the floquet wave vectors at this operating frequency are not available at this two displacements based on the existing simulation data.	115

- 6.8 Dependence of dispersion relation of “perfect” bulk mode when the boundary ferrite rods belong to K'-group. The floquet wave vector corresponding to different combinations of (x,y)-displacements can be found from the intersections between the dispersion relation curve and the green horizontal isofrequency line. In this case, since the dispersion relation weakly depends on y-displacement, the optical force long y-direction is expected to be much smaller than the optical force along x-direction. 116
- 6.9 Four examples of phase maps at one single operating frequency. (a) phase map at the frequency of $0.2532(c/a)$ when the chiral edge state is excited for the boundary magneto-optical rods of Group K. (b) phase map at the frequency of $0.2869(c/a)$ for the boundary magneto-optical rods of Group K' when the chiral edge state is excited. (c) phase map at the operating frequency of $0.408(c/a)$ for the boundary magneto-optical rods of Group K when the “perfect” bulk mode is excited. (d) phase map at the operating frequency of $0.408(c/a)$ for the boundary magneto-optical rods of Group K' when the “perfect” bulk mode is excited. 117
- 6.10 Agreement of the optical force calculation by using RTOF (curves) and Maxwell stress tensor integration (dots). (a) F_x on boundary magneto-optical rods of K-group at the frequency of $0.2632(c/a)$ for 3 y-displacements of $-0.05a$, $-0.01a$, and $0.02a$. (b) F_y on boundary magneto-optical rods of K-group at the operating frequency of $0.2632(c/a)$ for 3 x-displacements of 0, $0.04a$, and $0.08a$. (c) F_x on boundary magneto-optical rods of K'-group at the operating frequency of $0.2869(c/a)$ for 3 y-displacements of $-0.01a$, $0.01a$, and $0.03a$. (d) F_y on boundary magneto-optical rods of K'-group at the operating frequency of $0.2869(c/a)$ for 3 x-displacements of 0, $0.04a$, and $0.08a$ 120
- 6.11 Agreement between RTOF and Maxwell stress tensor integration on optical force generated by bulk modes for boundary magneto-optical rods of Group K and Group K'. (a) F_x on boundary magneto-optical rods of K-group at the frequency of $0.4088(c/a)$ for y-displacements of $-0.072a$, $0.039a$, and $0.043a$. (b) F_y on boundary magneto-optical rods of K-group at the frequency of $0.4084(c/a)$ for x-displacements of $0.072a$, $0.076a$, and $0.080a$. (c) F_x on boundary magneto-optical rods of K'-group at the frequency of $0.4082(c/a)$ for the y-displacements of $-0.06a$, $0.04a$, and $0.05a$. (d) F_y on boundary magneto-optical rods of K'-group at the frequency of $0.4080(c/a)$ for x-displacements of $0.06a$ and $-0.08a$ 121

- 6.12 Eigenfrequencies versus floquet wave vectors and displacements for boundary rods of Group K. (a). Eigenfrequencies versus $(k_x, xdisp)$ when y -displacement= $0.039a$, the isofrequency contours of $0.4086(c/a)$, $0.4088(c/a)$, and $0.4089(c/a)$ are highlighted as red curves which is proportional to the optical force potential. (b) Eigenfrequencies versus $(k_x, ydisp)$ when x -displacement= $-0.076a$, and the isofrequency contours of $0.4083(c/a)$, $0.4084(c/a)$, and $0.4085(c/a)$ are highlighted by yellow curves. (c) Eigenfrequency versus $(k_x, xdisp)$ when y -displacement= 0 , and the isofrequency contour of $0.4080(c/a)$ is highlighted by red curves. The top branch indicates optical potential with minimum which will trap the boundary rods to $xdisp = 0$, while the lower branch means optical force potential expels the boundary rods away from the origins when the light propagates to $-x$ -direction. (d) Eigenfrequency versus $(k_x, ydisp)$ when x -displacement= 0 , and the isofrequency= $0.4080(c/a)$ is highlighted by the yellow curves. Similarly, the top branch indicates stable equilibrium and the bottom branch means unstable equilibrium. 123
- 6.13 Eigenfrequencies versus floquet wave vectors and displacements for boundary rods of Group K'. (a). Eigenfrequencies versus $(k_x, xdisp)$ when y -displacement= $0.039a$, the isofrequency contours of $0.40825(c/a)$, $0.40832(c/a)$, and $0.40838(c/a)$ are highlighted as red curves which is proportional to the optical force potential. (b) Eigenfrequencies versus $(k_x, ydisp)$ when x -displacement= $-0.076a$, and the isofrequency contours of $0.40815(c/a)$, $0.40818(c/a)$, and $0.40821(c/a)$ are highlighted by yellow curves. (c) Eigenfrequency versus $(k_x, xdisp)$ when y -displacement= 0 , and the isofrequency contour of $0.4080(c/a)$ is highlighted by red curves. The top branch indicates optical potential with minimum which will trap the boundary rods to $xdisp = 0$, while the lower branch means optical force potential expels the boundary rods away from the origins when the light propagates to $-x$ -direction. (d) Eigenfrequency versus $(k_x, ydisp)$ when x -displacement= 0 , and the isofrequency= $0.4080(c/a)$ is highlighted by the yellow curves. Similarly, the top branch indicates stable equilibrium and the bottom branch means unstable equilibrium. 124

7.1	Agreement between the Reynold stress tensor and the response theory of acoustic force for 1D movement. The incident acoustic wave only consists of pressure wave and exerts on the bottom Nylon substrate, and therefore a single-port system is created. Because of the interference between the incident acoustic wave and the reflected acoustic wave, periodic acoustic intensity pattern is formed along the Nylon substrate and part of the acoustic power penetrates into the top movable Nylon slab. The top Nylon slab can freely slide on the oil membrane (assume no friction), and thus is trapped to highest acoustic intensity regions by acoustic gradient force.	131
7.2	Agreement between the Reynold stress tensor and the response theory of acoustic force for 2D movement. The incident pressure wave hits the wall of the cylindrical cup made of Nylon and the elastic energy is transferred to the water inside the cup and applies acoustic radiation pressure on the small Nylon particle in the water. The radius of the Nylon cup is $500nm$, the longer side of the elliptical particle is $30.9nm$, and the shorter side of the elliptical particle is $19.1nm$	132
7.3	Structure of single-port acoustic system in which conservative acoustic force exerting on the top phononic crystal can be created. The width and length of one unit cell is a and $1.6a$, respectively, to separate two resonances far away enough from each other to simplify the data processing steps. The thickness of both slabs is kept as $0.2a$, and the distance between two slabs is $0.26a$. The height and diameter of the pillars on both slabs are $0.2a$. The plane acoustic pressure wave is incident from the top and is then completely reflected from the bottom sound hard wall. The phase difference between the incident wave and the reflected wave Φ_r is measured for every displacement of the upper phononic crystal slab.	134
7.4	Acoustic force barrier formed along y-axis at the operating frequency of $0.1768(c/a)$. (a) the phase response as the upper phononic crystal is moving from $-0.5b$ to $0.5b$ along y-axis where $b = 1.6a$, as shown in the embedded illustration. This phase response is proportional to the actual acoustic force potential according to RTAF. (b) the acoustic force calculated using RTAF (curve) from the phase response has a perfect agreement with the first-principle calculation of the acoustic force using RST (dots). Note that the normalized acoustic force is on the scale of mN per Watt, which is much larger than the optical force, even though the stacked phononic crystal slabs at this operating frequency is not on resonance.	136

7.5	Fitting the temporal coupled mode theory (curves) to the first-principle FEM simulation (dots). The blue curve corresponds to displacements of $(0.5a, 0)$, the green curve corresponds to displacements of $(0.5a, 0.5b)$, and the orange curve corresponds to displacements of $(0, 0.5b)$. In all three cases, the phase response predicted by the temporal coupled mode theory have perfect agreement with those from FEM simulations. Different displacements of the upper phononic crystal slab will cause the resonant frequencies to change. Moreover, the dependence of the resonant frequency along y-direction is larger than that along x-direction.	138
7.6	Resonant frequency maps and decay rate maps with respect to the displacements of the upper phononic crystal slab in xy-plane. (a) resonant frequency map of the red resonance with respect to the displacements in xy-plane. (b) decay rate maps of the red resonance with respect to the displacements in xy-plane. (c) resonant frequency map of the blue resonance with respect to the displacements in xy-plane. (d) decay rate maps of the blue resonance with respect to the displacements in xy-plane. Both red resonant frequency and blue resonant frequency are not sensitive to x-displacement compared with their dependence on y-displacement. Similarly, decay rates are more dependent on y-displacement than x-displacement. Since the shape of acoustic force potential is determined by the resonant frequency map, it is much easier to create 1D acoustic barrier along y-direction without fine tuning of the operating frequency.	140
7.7	1D acoustic potential barrier as well as acoustic force calculated based on resonant frequency map and decay rate map derived from the temporal coupled mode theory. (a) intersection between the isofrequency plane of $0.1766(c/a)$ and the resonant frequency map of the blue resonance. The curves at the intersections determines the shape of acoustic force potential. (b) The phase response predicted by the temporal coupled mode theory at the operating frequency of $0.1766(c/a)$. The 2π phase transition happens at the displacements where the operating frequency plane intersects with the resonant frequency map. The intersection between the cut plane at $\Delta x = 0.5a$ and the phase response map is shown as the black curve. (c) the intersection between the cut plane at $\Delta x = 0.5a$ and the phase response map, i.e. the black curve in (b). (d) the acoustic force calculated based on the phase response in (c) using RTAF agrees with the acoustic force calculated using RST. Since the single-port CMT is used to do RTAF calculation, the acoustic force is conservative.	142

C.1 Linear dependence of truncation error on truncation period in log-log scale. (a) Conservative periodic vector field with both u_x and u_y are -1 in $[-1, 0]$ and 1 in $[0, 1]$; (b) $f(n)$ which is convolution between curl of Greens Function and the periodic vector field in the n^{th} period vanishes at infinity, and it blurs at large n due to limitation of precision of numeric data type of machine; (c) Truncation error E_T presents a linear dependence on truncation period N in log-log scale. 154

Chapter 1

Introduction

1.1 Background

Mechanically variable systems are ubiquitous in the real world including anything as big as ocean-going freighter or as small as atomic nucleus can be called mechanically variable system if only some components in it have some degree of freedom to move or rotate. Precisely and stably controlling the movement and orientation of these components ensure the normal operations of these multi-scale mechanically variable systems. Among all the controlling methods which have to apply certain form of force, optical force and acoustic force provide a non-touch manipulation of mechanically variable system ranging from nanometer scale to millimeter scale which are commons used in the applications such as atomic cooling [2, 13, 31], molecular and cell biology [85, 89], colloidal science [21, 41, 64, 71, 75], integrated photonics [35, 53, 55, 65], novel signal processing [14, 59, 82], and optical/atomic force imaging [37, 94].

The first part of completed projects have investigated the role of the optical forces, both in bulk and on discontinuous boundaries, in stimulated Brillouin scattering (SBS), and the sufficient conditions guaranteeing the conservativeness of the optical force, which can be applied in realizing slow

light, SBS-based signal processing, automatic optical alignment, and particle manipulation. To compensate the material loss which breaks the force conservativeness, a method of coating gain media surrounding the pillars of topological photonic crystal is demonstrated to recover the conservative optical force, which is significant in real-world application as material loss is inevitable in true experiments.

The achievement in the optical force research paves the road for the second half of my work on acoustic force. Acoustic force is generally several orders of magnitude larger than the optical force for a given amount of power and thus easier to be implemented in real experiments. The response theory of calculating acoustic force, which perfectly agrees with the conventional Reynold stress tensor method, is as well developed, based on which the system realizing auto-alignment of phononic crystal slab is constructed and capable of generating acoustic force on the order of N/W .

1.2 Motivation

1.2.1 Full vectorial calculation of the optical force

Although most nonlinear optical effects have been observed in nano-scale silicon photonic devices, the stimulated Brillouin scattering has entirely eluded observation in such devices over a decade. The stimulated Brillouin scattering gain coefficient in nano-scale silicon waveguide should be significant because of large refractive index contrast and small waveguide modal area. Despite of strong optical confinement in nano-scale silicon waveguide,

the elastic modes are not well confined in traditional silicon-on-insulator (SOI) waveguide in which the small mismatch of acoustic impedance between silicon and insulator substrate results in large acoustic mode leakage. Since the silicon-air boundary provides excellent acoustic mode confinement, the SBS effect is significantly enhanced in suspended silicon nano-scale waveguide. Unlike micro-scale photonic devices, the strong photon-boundary interaction in nano-scale waveguide has a significant impact on the photon-phonon coupling and the elastic wave displacements at the silicon-air boundaries also give rise to the non-linear polarization currents which contribute largely to the overall SBS gain coefficient.

1.2.2 Sufficient condition of conservative optical/acoustic force

Conservative optical force provides the possibility of realizing absolutely stable optical trapping which can be used for automatic self-alignment and stable particle orientation. Traditional optical trapping is restricted to particles with feature size much smaller than the wavelength so that dipole approximation can be assumed and the generally non-conservative scattering force is negligibly small. As the size of photonic devices increases to millimeter scale, the dipole approximation no longer holds and the significant scattering force will deteriorate the trapping performance. However, the optical self-alignment of photonic crystal slabs on millimeter scale enables the precise stacking fabrication of 3D photonic crystal devices providing complete photonic crystal bandgap and immune to unintended structural interruption,

which cannot be realized if the non-conservative component of optical force is not eliminated. To this end, the general condition warranting conservative optical force is explored and the non-conservative component of optical force is carefully eliminated in the proposed alignment system.

1.2.3 Response theory of acoustic force

Since the magnitude of radiation pressure is inversely proportional to the wave speed, the acoustic radiation pressure is expected to be several orders higher than its counterpart of optical radiation pressure. During the design and modeling of an acoustic system, the correct calculation of acoustic radiation pressure is of the most importance. Here I show the agreement between the force calculation via traditional Reynold stress tensor using first-principle computation in finite-element method and response theory of acoustic force (RTAF) using the phase response and displacement information of movable part. The significant improvement on the magnitude of acoustic radiation pressure over the optical radiation pressure is as well demonstrated in a complicated double-layer phononic crystal slab system, which indicates a promising way to realize the acoustic auto-alignment in the future.

1.3 Contributed work

1.3.1 Full vectorial calculation of SBS gain in nano-scale suspended silicon waveguide

We have developed a general framework to calculate the SBS gain coefficient in optical waveguide through the overlap integral between optical and

elastic eigen-modes. The optical forces originating from both radiation pressure and electrostrictive force are computed based on the full-vectorial electric field of optical eigenmodes, and each component of the displacement fields including P-wave (displacement is longitudinal to propagation direction) and S-wave (displacement is transverse to propagation direction) is evaluated in elastic eigen-mode. We show that both radiation pressure and electrostrictive force contribute significantly as the cross-section of the optical waveguide shrinks to sub-wavelength scale. Through the analysis of spatial distribution of each component of the optical forces, we show that the spatial symmetry of the optical forces dictates the selection rules of exciting well-coupled elastic modes. By applying this full-vectorial method to rectangular suspended waveguide, we demonstrate how the optical force field is coupled with each elastic mode for a range of scaling from $0.25\mu m$ to $25\mu m$ for forward SBS (FSBS) and backward SBS (BSBS) by locating and specifying the corresponding wave vector, \mathbf{k} . We further apply this method to investigate the intra- and inter- modal SBS processes, and reveal that the coupling between different optical modes is necessary to excite elastic modes with all possible symmetries. The part of work is reported in Chapter 2.

1.3.2 Conservative optical force in stacking photonic crystal slabs

We have deduced the sufficient condition for constructing conservative optical force field based on the response theory of optical force (RTOF) along with system response characterized by the temporal coupled-mode the-

ory (CMT). The conservativeness of the optical force which is calculated using RTOF can be predicted through the port number of the optical system regardless of the size of the device manipulated. Unlike optical force calculation using ray-optics approximation ($\lambda \ll a$) or dipole approximation ($\lambda \gg a$), we use the optical force formula developed in Chapter 2 using full vectorial electric field distribution from numerical simulation, which has perfect agreement with RTOF as well as Maxwell stress tensor formula. To illustrate the sufficient condition for conservative optical force, we construct a single-port system comprising of a photonic crystal slab with a perfect mirror at the bottom and a lossless polarizer on the top, in which conservative optical force field is established. We further corroborate the conservativeness of the constructed optical force field in single-port system via unique Helmholtz-Hodge decomposition. For photonic crystal slab system, we also reveal the fact that non-conservative component always co-exists with non-trivial optical force once the port number is larger than 1. This part of work is reported in Chapter 3.

1.3.3 Trapping and orientating nano-particles in one-way waveguide

The work aims at extending the application of conservative optical force to other single-port systems in which the nano-particles, bacteria or virus can be trapped and orientated for observation and selection. The single-port system can be established using lossless single-mode one-way waveguide, and the optical force magnitude can be enhanced by optical resonators adjacent to the one-way waveguide. The uniqueness of this trapping schemework is that

the conservative optical force realized by the unidirectional optical waveguide can control another degree of freedom, the rotation of the particle, in addition to translational motion. The part of work is reported in Chapter 4.

1.3.4 Self-aligned topological photonic crystal

In the last section, the topological photonic crystal is indispensable to realize one-way optical waveguide by which the manipulation of nano-particles can become true. However, the perfect arrangement of pillar array in topological photonic crystal is required to realize the above-mentioned goal, as the disorder of topological photonic crystal will introduce structural loss which is caused by the leakage of one-way waveguide mode into bulk of topological photonic crystal. Here I show by combining the optical forces generated from the waveguide mode and certain bulk mode, the topological photonic crystal can be self-aligned under the optical force, which is highly desired in the fabrication process of topological photonic crystals.

1.3.5 Compensating loss in one-way waveguide

To overcome the performance deterioration caused by loss in one-way waveguide in real experiment, the complex band structure of lossy one-way waveguide is studied using weak-form formula in finite-element method. By reducing the imaginary part of complex wave vector, the weak-form simulation can reduce the simulation time than by using the conventional frequency-domain simulation. We will propose easy-to-implement method to compensate

loss in one-way waveguide, and will investigate the effect of the gain medium on conservativeness of the optical force.

1.3.6 Auto-alignment of phononic crystal using acoustic force

The acoustic force is approximately 6 orders of magnitude larger than the optical force given the same amount of input power in the simplest scenario from momentum conservation, i.e. $\mathbf{F} = 2\mathbf{P}/\mathbf{v}$, and thus acoustical trapping attracts more attention because it is much easier to be implemented in the real experiments. The correct calculation of the acoustic force based on Reynold stress tensor acting on compressible particle of arbitrary shape is first introduced by Bruus in 2012. This result is further corroborated by the response theory of acoustic force similar to RTOF but providing more straightforward while deeper insight into characteristics of the acoustic force, which is of great significance in constructing purely conservative acoustic force field in acoustical alignment system.

1.4 Future work

1.4.1 Self-aligned topological photonic crystal with frequency modulation

When the topological photonic crystal is perfectly aligned, the bands of bulk modes are bi-directional with the wave vector along one direction traps the photonic crystal pillar while the wave vector along the opposite direction expels the photonic crystal pillar. To overcome the difficulty, frequency modulation may be required to suppress the bands corresponding to the un-

desirable wave vectors, and thus the self-aligned topological photonic crystal can be finally realized.

1.4.2 Two-dimensional acoustic trap

Unlike the electromagnetic waves, the resonance and decay rates of acoustic pressure wave is not sensitive to displacements of phononic crystal along the direction of shorter period, and therefore, two-dimensional acoustic trap is more difficult to construct compared with one-dimensional acoustic barrier. An additional layer of phononic crystal slab is possibly needed to create two-dimensional acoustic trap to align large-scale phononic crystal. Constructing a round acoustic trap to manipulate an elastic particle is easier than controlling a phononic crystal, in which an elastic substrate with acoustic resonator of snowflake shape is all one needs where the branches of the acoustic resonator help both incorporating more acoustic power and constructing the acoustic resonance.

Chapter 2

General framework of stimulated Brillouin scattering gain coefficient calculation in nano-scale systems

2.1 Stimulated Brillouin scattering in nano-scale systems

¹ Stimulated Brillouin Scattering (SBS) is a third-order nonlinear process in which two optical modes are coupled through an elastic mode[1, 7]. In a waveguide system, the time-varying optical force at the beating frequency of pump and Stokes wave is coupled with the elastic mode at the phase-matching wavevector and excites the modes of mechanical vibration (phonons) of the waveguide which in turn scatters the light between pump wave and Stokes wave. Since its discovery, SBS has been widely studied, yielding a wide variety of applications in efficient phonon generation [12, 15], optical frequency conversion[30, 32, 47], optical isolators[29, 50, 92], signal processing techniques[77, 95], slow light[44, 46, 48, 72, 73], and novel laser source[24, 28]. The versatility of stimulated Brillouin scattering applications stems from our

¹This work is partially based on “W. Qiu, P.T. Rakich, H. Shin, **H. Dong**, M. Soljačić, and Z. Wang, *Stimulated Brillouin scattering in nanoscale silicon step-index waveguides: a general framework of selection rules and calculating SBS gain*, Optics Express, 2013”. I contributed to optical force calculations in COMSOL and SBS gain calculation.

understanding and capability of manipulating this powerful form of photon-phonon coupling in a wide range of waveguide systems.

Conventional treatments of SBS, which have been proven remarkably accurate at microscales[1, 7], view Brillouin coupling as arising from the intrinsic material nonlinearities and do not count for radiation pressures and boundary-induced nonlinearities. However, these conventional treatments fail to predict SBS coupling within nano-scale silicon waveguides, as the radiation pressures arising from strong interaction of light with the boundaries of such waveguides are radically enhanced by nanoscale modal confinement and introduce radiation pressure mediated nonlinearity independent of the intrinsic material nonlinearity[51, 57, 58, 62, 69, 79]. Furthermore, boundary-induced nonlinearities induced by elastic wave displacements at discontinuous boundaries of silicon waveguides give rise to nonlinear polarization currents which significantly contribute to the overall SBS coupling[62].

In this chapter, a general framework of calculating SBS gain coefficient via the overlap integral of optical forces and elastic eigen-modes is presented, with emphasis on how to calculate radiation pressure on discontinuous boundaries of high-index contrast silicon waveguide and electrostrictive force both in bulk and on boundaries. This part of work has been reported in Ref.[56] as well as extended applications in slow light[83] and novel signal processing technologies[60].

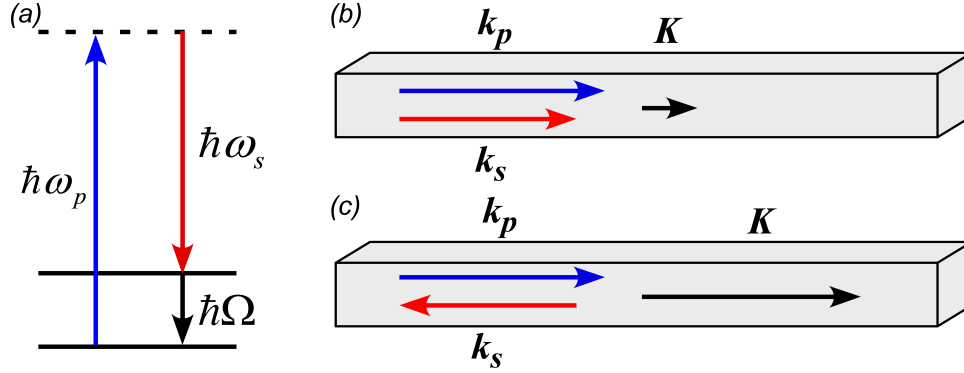


Figure 2.1: Typical SBS process in guided-wave system. (a) Energy level of the stimulated Brillouin scattering process, where ω_p , ω_s , and Ω are angular frequencies of pump photon, Stokes photon, and phonon. (b) Phase matching condition of forward SBS process, and (c) Phase matching condition of backward SBS process, where k_p , k_s , and K are wave number of pump wave, Stokes wave, and acoustic wave.

2.2 Calculating the SBS gain via overlap integral

2.2.1 General SBS gain induced by optical force

In a typical SBS process happening in a silicon waveguide along x-direction, the high-energy pump wave $\mathbf{E}_p e^{i(k_p x - \omega_p t)}$ interferes with the red-shifted Stokes wave $\mathbf{E}_s e^{i(k_s x - \omega_s t)}$ to generate an acoustic phonon at the beating frequency of Ω , and vice versa. This process is illustrated in Fig 2.1. The energy conservation and phase matching condition require that $\Omega = \omega_p - \omega_s$ (Fig 2.1a) and $\mathbf{K} = \mathbf{k}_p - \mathbf{k}_s$ (Fig 2.1b,c). Since the cross-section of this silicon strip waveguide is on nano-scale, the translational invariance limits the pump wave and Stokes wave on the single x-axis. Therefore, depending on the directions of launching waves, SBS can be categorized into forward SBS (Fig 2.1b) in which two codirectionally propagating light waves are coupled through

standing-wave phonons and backward SBS (Fig 2.1c) in which two counter-propagating light waves are coupled through traveling-wave phonons. The photon-phonon coupling is generally characterized by parametric conversion with the canonical relation[1, 7]

$$dP_s/dx = G_B \cdot P_p P_s - \alpha_s P_s \quad (2.1)$$

Here, P_p and P_s are the guided power of pump wave and Stokes wave, and G_B is the stimulated SBS modal gain coefficient. Note that the first term on RHS of Eq 2.1 is related to Stokes photon generation rate, which is equal to phonon generation rate, by a factor of $1/\hbar\omega_s$, the SBS gain can be calculated through particle flux conservation [62]

$$G_B = \frac{1}{2} \frac{\omega_s}{\Omega} \frac{1}{P_p P_s} \text{Re} \langle \mathbf{f}_\Omega, \frac{d\mathbf{u}}{dt} \rangle \quad (2.2)$$

where \mathbf{f}_Ω is a generally defined total optical force distribution at the beating frequency of Ω and \mathbf{u} is the total elastic deformation induced by \mathbf{f}_Ω . The bracket $\langle \mathbf{A}, \mathbf{B} \rangle$ denotes the time-averaged product of \mathbf{A} and \mathbf{B} (here only real part is reserved with coefficient of 1/2 introduced) which is subsequently integrated over the cross-section of the waveguide to give the total power generated by the optical forces.

2.2.2 SBS gain of each elastic eigen-mode

Unlike the frequency response method of calculating SBS gain presented in last section which can only give the total SBS gain via the aggregated optical force field and displacement field [62], the eigen-mode method is developed

in this section to investigate disparate contributions to SBS gain from each orthogonal elastic eigen-mode. Under the excitation of optical force \mathbf{f}_Ω , the total displacement response \mathbf{u} can be mathematically decomposed into a linear combination of elastic modes which coefficients can be derived from the orthogonality of these elastic modes. In the case of only two presenting optical fields, pump wave and Stokes wave, the optical force $\mathbf{f}_\Omega e^{-i\Omega t}$ drives the elastic deformation response $\mathbf{u} e^{-i\Omega t}$ oscillating at the same frequency which is governed by the equation of motion without elastic loss [66]

$$-\rho\Omega^2\mathbf{u}_i = \frac{\partial}{\partial x_j} c_{ijkl} \frac{\partial u_l}{\partial x_k} + \mathbf{f}_i \quad (2.3)$$

where ρ is the mass density and c_{ijkl} is the elastic tensor with important symmetric properties ($c_{ijkl} = c_{jikl}$, $c_{ijkl} = c_{ijlk}$, and $c_{ijkl} = c_{klij}$). With these symmetric properties of c_{ijkl} , the operator $\frac{\partial}{\partial x_j} c_{ijkl} \frac{\partial}{\partial x_k}$ on the RHS of Eq 2.3 is proven to be Hermitian [54] to guarantee the orthogonality the m^{th} order eigen-mode $\mathbf{u}_m e^{-i\Omega_m t}$ with respect to all other eigen-modes

$$\langle \mathbf{u}_m, \rho \mathbf{u}_n \rangle = \delta_{mn} \langle \mathbf{u}_m, \rho \mathbf{u}_m \rangle \quad (2.4)$$

Whenever an external force \mathbf{f}_i exists, a set of elastic eigen-modes are excited to give a linear combination of total displacement $\mathbf{u} = \sum_m b_m \mathbf{u}_m$, Eq 2.3 can be rewritten as

$$-\rho\Omega^2 \sum_m b_m \mathbf{u}_m = - \sum_m \rho\Omega_m^2 b_m \mathbf{u}_m + \mathbf{f}_i \quad (2.5)$$

Using the orthogonality in Eq 2.4, the coefficient b_m can be calculated as

$$b_m = \frac{\langle \mathbf{u}_m, \mathbf{f} \rangle}{\langle \mathbf{u}_m, \rho \mathbf{u}_m \rangle} \frac{1}{\Omega_m^2 - \Omega^2} \quad (2.6)$$

When elastic loss presents, the first-order effect of loss is considered and can be characterized by changing real-valued Ω_m to a complex value $\Omega_m - i\Gamma_m/2$. Assuming the quality factor $Q_m = \Omega_m/\Gamma_m$ is well above 1 (1000 is used in numerical simulations and experimental results show it can exceed 1000 [11, 22]) and $\Omega \approx \Omega_m$, the coefficient b_m is given by

$$b_m = \frac{\langle \mathbf{u}_m, \mathbf{f} \rangle}{\langle \mathbf{u}_m, \rho \mathbf{u}_m \rangle} \frac{1}{\Omega_m \Gamma_m} \frac{\Gamma_m/2}{\Omega_m - \Omega - i\Gamma_m/2} \quad (2.7)$$

Knowing the coefficient of each eigen-mode \mathbf{u}_m , the total SBS gain coefficient in Eq 2.2 can be calculated as the linear sum of all SBS gain of each order elastic mode. With the assumption of \mathbf{u} oscillating at frequency Ω , Eq 2.2 can be retrieved as

$$\begin{aligned} G_B &= \frac{1}{2} \frac{\omega_s}{P_p P_s} \text{Im} \langle \mathbf{f}_\Omega, \mathbf{u} \rangle \\ &= \frac{1}{2} \frac{\omega_s}{P_p P_s} \sum_m \text{Im}(b_m) \langle \mathbf{f}_\Omega, \mathbf{u}_m \rangle \\ &= \frac{1}{2} \frac{\omega_s}{P_p P_s} \sum_m \frac{\langle \mathbf{u}_m, \mathbf{f}_\Omega \rangle}{\langle \mathbf{u}_m, \rho \mathbf{u}_m \rangle \Omega_m \Gamma_m} \frac{(\Gamma_m/2)^2}{(\Omega_m - \Omega)^2 + (\Gamma_m/2)^2} \langle \mathbf{f}_\Omega, \mathbf{u}_m \rangle \\ &= \sum_m \frac{\omega_s Q_m |\langle \mathbf{f}_\Omega, \mathbf{u}_m \rangle|^2}{2 P_p P_s \Omega_m^2 \langle \mathbf{u}_m, \rho \mathbf{u}_m \rangle} \frac{(\Gamma_m/2)^2}{(\Omega_m - \Omega)^2 + (\Gamma_m/2)^2} \end{aligned} \quad (2.8)$$

It is obvious that each elastic mode has a SBS gain of Lorentzian shape with a peak value of $(\omega_s Q_m |\langle \mathbf{f}_\Omega, \mathbf{u}_m \rangle|^2) / (2 P_p P_s \Omega_m^2 \langle \mathbf{u}_m, \rho \mathbf{u}_m \rangle)$. Since the only assumption about the optical force \mathbf{f}_Ω is that it operates at the beating frequency Ω , this peak value is suitable for arbitrary shape of cross-section of a waveguide. In the numerical finite-element method for any geometry, one can calculate the mode profiles of pump wave and Stokes wave for a given

frequency $\omega_{p,s}$ ($\sim 1550nm$) as well as their wavevector $k_{p,s}$. The displacement distribution \mathbf{u}_m of each elastic eigen-mode at the phase matching condition $q = k_p - k_s$ (setup as Floquet periodic boundary condition) can be subsequently calculated. Moreover, Eq 2.8 indicates an easy way to separate effects coming from different optical force components, as the overlap integral $\langle \mathbf{f}_\Omega, \mathbf{u} \rangle$ is a linear sum of all optical forces. The only remaining problem is how to find the correct total optical force \mathbf{f}_Ω .

2.3 Radiation pressure on discontinuous boundaries

2.3.1 General MST in homogeneous material

The radiation pressure contribution to the total optical force \mathbf{f}_Ω can be directly derived from the well-known 3×3 Maxwell Stress Tensor (MST) \mathbb{T} , i.e. $\mathbf{f}_\Omega^{RP} = \nabla \cdot \mathbb{T}$ under steady state, where the MST is defined as

$$\mathbb{T} = \begin{bmatrix} T_{11}, T_{12}, T_{13} \\ T_{21}, T_{22}, T_{23} \\ T_{31}, T_{32}, T_{33} \end{bmatrix}.$$

Each entry of the electric and magnetic components of MST is given by [20]

$$\begin{cases} T_{ij}^E = E_i D_j - \frac{1}{2} \delta_{ij} \mathbf{E} \cdot \mathbf{D} \\ T_{ij}^M = B_i H_j - \frac{1}{2} \delta_{ij} \mathbf{B} \cdot \mathbf{H} \end{cases} \quad i, j = 1, 2, 3 \quad (2.9)$$

Here δ_{ij} is the Kronecker delta function. Eq 2.9 is quite general and suitable to find the radiation pressure at the interface of even anisotropic materials. Besides the default MST expressions in COMSOL, one can use the expressions in Appendix A to find the radiation pressure right on the interface of two distinct materials. In isotropic material, radiation pressure is proven to localize at

discontinuous interface of hybrid homogeneous material system where the gradient of relative permittivity ϵ_r is non-zero (the magnetic component of MST is zero for dielectric material, i.e. relative permeability $\mu_r = 1$ everywhere) [19, 27, 40]. The electric component of instantaneous MST is

$$T_{ij}^E(t) = \epsilon_o \epsilon_r [E_i(t)E_j(t) - \frac{1}{2}\delta_{ij}|\mathbf{E}(t)|^2] \quad i, j = 1, 2, 3 \quad (2.10)$$

where ϵ_r is a scalar rather than a 3×3 anisotropic matrix.

2.3.2 Decomposition of MST on discontinuous boundaries

However, MST fails to provide insight of how material discontinuity is responsible for generating radiation pressure by noting that \mathbf{E} is not continuous at the interface, and therefore the field is decomposed into tangential electric field \mathbf{E}_t and normal displacement field \mathbf{D}_n as they are continuous across the interface to reveal the effect of material discontinuity. The surface pressure \mathbf{F}^{RP} is related to force density distribution \mathbf{f}_Ω^{RP} using Gauss's theorem

$$\iiint_V (\nabla \cdot \mathbb{T}) dV = \oiint_s (\mathbb{T}\mathbf{n}) \cdot d\mathbf{s} = \oiint_s \mathbf{F}^{RP} \cdot d\mathbf{s} \quad (2.11)$$

where \mathbf{n} is the surface normal vector and $\mathbf{F}^{RP} \triangleq \mathbb{T}\mathbf{n}$. Knowing each entry in MST given by Eq 2.10, the surface pressure \mathbf{F}^{RP} can be calculated via matrix multiplication

$$\mathbf{F}^{RP} = \epsilon_o \epsilon_r [(\mathbf{E}(t) \cdot \mathbf{n})\mathbf{E}(t) - \frac{1}{2}|\mathbf{E}(t)|^2\mathbf{n}] \quad (2.12)$$

At the interface of two homogeneous materials, the electric field is decomposed into tangential electric component and normal electric component, i.e. $\mathbf{E}(t) =$

$E_n(t)\mathbf{n} + E_t(t)\mathbf{t}$. Insert this decomposed form of electric field into Eq 2.12 and get

$$\begin{aligned}\mathbf{F}^{RP} &= \epsilon_o\epsilon_r [E_n(t)[E_n(t)\mathbf{n} + E_t(t)\mathbf{t}] - \frac{1}{2}|E_n(t)\mathbf{n} + E_t(t)\mathbf{t}|^2\mathbf{n}] \\ &= D_n(t)E_t(t)\mathbf{t} + \frac{1}{2}[(\epsilon_o\epsilon_r)^{-1}D_n(t)^2 - \epsilon_o\epsilon_r E_t(t)^2]\mathbf{n}\end{aligned}\quad (2.13)$$

The radiation pressure turns out to be the difference of the surface pressure on two sides of the interface, and combining the boundary conditions ($\epsilon_o\epsilon_{r1}E_{1n} = \epsilon_o\epsilon_{r2}E_{2n} = D_n$ and $E_{1t} = E_{2t} = E_t$) we can find the total surface pressure is

$$\mathbf{F}_t^{RP} = \frac{1}{2}[\epsilon_o^{-1}D_n(t)^2(\epsilon_{r2}^{-1} - \epsilon_{r1}^{-1}) - \epsilon_o E_t(t)^2(\epsilon_{r2} - \epsilon_{r1})]\mathbf{n}\quad (2.14)$$

Note that the tangential component of surface pressure cancels out across the interface, and thus the total radiation pressure is purely perpendicular to the interface. In the studied FSBS process, the total electric field $[\mathbf{E}_p e^{i(k_px - \omega_pt)} + \mathbf{E}_s e^{i(k_sx - \omega_st)}] + c.c.$ is inserted into Eq 2.14 and only terms of frequency Ω are reserved to derive the amplitude of time-harmonic radiation pressure of the form $\mathbf{F}_t^{RP} e^{i(qx - \Omega t)}$ as

$$\mathbf{F}_t^{RP} = \frac{1}{2}[\epsilon_o^{-1}D_{pn}D_{sn}^*(\epsilon_{r2}^{-1} - \epsilon_{r1}^{-1}) - \epsilon_o E_{pt}E_{st}^*(\epsilon_{r2} - \epsilon_{r1})]\mathbf{n}\quad (2.15)$$

The radiation pressure is obviously normal to the interface, pointing from high-index region to low-index region. In axially translationally invariant waveguide, the radiation pressure is always real and transverse.

In BSBS, the total electric field of counter-propagating waves becomes $[\mathbf{E}_p e^{i(k_px - \omega_pt)} + \mathbf{E}_s e^{i(k_s(-x) - \omega_st)}] + c.c.$, and therefore the radiation pressure

changes accordingly as

$$\mathbf{F}_t^{RP} = \frac{1}{2} [\epsilon_o^{-1} D_{pn} D_{sn} (\epsilon_{r2}^{-1} - \epsilon_{r1}^{-1}) - \epsilon_o E_{pt} E_{st} (\epsilon_{r2} - \epsilon_{r1})] \mathbf{n} \quad (2.16)$$

It is worthy to mention that in a homogeneous material the divergence of MST generates zero body force as we can see from Eq 2.15 and Eq 2.16 which are related to body force through Gauss's theorem. Therefore, the radiation pressure only exists and is normal to the interface of two homogeneous materials, pointing from high-index medium to low-index medium.

2.4 Electrostrictive force in bulk and on boundaries

Electrostrictive forces are calculated from the electrostriction tensor \mathbb{S} , which is similar to MST, a 3×3 matrix with each entry given by

$$\sigma_{ij} = -\frac{1}{2} \epsilon_o n^4 p_{ijkl} E_k(t) E_l(t) \quad i, j, k, l = 1, 2, 3 \quad (2.17)$$

where n is the refractive index of the homogeneous materials, and p_{ijkl} is the photoelastic tensor [67]. In a FSBS process happening in a guided-wave system, the electric field components $E_{k,l}$ in Eq 2.17 is replaced by the total codirectionally propagating waves $(\mathbf{E}_p e^{i(k_p x - \omega_p t)} + \mathbf{E}_s e^{i(k_s x - \omega_s t)})/2 + c.c.$, and only the components with the frequency of Ω are reserved

$$\sigma_{ij} = -\frac{1}{4} \epsilon_o n^4 p_{ijkl} (E_{pk} E_{sl}^* + E_{pl} E_{sk}^*) \quad i, j, k, l = 1, 2, 3 \quad (2.18)$$

As the most commonly used material in integrated optics either have cubic crystalline lattice (silicon) or are isotropic (silica glass) and commercial waveguide systems are fabricated to be aligned with the principle axis of the medium,

we assume the crystal structure of the material is symmetric with respect to plane of $x = 0$, $y = 0$, and $z = 0$. Therefore, if p_{ijkl} has odd number of certain component, it is zero. In Voigt notation, Eq 2.18 can be explicitly written as

$$\begin{bmatrix} \sigma_{11} \\ \sigma_{22} \\ \sigma_{33} \\ \sigma_{23} \\ \sigma_{13} \\ \sigma_{12} \end{bmatrix} = -\frac{1}{2}\epsilon_o n^4 \begin{bmatrix} p_{11} & p_{12} & p_{13} & & & \\ p_{12} & p_{22} & p_{23} & & & \\ p_{13} & p_{23} & p_{33} & & & \\ & & & p_{44} & & \\ & & & & p_{55} & \\ & & & & & p_{66} \end{bmatrix} \begin{bmatrix} E_{p1}E_{s1}^* \\ E_{p2}E_{s2}^* \\ E_{p3}E_{s3}^* \\ E_{p2}E_{s3}^* + E_{p3}E_{s2}^* \\ E_{p1}E_{s3}^* + E_{p3}E_{s1}^* \\ E_{p1}E_{s2}^* + E_{p2}E_{s1}^* \end{bmatrix} \quad (2.19)$$

For BSBS in which one wave is launched from the opposite direction, the counter-propagating waves generate electrostrictive tensor as

$$\begin{bmatrix} \sigma_{11} \\ \sigma_{22} \\ \sigma_{33} \\ \sigma_{23} \\ \sigma_{13} \\ \sigma_{12} \end{bmatrix} = -\frac{1}{2}\epsilon_o n^4 \begin{bmatrix} p_{11} & p_{12} & p_{13} & & & \\ p_{12} & p_{22} & p_{23} & & & \\ p_{13} & p_{23} & p_{33} & & & \\ & & & p_{44} & & \\ & & & & p_{55} & \\ & & & & & p_{66} \end{bmatrix} \begin{bmatrix} E_{p1}E_{s1} \\ E_{p2}E_{s2} \\ E_{p3}E_{s3} \\ E_{p2}E_{s3} + E_{p3}E_{s2} \\ E_{p1}E_{s3} + E_{p3}E_{s1} \\ E_{p1}E_{s2} + E_{p2}E_{s1} \end{bmatrix} \quad (2.20)$$

In a hybrid system consisting of various homogeneous materials, electrostrictive force can exist inside each medium, giving rise to body force, and at the interface, generating electrostrictive pressure. The electrostrictive body force is given by the negative divergence of the electrostrictive tensor, i.e. $\mathbf{f}_\Omega^{ES} = -\nabla \cdot \mathbb{S}$. Similar to MST, the electrostrictive pressure on the interface of material 1 and material 2 is given by $\mathbf{F}^{ES} = (\mathbb{S}_1 - \mathbb{S}_2)\mathbf{n}$, with each component given by $F_i^{ES} = (\sigma_{1ij} - \sigma_{2ij})n_j$ (Einstein notation with respect to j is used here).

2.5 SBS gain coefficient in suspended silicon waveguide system

In this section, we apply the general framework to study the intra-modal and inter-modal SBS process of a silicon waveguide suspended in air (Fig. 2.2b insert). Intra-modal process is concerned with the configuration where the pump and the Stokes waves are launched into the same spatial optical mode of the waveguide, and both FSBS and BSBS are investigated. Inter-modal process includes the pump and the Stokes wave with distinct spatial optical mode of the waveguide, which essentially doubles the degree of freedom of tailoring optical force distribution. And silicon waveguides are of particular interest, because it can be fabricated on standard SOI platforms. In addition, a suspended silicon waveguide provides tight optical confinement through its large refractive index and nearly perfect elastic confinement through a dramatic impedance mismatch with air. Moreover, since radiation pressure is proportional to the difference of dielectric constants across waveguide boundaries and electrostriction force is quadratic over refractive index, both kinds of optical forces are significantly enhanced in high index contrast structures such as silicon waveguides. Here, we consider a silicon waveguide with a rectangular cross-section of a by $0.9a$ to distinguish two orthogonal optical modes. For silicon, we use refractive index $n = 3.5$, Young's modulus $E = 170 \times 10^9$ Pa, Poisson's ratio $\nu = 0.28$, and density $\rho = 2329\text{kg/m}^2$. In addition, we assume that the $[100]$, $[010]$, and $[001]$ symmetry direction of this crystalline silicon coincide with the x , y , and z axis respectively. Under this orientation, the photo-elastic

tensor p_{ijkl} in the contracted notation is $[p_{11}, p_{12}, p_{44}] = [-0.09, 0.017, -0.051]$ [25]. The structure has two symmetry planes $y = 0$ and $z = 0$. Both optical modes and elastic modes are either symmetric or anti-symmetric with respect to these planes.

2.5.1 Optical and elastic eigen-modes in suspended rectangular silicon waveguide

The advantage of eigen-mode method to calculate SBS gain is that we can separate the contributions from different optical and elastic eigenmodes and intuitively predict the SBS gain via spatial symmetry of optical force field and displacement distribution of each eigenmode. We characterize two fundamental orthogonal optical modes as E_{y11} and E_{z11} where E_{y11} mode has even E_y component and odd E_z component with respect to $y = 0$ and $z = 0$ planes and E_{z11} has the orthogonal polarization. Their dispersion relations are plotted in Fig. 2.2(a) in blue and red, respectively. Throughout the numerical experiment, we assume pump wavelength at $1.55\mu m$ and the unit of angular frequency is normalized by length scale a . Since $\Omega/\omega \approx V_L/c \approx 10^{-4}$, pump wave and Stokes wave approximately correspond to the same spatial optical mode, and thus we use E_{y11} mode as electric field spatial distribution for both waves. Therefore, induced optical force in intra-modal coupling is always symmetry with respect to $y = 0$ and $z = 0$ plane, and thus only elastic eigenmodes with the same symmetry will gain maximum power from optical mode and be excited. The elastic eigen-modes are computed in eigensolver as well, and shown in Fig. 2.2(b) where blue dash curves are calculated by forcing

$u_y = u_z = 0$ and red dash curves are derived by prescribing $u_x = 0$. The P-wave is defined as only having deformation along longitudinal axis (x-axis) and S-wave is defined as having deformation along transverse axis (y- and z-axis). When acoustic wave vector $q = 0$, either P-modes or S-modes can be excited, whereas at nonzero q hybridized acoustic modes denoted by E with displacements along all directions can be excited.

2.5.2 Intra-modal coupling versus Inter-modal coupling

In this section, the numerical experiment results of calculating SBS gain for intra-modal photon-phonon coupling (including FSBS and BSBS) and inter-modal coupling (only FSBS) are presented.

Due to zero longitudinal optical force in FSBS, only S-like elastic modes can be excited in this scenario. We choose $a = 315nm$ which presents the largest SBS gain within the range of a from $250nm$ to $2.5\mu m$, and the angular frequency of $0.203(2\pi a/c)$ which fits $1550nm$ wavelength. From Fig. 2.3, both electrostriction force and radiation pressure are even with respect to y-axis and z-axis, and has no longitudinal component because $dq/dx = iq = 0$. Knowing that either P-wave or S-wave can be excited at $q = 0$, the longitudinal P-wave won't be excited, leaving non-zero SBS gain for E2, E3, and E5 modes. Fig. 2.3(c) indicates that after $a = 315nm$, the radiation pressure induced SBS gain drops several orders (4-6) of magnitudes more quickly than electrostriction induced SBS gain, which agrees with conventional SBS theory that only electrostriction force plays significant role in micro-scale devices.

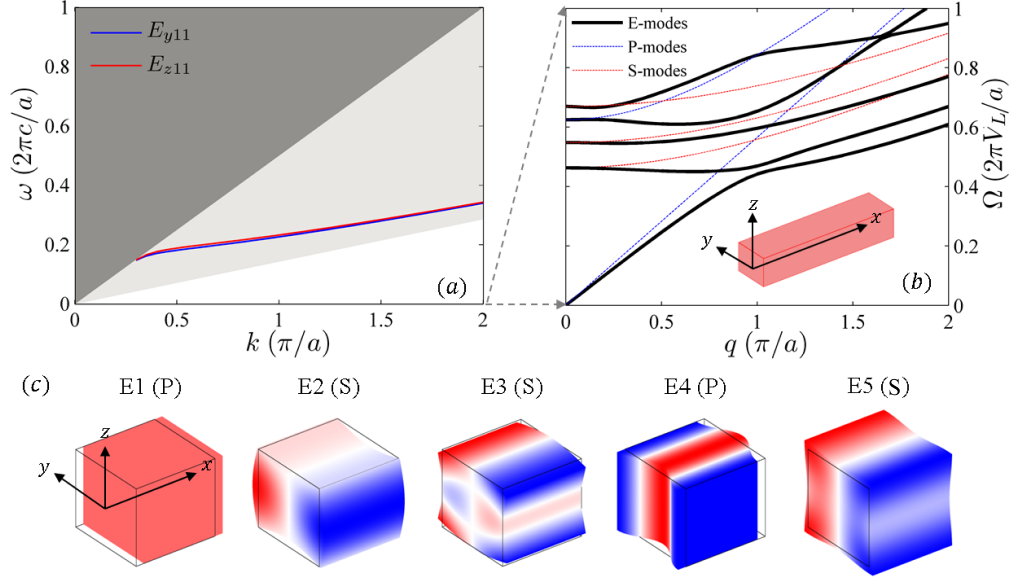


Figure 2.2: The guided optical and elastic modes of a silicon rectangular waveguide. Optical frequency is in unit of $2\pi c/a$, while elastic frequency is in unit of $2\pi V_L/a$. $V_L = \sqrt{E/\rho} = 8.54 \times 10^3 \text{m/s}$ is the velocity of longitudinal elastic waves in bulk silicon. (a) Dispersion relation of optical modes E_{y11} and E_{z11} . (b) Dispersion relation of elastic modes which have even symmetry with respect to both $y = 0$ and $z = 0$ planes. E-modes (black lines) are the eigen-modes of the actual silicon waveguide, with silicon-air interfaces treated as free boundaries. For comparison, the dispersion relations of purely longitudinal modes (designated as P-modes, blue curves) and purely transverse modes (designated as P-modes, red curves) are included. They are constrained respectively with x-only displacement, and y-z-only movements. At $q = 0$, E-modes manifest as either P-modes or S-modes. (c) The displacement profiles of mode E1 through E5 at $q = 0$, with the peak deformation shown. The color represents y-displacement (u_y) for S-like E modes and x-displacement (u_x) for P-like E modes. Blue, white, and red correspond to negative, zero, and positive values respectively. Mode E1 experience a DC longitudinal offset at $\Omega = 0$.

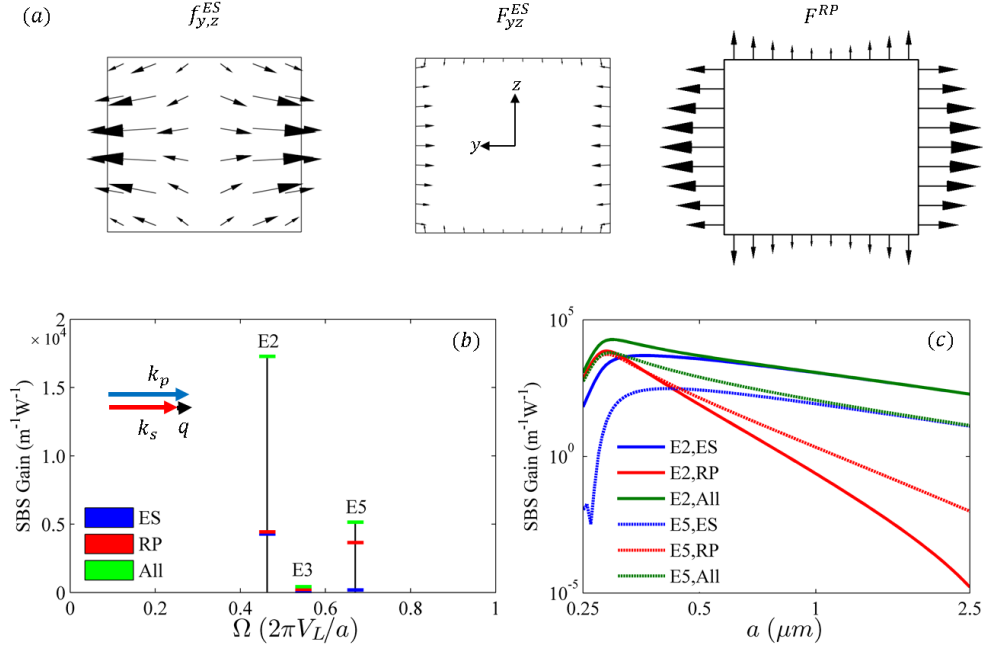


Figure 2.3: Optical force distributions and the resultant gain coefficients of the Forward SBS. In panels (a) and (b), the width of the waveguide is $a = 315\text{nm}$, and the incident optical waves have $\omega = 0.203(2\pi c/a)$, and $k = 0.75(\pi/a)$. The elastic waves are generated at $q = 0$. (a) The force distribution of electrostriction body force density, electrostriction surface pressure, and radiation pressure respectively. All three types of optical forces are transverse. (b) Calculated FSBS gains of the elastic modes, assuming mechanical $Q = 1000$. Blue, red, and green bars represent FSBS gains under three conditions: electrostriction-only, radiation-pressure-only, and the combined effects. Only the S-like E modes have non-zero gains. (c) The scaling relation of FSBS gains as the device dimension a is varied from $0.25\mu\text{m}$ to $2.5\mu\text{m}$. Solid and dotted curves correspond to the gain coefficients for mode E2 and E5 respectively.

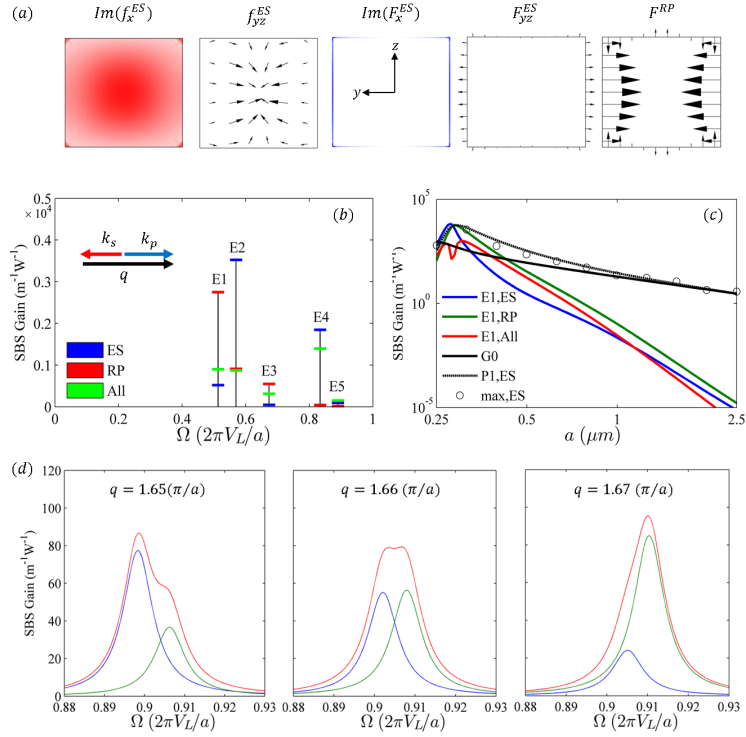


Figure 2.4: Optical force distributions and the resultant gain coefficients of the Backward SBS. In panels (a) and (b), the width of the waveguide is $a = 315\text{nm}$, and the incident optical waves have $\omega = 0.203(2\pi c/a)$, and $k = 0.75(\pi/a)$. The elastic waves are generated at $q = 1.5(\pi/a)$. (a) The force distribution of electrostriction body force density, electrostriction surface pressure, and radiation pressure respectively. Electrostriction have both longitudinal and transverse components. Radiation pressure are purely transverse. (b) Calculated BSBS gains of the elastic modes, assuming mechanical $Q = 1000$. Blue, red, and green bars represent FSBS gains under three conditions: electrostriction-only, radiation-pressure-only, and the combined effects.(c) The scaling relation of BSBS gains related to mode E1 as a is varied from $0.25\mu\text{m}$ to $2.5\mu\text{m}$. Gain coefficients predicted by conventional fiber BSBS theory are shown as the solid black curve. The dotted black curve represents the electrostriction-only BSBS gain of mode P1. Black circles represent the largest electrostriction-only BSBS gain coefficient among all E-modes for a given a . (d) BSBS spectra near the anti-crossing between mode E4 and E5 around $q = 1.66(\pi/a)$. The mechanical quality factor Q is assumed to be 100. The red lines represent the total BSBS gain. The blue and green lines represent contributions from mode E4 and E5.

Unlike FSBS, the acoustic wave vector in BSBS is not zero, which results in non-zero longitudinal component in electrostriction force, which will excite P-wave elastic eigenmodes as well. In Fig. 2.4, panels (a) and (b) both remain $a = 315nm$ and $\omega = 0.203(2\pi c/a)$. The only difference from FSBS is that elastic modes are calculated at $q = 2k$. The longitudinal elastic modes E1 and E4 are both excited. As a increases its size, the initially excited fundamental P1 mode will intersect with other hybridized elastic mode as indicated from the elastic mode band diagram. The hybridized mode which happens to have similar shape with P1 mode would gain power from fundamental P1 mode and then be excited. The maximum SBS gain among all E-modes for each a are plotted as circles in Fig. 2.4(c). Fig. 2.4 (d) presents the effect of intersection of different hybridized mode (E4 and E5) in band diagram. As the acoustic wave vector q is shifted across the intersection point, the portion of excited E4 mode and E5 mode depends on the tiny tuning of acoustic wave vector, and thus gives different overall SBS gain contributed from electrostriction.

Since both electrostriction force and radiation pressure in FSBS and BSBS are even with respect to y -axis and z -axis due to similar overlap pump and Stokes electric fields, the possible way to excite elastic modes with all possible symmetries is to use inter-mode SBS coupling. We choose two optical modes with wave vector $k = 0.750(\pi/a)$ and $k = 0.665(\pi/a)$ which presents orthogonal field polarization, and as a result uneven force distribution is generated as shown in Fig. 2.5 (a). In this case, the first and second hybridized elastic modes at $q = 0.085(\pi/a)$ with rotational and breathing motion respec-

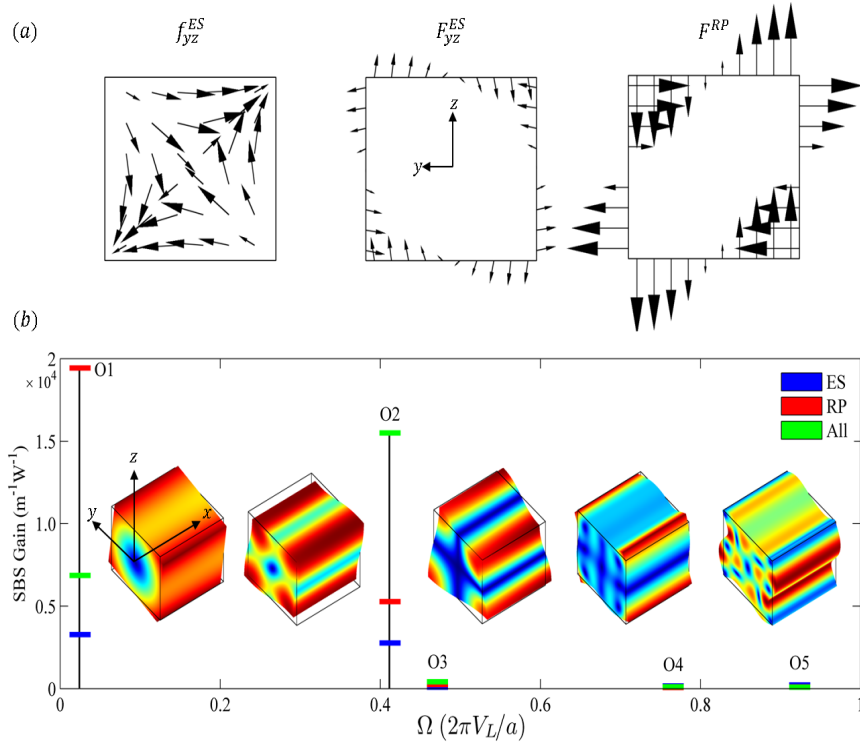


Figure 2.5: Optical force distributions, relevant elastic modes, and the resultant gain coefficients of inter-modal FSBS between E_{y11} (pump) and E_{z11} (Stokes). The width of the waveguide is set to be $a = 315\text{nm}$. The incident optical waves have $\omega = 0.203(2\pi c/a)$, with the pump-wave propagation constant at $k_p = 0.750(\pi/a)$, and the Stokes-wave propagation constant at $k_s = 0.665(\pi/a)$. The elastic waves are generated at $q = 0.085(\pi/a)$. (a) The force distribution of electrostriction body force density, electrostriction surface pressure, and radiation pressure respectively. The longitudinal forces (not shown here) are negligible, in comparison to the transverse forces. All optical forces are anti-symmetric with respect to plane $y = 0$ and plane $z = 0$, exciting elastic modes with the matching symmetry (designated as O-modes). (b) Calculated inter-modal SBS gains, assuming mechanical $Q = 1000$. The insets illustrate the displacement profiles of mode O1 through O5 at $q = 0.085(\pi/a)$, at peak deformation. "Jet" colormap is used to show the amplitude of *total* displacement. Blue and red correspond to zero and maximum respectively.

tively have good shape matching of optical force field, and therefore are hugely enhanced, compared with SBS gain derived in Fig. 2.4.

2.6 Concluding remarks

In this chapter, the optical forces in the bulk and on the boundaries are investigated and comprehensively give the SBS gain in nano-scale system. Unlike traditional treatment of this second-order nonlinearity in micro-scale system, the radiation pressure on the boundaries is taken into account, predicting a huge enhancement of SBS gain in nano-scale system. In the next chapter, it will be shown that radiation pressure also plays a significant role of manipulating objects ranging from nano-scale to even millimeter scale, which is promising in applications ranging from atom cooling, particle trapping, to automatic alignment in stacking fabrication.

Chapter 3

Self-alignment of millimeter-scale photonic crystal slabs with sub-nanometer resolution

3.1 Automatic self-alignment technologies using optical forces

¹ In this chapter, another branch of application of radiation force is investigated to find the general condition to construct an optical force field to align millimeter-scale photonic crystal (PC) slabs with sub-nanometer resolution. A purely conservative optical force field constructed from guided resonances confined within PC slabs is an indispensable prerequisite for stable alignment. Using the response theory of optical force (RTOF) and temporal coupled-mode theory (CMT), we show that a single-port system warrants establishing optical force potential well and furthermore significantly enhances the force strength at the potential edges. The conclusions provide much more straightforward insights into non-conservative nature of optical force and simple methods to adjust trapping position and resolution.

¹This work is partially based on “**H. Dong** and Z. Wang, *All-optical near-field self-alignment in sub-nanoscale induced by Fano-resonance*, APS March Meeting 2015, San Antonio, TX”.

3.1.1 Brief overview of optical manipulation techniques

Optical forces have been widely used for non-touch manipulation of atoms and nano-structures in fields ranging from atomic physics [2, 31], molecular and cell biology [85, 89], colloidal science [21, 41, 64, 71, 75] to integrated photonics [35, 53, 65]. However, these optical trapping technologies are limited to manipulating single or multiple particles on the top surface of optical cavities or waveguides, and also vulnerable to vibration and rotation induced by natural non-conservative component of optical forces, which are simply neglected as either it is relatively small compared with conservative component or it does not play a significant role in the applications. Here we present an ideal self-alignment system combining sub-nanometer resolution, millimeter-scale working range, and stability together, which is of particular useful during 3D assembly of PC slabs with artificial patterns on them. Such precise millimeter-scale 3D alignment enables strong and nearly-ideal spatial confinement of light due to existing photonic bandgaps of PC slabs, as well as reduces scattering loss induced by unintended disorders like structural misalignment. The stability of this 3D alignment requires a tunable potential well generated by a variable conservative optical force field depending on frequency, which will be revealed later.

3.1.2 The advantage of conservative optical force

The foremost advantage of optical forces is the sub-nanometer resolution of alignment in certain nanostructures with ultra-high Q-factor [10, 76, 90].

With the aid of ultra-high Q-factor, the optical force field can be rapidly and sensitively reconfigured by tuning the frequency of the incident illumination field. However, to realize sub-nanometer resolution using optical forces, one must be careful to eliminate any tiny vibration or rotation induced by the non-conservative component of the optical force field. These non-conservative components can be scattering forces widely seen in optical tweezers [63, 64, 88], and guided wave systems [52], which tend to increase the kinetic energy of the trapping object and subsequently drive them out of the potential well. This is particularly evident in the cases of anchoring particles where one must limit the particle size and its index contrast to obtain a nearly conservative optical force field (also known as gradient force [4]), and cooling atoms where standing-wave optical field is used to generate conservative force under dipole approximation [13]. Thanks to their small sizes, in both scenarios, one can apply dipole approximation and further assume the perturbation to the optical fields induced by the trapping target is negligible. Consequently, the 3D optical potential constructed in both cases is proportional to the field intensity distribution. However, the non-conservative component of the optical forces will become more significant as the structure size increases and index contrast gets higher, because the dipole approximation no longer holds as the optical field distribution is greatly disturbed by the moving object, and thereby introducing more non-conservative forces [61, 84].

With the help of optical alignment with absolute stability, scaling up the size of the trapping target beyond the tightly focused Gaussian beams

which are limited by a usable volume of λ^3 , as well as maintaining the sub-nanometer resolution, has significant technological applications. For instance, optically aligning a membrane with periodic sub-wavelength patterns (photonic crystal slab or meta-surfaces) on top of a periodic substrate enables layer-by-layer stacking fabrication of large-scale 3D photonic crystals [43, 70] and metamaterials with nanometer precision. Compared with the existing interference lithography [38] and self-assembly techniques [26], such layer-by-layer optical self-alignment is much more flexible as it allows assembly of disparate layers, provided that the in-plane periodicity (periodic pattern in the layer) is preserved. As a contrast, traditional self-alignment techniques require that the target structure to be periodic out of plane as well. This flexibility is crucial for future applications in silicon interconnects and flexible photonics.

3.1.3 Organization of this chapter

In this chapter, I present how a purely conservative optical force potential can be established even if incident plane wave has no intensity gradient along either axial (out-of-plane) or transversal (in-plane) directions. Unlike previous work where the conservativeness of near-field radiation pressure has been rarely explored, we reveal the underlying physics beneath the general non-conservative nature of radiation pressure, which helps to identify a universal criteria of constructing a conservative force field and self-aligning system. Within such system, the optical force is not merely the gradient of the intensity of near-field distribution, but also absolutely conservative.

We start with showing that the optical force in a lossless one-port system is guaranteed to be conservative, from a comprehensive analysis based on the response theory of optical force and the temporal coupled-mode theory (CMT). A real example of constructing such a system is given in Sec.3.2.1. The theoretical analysis is then further corroborated with finite-element numerical modeling using the Maxwell stress tensor (see appendix A) and radiation pressure on boundaries (see Chapter 2). Especially, the precise CMT capturing all the features of stacking PC slabs scheme is given in Sec.3.2.2, providing complete insight of indispensability of each component in the constructed system. Simply extending this analysis to two-port system, we illustrate the necessity of restricting the system output to a single port in order to construct conservative force field (Sec. 3.2.3). The spatial resolution of the conservative optical force field can be refined to sub-nanometer scale by choosing ultra high-Q resonance under the guidance of coupled-mode theory, and the position of optical force well bottom can be as well determined based on the spatial dependence of resonant frequency and decay rates (Sec.3.2.4). Finally, the conservativeness of the optical force field is verified with numerical Helmholtz-Hodge decomposition, which is done on TACC supercomputer (<https://www.tacc.utexas.edu/>) (Sec.3.3).

3.2 Conservative optical force established in stacked photonic crystal slabs system

A conservative force field \mathbf{F} , by definition, is irrotational or curl-free, i.e. $\nabla \times \mathbf{F} = 0$, in contrast to a non-conservative force which has a non-zero curl component. By translating this general mathematical conservation condition to an alternative expression of conservative optical force in terms of physical properties of the incident optical field, it becomes more enlightening for us to design a desired optical alignment system. A good example is that under the paraxial limit for a particle small enough for dipole approximation, the curl of the optical force is proportional to the cross product between the intensity gradient and the phase gradient of the incident optical beam, i.e. $\nabla I \times \nabla \phi$ [42]. A straightforward conservative condition can be derived right away as these two gradients must be parallel to each other. Unfortunately, the paraxial approximation in integrated photonic system is generally broken, especially for guided modes in a waveguide with high index contrast. Optical resonances also significantly alter the near field from that of illumination field, even in a very simple structure [84], which requires us to examine integrated photonic systems closely and understand the unique physical constraints from curl-free conditions for conservative optical force.

3.2.1 One-port system guaranteeing conservative optical forces

In this section, we rely on the response theory of optical force (RTOF) [61] to deduce the general conservative condition of optical force field, taking

the advantage of the fact that many integrated photonic system can be described as n-port framework with well-defined and readily-measured optical input/output ports. For simplicity, we first neglect the absorption and scattering loss, and begin with an n-port lossless system. RTOF implies that the optical force \mathbf{F} on the moving target is directly related to the change in the phase of the scattered ports as a function of the displacement \mathbf{r} ,

$$\mathbf{F}(\mathbf{r}) = -\frac{1}{\omega} \sum_{i=1}^n P_i(\mathbf{r}) \nabla_{\mathbf{r}} \phi_i(\mathbf{r}) \quad (3.1)$$

Here ω is the angular frequency of the incident optical beam; P_i and ϕ_i are the outgoing optical power and phase response at the i^{th} port, both driven by the scattering matrix of the system and the incident waves. The phase gradient $\nabla_{\mathbf{r}} \phi_i$ is calculated with respect to the movement of the movable object. Having taken into account that the curl of gradient of a scalar field vanishes, we derive the curl of the optical force \mathbf{F} as

$$\nabla_{\mathbf{r}} \times \mathbf{F}(\mathbf{r}) = -\frac{1}{\omega} \sum_i (\nabla_{\mathbf{r}} P_i) \times (\nabla_{\mathbf{r}} \phi_i) \quad (3.2)$$

The above outcome implies that, (A)if the sum of the curl products at all the output ports of the system adds up to zero for the entire range of interest of displacement \mathbf{r} , the optical forces are conservative. Multi-port systems are quite general as most networks have transmission port as well as reflection port. Polarization rotation enhanced at the resonance introduces even more output ports, making it practically impossible to maintain the sum of cross products to be zero. (B)Another special case having the power gradient parallel to the phase gradient at all output ports or forcing the optical power at every output

port to be constant no matter how the target moves is generally unrealizable in mechanically variable system. (C) Making the phase gradient to be zero, on the other hand, is trivial because no optical force is generated at all according to Eq.3.1 (we will later in Sec.3.2.3 prove that zero optical force is generated even when difference of phase gradients is constant in 2-port system). (D) The last and only peculiar scenario in which curl of the optical force is zero, regardless the complexity of the near-field distribution across the movable object, is a lossless system with a single output port, i.e. the output power is constant and equal to the incident optical power. The optical force, however, is not zero and proportional to the gradient of the scalar phase field, $\mathbf{F} = -(P_{in}/\omega)\nabla\phi$.

To illustrate conservative optical force in lossless single-port system, we consider the optical forces exerting on the dielectric photonic crystal slab (Fig. 3.1(a)) moving in XY-plane, with the goal of aligning these two photonic crystal slabs automatically with sub-nanometer scale resolution. The dielectric PC slab on the top, made of a *rectangular* lattice of air holes in silicon ($\epsilon = 12.25$), is supported by a metallic PC slab made of an identical lattice of rods atop the metallic substrate. The dimension of the unit cell is deliberately chosen to be $1a \times 1.4a$ rectangle (a being the lattice constant along the X-direction), to break the degeneracy of the guided resonance, and its importance will become apparent later in this chapter (Sec.3.2.4). The air holes in the upper slab are blind holes, with a radius of $0.1a$ and a depth of $0.4125a$, to ensure the upper slab is always supported by the metallic rod array beneath, irrespective of the displacement. The metallic PC slab is made of rods with a radius of $0.1a$ and a

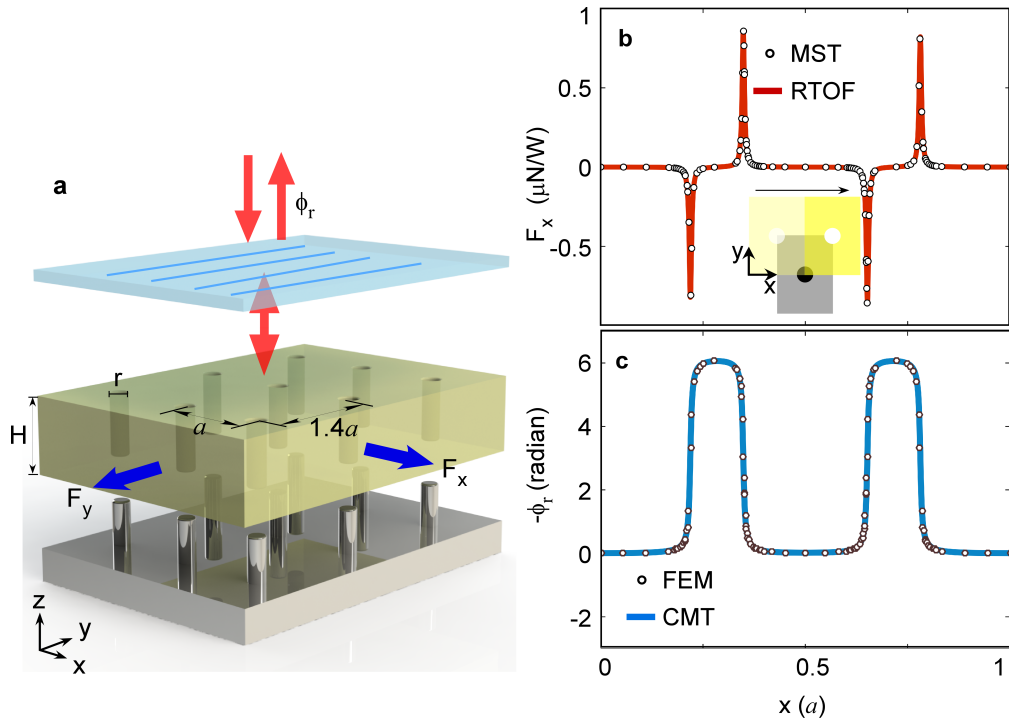


Figure 3.1: (a) Schematics of two photonic crystal slabs (a dielectric one shown in yellow and a metallic one shown in grey) to be self-aligned optically in the xy -plane. The incident light is a plane wave from the top along z -direction, and travels through a polarizing reflector (shown in blue). (b) Calculated optical force (x -component) on the upper photonic crystal slab and (c) the negative phase response of the reflection, as a function of its displacement along x direction as shown in the inset. Y -displacement is set to be 0

height of $0.275a$. To save computational power, the perfect electric conductor (PEC) is used to simulate the metallic surface with no loss and complete reflection. In practical experiment, 3D photonic crystals [42, 80] with complete band gap, or omnidirectional reflector [86] can replace the metallic substrate without affecting the conclusion. Since the structure is illuminated by a plane wave polarized along x-direction, a polarizing reflector colored in blue is used to prevent the light polarized along y-direction from leaking above [5, 16, 49], as polarization rotation induced by non-centrosymmetric PC slab stack will open another port to this system.

The calculated optical force on the upper PC slab (Fig. 3.1b) in the abovementioned one-port system shows very localized one-dimensional potential wells (Fig. 3.1c) along x-direction (y -displacement = 0), which are also periodic and can be used to confine the PC slab on top. The optical forces are calculated using the response theory, which agrees perfectly with the first-principle calculation using either the Maxwell stress tensor (MST) or Kelvin force formalism (see Chapter 2). Not only does the response theory simplify the force computation in that it only requires the phase of the outgoing wave (the reflected wave in Fig. 3.1a), i.e. $\mathbf{F} = -(1/2\omega)A\sqrt{\epsilon_o/\mu_o}|E|^2\nabla\phi$, where A is the cross-section area of one unit cell, ϕ is the phase of the reflected wave, but also provides more straightforward design insight with the aid of temporal coupled mode theory when extracting the phase response. In this one-dimensional case where y -displacement is fixed at zero, the negative phase spectrum is proportional to the scalar potential established by the optical

force. The supported PC slab can be trapped in the potential centering at $x = 0$ or $0.5a$, and the potential width can be narrowed by tuning the operating frequency. This approach further benefits from the high cavity Q-factor which is important in optical positioning with ultra-high spatial resolution of manipulation. Note that since the accuracy of CMT improves with higher cavity Q factor, excellent agreement between RTOF and MST in Fig 3.1b, which is deliberately chosen as a low-Q case with relatively wider force peaks, convinces us to rely on CMT to predict and design the force potential in remaining regions with higher Q factor.

3.2.2 Port number in various stacking photonic crystal slabs systems

In this section, I will present the temporal CMT for the most common structure of two stacking photonic crystal slabs which presents reflection, transmission, polarization conversion, and multiple fano-resonances simultaneously. Temporal CMT is particularly accurate for high-Q coupled waveguide or guided resonance systems so as to eliminate the necessity of finite-element simulation, and more importantly, provides more intuitive insight of force field shape. The most comprehensive temporal CMT presented in this section provides a thorough insight and a clear answer to why the lossless reflective substrate and polarizer in our proposed schematic are indispensable. The complete understanding of stacking photonic crystal slabs also helps to determine the sufficient conditions of realizing total reflection. Since the resonant frequency of high-Q guided resonance in stacking photonic crystal slabs is a function

of relative displacement of these two slabs, it has a potential application in tunable optical filter.

For two stacking slabs without holes on them, the polarization rotation does not exist in this kind of structure if the dielectric medium is isotropic. The transfer equation without micro-resonator can be written as

$$\begin{bmatrix} S_{1-}^x \\ S_{1-}^y \\ S_{2-}^x \\ S_{2-}^y \end{bmatrix} = \begin{bmatrix} r_d & 0 & t_d & 0 \\ 0 & r_d & 0 & t_d \\ t_d & 0 & r_d & 0 \\ 0 & t_d & 0 & r_d \end{bmatrix} \begin{bmatrix} S_{1+}^x \\ S_{1+}^y \\ S_{2+}^x \\ S_{2+}^y \end{bmatrix} \quad (3.3)$$

where subscripts 1 and 2 in Eq. 3.3 correspond to physically existent waveguides 1 and 2, respectively, which can be alternatively interpreted as free spaces above and below the stack. S_- denotes outgoing propagation modes and S_+ stands for incoming propagation modes. Two polarizations are presented by x and y, meaning x-polarization and y-polarization. r_d and t_d in Eq. 3.3 are complex values which should take Fabry-Perot background into account to make sure energy conserves, i.e. $C^\dagger C = I$ where C is the 4×4 transfer matrix [23]. The slow-varying Fabry-Perot background reflection and transmission coefficients depend on effective permittivity and effective thickness of stacking layers which are determined by medium property and structure.

Cavity modes excited in micro-resonators, which can be drilled periodic hole array on each slab, can be coupled into any ports regardless their polarization. In Fig. 3.2(a), the stacking photonic crystal slabs is illuminated by a plane wave polarized along x-direction. At a frequency far away from the resonant modes, the sum of reflection and transmission measured

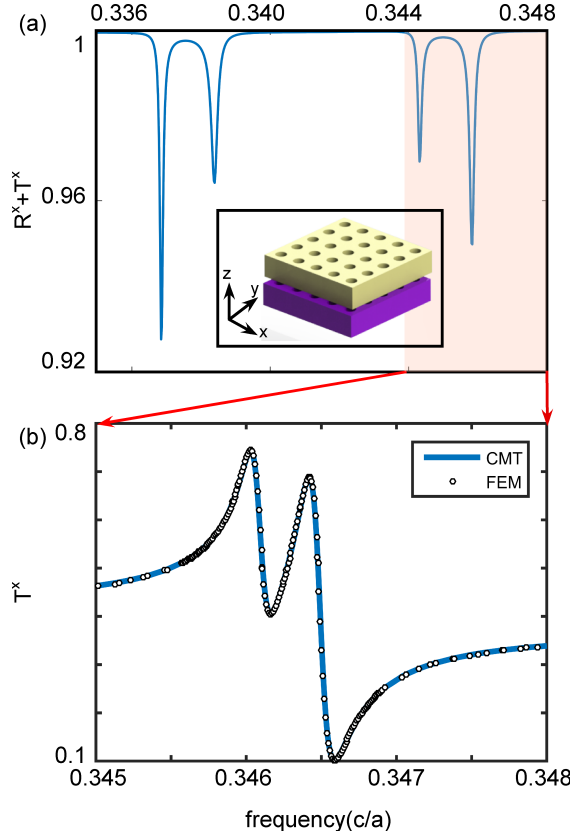


Figure 3.2: Polarization rotation happening in stacking photonic crystal slabs at resonances. (a) The top and bottom slabs (inset) are both made of silicon with $\epsilon_r = 12.25$, and with identical thickness of $0.55a$ and air holes with radius of $0.1a$, where a is the lattice constant. The incident plane wave has polarization along x-direction, and the sum of reflection and transmission polarized along x-direction is calculated in finite-element method when x-displacement = $0.11a$ and y-displacement = $0.17a$, which is less than 1 when polarization rotation happens as a result of coupling between resonant modes and propagating modes. (b) perfect agreement between finite-element calculation and 4-port coupled-mode theory in computing transmission coefficient along x-polarization.

on x-polarization is 1 because two polarizations cannot talk to each other through resonant modes. On resonances, the cavity modes are coupled into waveguides polarized along both x-direction and y-direction, resulting in power leakage into y-polarization. Suppose there are two resonant modes, the dynamic response equation describing the interaction between localized modes and propagation modes can be written as

$$\left\{ \begin{array}{l} \frac{d}{dt} \begin{bmatrix} A \\ B \end{bmatrix} = \begin{bmatrix} j\omega_A & 0 \\ 0 & j\omega_B \end{bmatrix} \begin{bmatrix} A \\ B \end{bmatrix} - \mathbf{\Gamma} \begin{bmatrix} A \\ B \end{bmatrix} + \mathbf{K}^T \begin{bmatrix} S_{1+}^x \\ S_{1+}^y \\ S_{2+}^x \\ S_{2+}^y \end{bmatrix} \\ \begin{bmatrix} S_{1-}^x \\ S_{1-}^y \\ S_{2-}^x \\ S_{2-}^y \end{bmatrix} = \begin{bmatrix} r_d & 0 & t_d & 0 \\ 0 & r_d & 0 & t_d \\ t_d & 0 & r_d & 0 \\ 0 & t_d & 0 & r_d \end{bmatrix} \begin{bmatrix} S_{1+}^x \\ S_{1+}^y \\ S_{2+}^x \\ S_{2+}^y \end{bmatrix} + \mathbf{D} \begin{bmatrix} A \\ B \end{bmatrix} \end{array} \right. \quad (3.4)$$

where A and B are localized mode amplitudes with corresponding resonant frequencies ω_A and ω_B . The 2×2 decay matrix $\mathbf{\Gamma}$ has complex off-diagonal elements if two cavity modes do not decay completely in phase or out of phase into waveguides 1 and 2. This situation is quite general as the mirror symmetry along z-direction is broken when these two photonic crystal slabs are mismatched. \mathbf{K} is the waveguide-to-resonator transfer matrix which is only determined by material properties and structural geometry. Similarly, another resonator-to-waveguide transfer matrix \mathbf{D} depicts the progress of how localized modes are coupled into external waveguides.

The coupling matrices \mathbf{K} and \mathbf{D} are essential to explain the phenomenon of polarization rotation caused by coupling between cavity modes and waveguide modes, in addition to regular reflection and transmission. To capture all

the possible coupling features in most complicated stacking photonic crystal slabs system, the coupling matrix \mathbf{D} is expressed using 8 sets of unique decay rates and coupling phases as

$$\mathbf{D} = \begin{bmatrix} \sqrt{2\gamma_{A1}^x} e^{i\theta_{A1}^x} & \sqrt{2\gamma_{B1}^x} e^{i\theta_{B1}^x} \\ \sqrt{2\gamma_{A1}^y} e^{i\theta_{A1}^y} & \sqrt{2\gamma_{B1}^y} e^{i\theta_{B1}^y} \\ \sqrt{2\gamma_{A2}^x} e^{i\theta_{A2}^x} & \sqrt{2\gamma_{B2}^x} e^{i\theta_{B2}^x} \\ \sqrt{2\gamma_{A2}^y} e^{i\theta_{A2}^y} & \sqrt{2\gamma_{B2}^y} e^{i\theta_{B2}^y} \end{bmatrix} \quad (3.5)$$

Based on the time reversal symmetry (see Appendix B), we can derive $\mathbf{K} = \mathbf{D}$ and $\mathbf{CD}^* = -\mathbf{D}$. The latter can be expanded as

$$\begin{aligned} & \begin{bmatrix} r_d & 0 & t_d & 0 \\ 0 & r_d & 0 & t_d \\ t_d & 0 & r_d & 0 \\ 0 & t_d & 0 & r_d \end{bmatrix} \begin{bmatrix} \sqrt{2\gamma_{A1}^x} e^{-i\theta_{A1}^x} & \sqrt{2\gamma_{B1}^x} e^{-i\theta_{B1}^x} \\ \sqrt{2\gamma_{A1}^y} e^{-i\theta_{A1}^y} & \sqrt{2\gamma_{B1}^y} e^{-i\theta_{B1}^y} \\ \sqrt{2\gamma_{A2}^x} e^{-i\theta_{A2}^x} & \sqrt{2\gamma_{B2}^x} e^{-i\theta_{B2}^x} \\ \sqrt{2\gamma_{A2}^y} e^{-i\theta_{A2}^y} & \sqrt{2\gamma_{B2}^y} e^{-i\theta_{B2}^y} \end{bmatrix} \\ &= - \begin{bmatrix} \sqrt{2\gamma_{A1}^x} e^{i\theta_{A1}^x} & \sqrt{2\gamma_{B1}^x} e^{i\theta_{B1}^x} \\ \sqrt{2\gamma_{A1}^y} e^{i\theta_{A1}^y} & \sqrt{2\gamma_{B1}^y} e^{i\theta_{B1}^y} \\ \sqrt{2\gamma_{A2}^x} e^{i\theta_{A2}^x} & \sqrt{2\gamma_{B2}^x} e^{i\theta_{B2}^x} \\ \sqrt{2\gamma_{A2}^y} e^{i\theta_{A2}^y} & \sqrt{2\gamma_{B2}^y} e^{i\theta_{B2}^y} \end{bmatrix} \end{aligned} \quad (3.6)$$

Noting that only half of these 8 equations are independent as they can be divided into 4 equivalent sets of equations having the same solution with the form as $\sqrt{2\gamma_2} e^{i\theta_2} = \frac{r_d^2 - t_d^2}{t_d} \sqrt{2\gamma_1} e^{-i\theta_1} + \frac{r_d}{t_d} \sqrt{2\gamma_1} e^{i\theta_1}$, the coupling matrix \mathbf{D} can be expressed only in terms of decay rates of mode A as

$$\mathbf{D} = \begin{bmatrix} \sqrt{2\gamma_{A1}^x} e^{i\theta_{A1}^x} & \sqrt{2\gamma_{B1}^x} e^{i\theta_{B1}^x} \\ \sqrt{2\gamma_{A1}^y} e^{i\theta_{A1}^y} & \sqrt{2\gamma_{B1}^y} e^{i\theta_{B1}^y} \\ \frac{r_d^2 - t_d^2}{t_d} \sqrt{2\gamma_{A1}^x} e^{-i\theta_{A1}^x} + \frac{r_d}{t_d} \sqrt{2\gamma_{A1}^x} e^{i\theta_{A1}^x} & \frac{r_d^2 - t_d^2}{t_d} \sqrt{2\gamma_{B1}^x} e^{-i\theta_{B1}^x} + \frac{r_d}{t_d} \sqrt{2\gamma_{B1}^x} e^{i\theta_{B1}^x} \\ \frac{r_d^2 - t_d^2}{t_d} \sqrt{2\gamma_{A1}^y} e^{-i\theta_{A1}^y} + \frac{r_d}{t_d} \sqrt{2\gamma_{A1}^y} e^{i\theta_{A1}^y} & \frac{r_d^2 - t_d^2}{t_d} \sqrt{2\gamma_{B1}^y} e^{-i\theta_{B1}^y} + \frac{r_d}{t_d} \sqrt{2\gamma_{B1}^y} e^{i\theta_{B1}^y} \end{bmatrix} \quad (3.7)$$

Replacing \mathbf{K} in the first equation of Eq. 3.4 by \mathbf{D} and assuming harmonic

cavity modes, the transfer matrix \mathbf{S} is found to be

$$\mathbf{S} = \mathbf{C} + \mathbf{D} \left[\left(\begin{bmatrix} j(\omega - \omega_A) & 0 \\ 0 & j(\omega - \omega_B) \end{bmatrix} + \mathbf{\Gamma} \right)^{-1} \mathbf{D}^T \right] \quad (3.8)$$

where the decay rate matrix $\mathbf{\Gamma}$ is related to the coupling matrix \mathbf{D} via conclusion from energy conservation law, i.e. $\mathbf{D}^\dagger \mathbf{D} = 2\mathbf{\Gamma}$ (\dagger stands for complex conjugate).

To summarize, the stack of two photonic crystal slabs is a 4-port system indicated by coupled-mode theory, which agrees perfectly with finite-element calculation as shown in Fig. 3.2(b). The transmission port can be easily eliminated by a complete reflective mirror from the bottom. The polarization rotation does not occur if the structure presents an in-plane centro-symmetry [81], but it will not generate any optical force if only translational motion happens, which is not suitable for self-alignment. The other possibility of removing polarization rotation while generating conservative optical force simultaneously is to use a lossless polarizer as we proposed in Fig. 3.1.

3.2.3 Inevitable non-conservative optical force in multi-port system

To show the necessity of the single-port operation, i.e. with the use of the metal rods substrate and the polarizer on the top, we reveal the non-conservativeness of optical force in multi-port system. Multi-port system is quite general in reality as most photonic crystal slabs fabricated on transparent SOI or GaAs wafers are multi-port system, because the in-plane central-asymmetry of dislocated slabs causes polarization rotation and the dislocation

of stacking PC slabs causes the cavity modes to scatter with different decay rates upwards and downwards[81].

The conservative nature of optical force can be broken, i.e. non-zero conservative force field cannot be established otherwise it must contain non-conservative component, if we only remove the polarizer above as it opens another port for y-polarization. To simplify the analysis of the counter-example, we assume the resonant cavity only has a single mode A . The corresponding temporal coupled-mode theory for this 2-port single-mode system is revised to be

$$\begin{cases} \frac{d\mathbf{A}}{dt} = -i\omega_A\mathbf{A} - \gamma_A\mathbf{A} + \mathbf{K}^T \begin{bmatrix} S_{1+} \\ S_{2+} \end{bmatrix} \\ \begin{bmatrix} S_{1-} \\ S_{2-} \end{bmatrix} = e^{i\phi}\mathbf{C} \begin{bmatrix} S_{1+} \\ S_{2+} \end{bmatrix} + \mathbf{D}\mathbf{A} \end{cases} \quad (3.9)$$

The matrix \mathbf{C} is an identity matrix due to total reflection. The 2×1 vertical vector \mathbf{D} represents the coupling coefficients from cavity mode to the outgoing waveguide modes. The subscripts of 1 and 2 correspond to 2 ports denoting orthogonal polarizations. Suppose only port 1 is excited, the normalized field intensities at port 1 and port 2 are derived as

$$\begin{cases} I_{11} = \frac{(\omega-\omega_o)^2+(\gamma_1-\gamma_2)^2}{(\omega-\omega_o)^2+(\gamma_1+\gamma_2)^2} \\ I_{21} = \frac{4\gamma_1\gamma_2}{(\omega-\omega_o)^2+(\gamma_1+\gamma_2)^2} = 1 - I_{11} \end{cases} \quad (3.10)$$

The corresponding phase responses at port1 and port2 are computed as

$$\begin{cases} \tan(\Phi_{11}) = -\frac{2\gamma_1(\omega-\omega_o)}{(\omega-\omega_o)^2+(\gamma_1^2-\gamma_2^2)} \\ \tan(\Phi_{21}) = \frac{\omega-\omega_o}{\gamma_1+\gamma_2} \end{cases} \quad (3.11)$$

One can verify that the energy is conservative from Eq. 3.10, and thus the curl of the optical force based on RTOF is found to be

$$\nabla \times \mathbf{F} = -\frac{P_{in}}{\omega} \nabla I_{11} \times \nabla(\Phi_{11} - \Phi_{21}) \quad (3.12)$$

Due to polarization rotation, the outgoing wave intensity I_{11} is not constant because the ratio of energy dissipated into each polarization changes with the geometry. Therefore, from Eq. 3.12 we draw the conclusion that the gradient of I_{11} has to be parallel with the gradient of $\Phi_{11} - \Phi_{21}$ to ensure conservative optical force, which is generally not satisfied in most systems. To take a step further to check whether $\Phi_{11} - \Phi_{21}$ can always be constant for any frequency, we calculate the tangent of $\Phi_{11} - \Phi_{21}$ to be

$$\tan(\Phi_{11} - \Phi_{21}) = \frac{\omega - \omega_o}{\gamma_1 - \gamma_2} \quad (3.13)$$

It is obvious that if and only if $\gamma_1 = \gamma_2$, one can deduce $\Phi_{11} - \Phi_{21} = \pi/2$. However, due to the out-of-plane asymmetry of PC slab stacking configuration, the decay rates along two polarizations are different. Moreover, the same requirement results in $\tan(\Phi_{11}) = 1/\tan(\Phi_{21})$ based on Eq. 3.11, which indicates that $\Phi_{11} + \Phi_{21} = \pi/2$. Since the continuously transited phase responses are actually fixed (instant π phase transition is prohibited), no optical force can be generated in such a system. Therefore, even in this simplest 2-port system, the optical force field is generally non-conservative, which is not suitable to precisely and stably align photonic crystal layers. However, non-conservative nature of optical force in a multi-port system is promising to build optical micro-motors.

3.2.4 Tailoring conservative optical force field established in one-port system

Knowing that only single-port system is suitable for automatic alignment with ultra-high spatial resolution as well as absolute stability, we use the CMT to analyze the spatial dependence of resonant frequency $f(x, y)$ and decay rate $\gamma(x, y)$ based on which the desired optical force potential can be shaped. In the first step, the exact values of resonant frequencies and decay rates are extracted from the least-squared fitting with the reflection spectra, which are from first-principle finite-element simulation results, over the entire 2D displacement of the upper PC slab. After the parameter maps of CMT framework have been determined, we then tailor the desired force potential simply by tuning the frequency.

The structure shown in Fig. 3.1a supports a number of guided resonances at normal incidence denoted by A and B and one port coupled with two external modes S_{\pm} ($+$ denotes incoming propagation mode and $-$ denotes outgoing propagation mode). At a frequency far away from the resonances of the cavity, amplitude of the outgoing wave S_- only experiences a constant phase delay with respect to the incoming wave, i.e. $S_- = e^{i\phi_o} S_+$. The phase ϕ_o is real-valued in a lossless system. Near the resonant frequencies of the optical cavity, the cavity mode is excited and the corresponding coupled-mode equation is [74]

$$\begin{cases} \frac{d}{dt} \begin{bmatrix} A \\ B \end{bmatrix} = -i \begin{bmatrix} \omega_A & 0 \\ 0 & \omega_B \end{bmatrix} \begin{bmatrix} A \\ B \end{bmatrix} - \begin{bmatrix} \gamma_A & \gamma_o \\ \gamma_o^* & \gamma_B \end{bmatrix} \begin{bmatrix} A \\ B \end{bmatrix} + \mathbf{K}^T S_+ \\ S_- = e^{i\phi_o} S_+ + \begin{bmatrix} \sqrt{2\gamma_A} e^{i\theta_A} & \sqrt{2\gamma_B} e^{i\theta_B} \end{bmatrix} \begin{bmatrix} A \\ B \end{bmatrix} \end{cases} \quad (3.14)$$

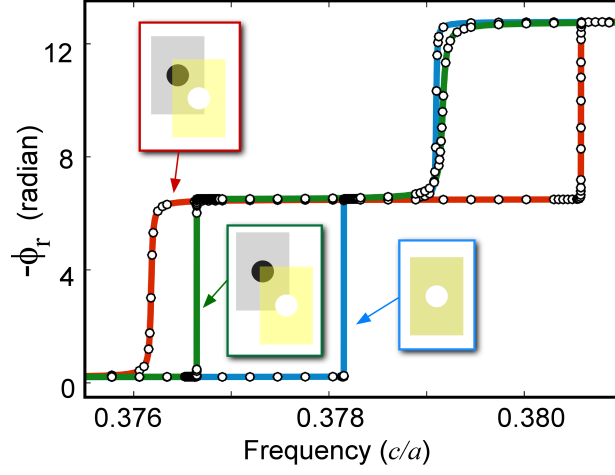


Figure 3.3: Calculated phase spectra of the reflected light at three lateral offsets: $(0a, 0a)$ (blue), $(0.5a, -0.7a)$ (green), and $(0.25a, -0.35a)$ (red). Insets show the relative positions of the two photonic crystal slabs. Results from first-principle finite-element calculations (dots) are fitted to the coupled-mode theory (curves).

where $\omega_{A,B}$ are resonant angular frequencies of the two cavity modes respectively indicated by subscripts, A and B are complex-valued localized cavity modes including the phase information, γ_A and γ_B are real-valued decay rates of these two cavity modes respectively, $\gamma_o D$ is related to γ_A and γ_B by energy conservation law, and the 1×2 complex coupling matrix \mathbf{K} represents the amount of incident wave coupled into cavity.

Through time-reversal symmetry and energy conservation, the reflection coefficient of this single-port multi-mode system has an all-pass response

with unitary amplitude

$$S = \frac{S_-}{S_+} = e^{i\phi_0} \left(1 + \frac{2i\gamma_A(\omega - \omega_B) + 2i\gamma_B(\omega - \omega_A)}{- (\omega - \omega_A)(\omega - \omega_B) - i\gamma_A(\omega - \omega_B) - i\gamma_B(\omega - \omega_A)} \right) \quad (3.15)$$

Obviously, the phase of reflection coefficient S only depends on the resonant frequencies $\omega_{A,B}$ and decay rates $\gamma_{A,B}$ which vary with the movement of the top photonic crystal slab. Generally, increasing 2π phase transition of reflectivity occurs around the resonances (Fig.3.3). Note that the phase spectra are inversed in Fig.3.3 so that phase maps presented later are directly proportional to optical force potential to provide straightforward view in the remaining part of this article. As the resonant frequency, a strong function of the displacement of the top photonic crystal slab, varies around the fixed frequency of illumination, the 2π phase transition subsequently happens in real space of displacement (Fig 3.1c). In contrast, the operating frequency away from the resonant frequency lacks any pronounced potential barriers or wells. More specifically, around the lower resonance in Fig. 3.3, the lower bound of red curve and upper bound of blue curve give a good illustration of defining the range of operating frequency from $0.3759(c/a)$ to $0.3786(c/a)$. Throughout the process, $\omega_{A,B}$ and $\gamma_{A,B}$ are accurately fitted by making phase spectra with perfect agreement with finite-element simulations.

The offset between the two slabs has a drastic impact on the resonant frequency and decay rate, which can be fitted from the FEM calculation of reflectivity at a few frequencies over the entire unit cell (Fig. 3.4, thereby allowing us to interpolate and extrapolate the phase response over a wide range

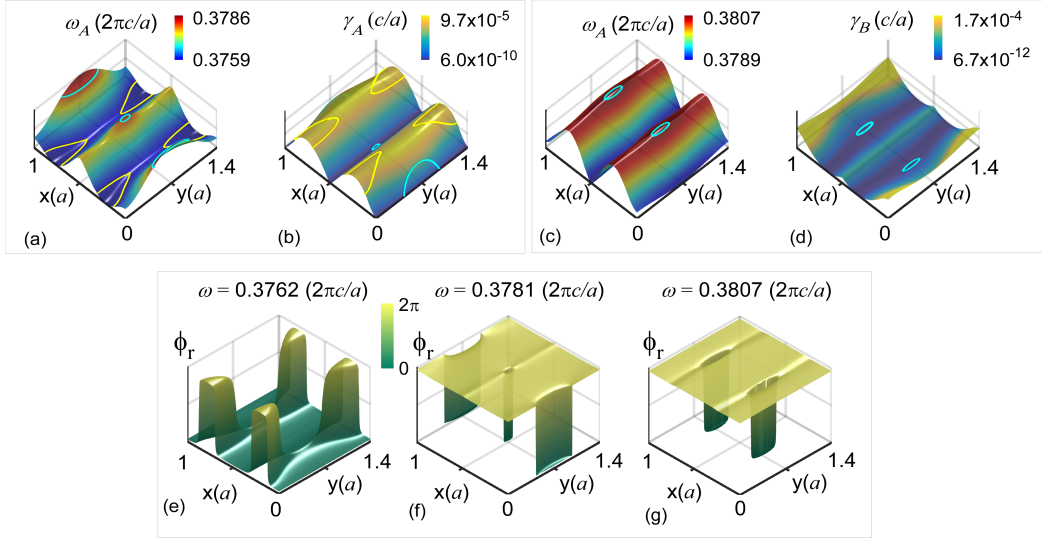


Figure 3.4: Calculated displacement-dependent resonance frequency, decay rate and phase response (optical potential) (a-d) Resonant frequency ω and decay rate γ for Mode A and B as a function of the x-y displacement of the upper photonic crystal slab. The frequency contour of frequency of $0.3762(c/a)$ is plotted in yellow in (a) with corresponding decay rates in yellow in (b). The cyan frequency contour in (a) corresponds to frequency of $0.3781(c/a)$ with the corresponding decay rates in cyan as well in (b). The frequency contour of $0.3807(c/a)$ is plotted in cyan in (c) with corresponding decay rates plotted in cyan in (d). (e) (g) Corresponding phase response of the reflection for frequencies of 0.3762 (c/a), $0.3781(c/a)$, and $0.3807(c/a)$.

of frequencies and spatial displacements. For instances, two frequency contours of $0.3762(c/a)$ and $0.3781(c/a)$ are plotted in yellow and cyan respectively in Fig. 3.4a and another higher frequency contour for $0.3807(c/a)$ is plotted in cyan in Fig. 3.4c. These frequency contours coincide with the edge shapes of phase maps of corresponding frequencies as shown in Fig. 3.4e-g which are actually proportional to the optical force potential (note that the phase maps are already inverted). This is crucial for constructing desired force potential with ideal shape at desired location that expels or traps the movable object. The potential mesas in Fig. 3.4e prevents the movable photonic crystal slab from entering the top platform regions. Perfect alignment without misplacement of top photonic crystal slab with substrate can be achieved by constructing a potential well right in the center as shown in Fig. 3.4f. At the same frequency, total misplacement of $0.5a$ can be realized as well. Trapping the photonic crystal slab to another position besides 0 or $0.5a$ is also realizable by utilizing higher resonance as shown in Fig. 3.4g. One can further increase the frequency to reach even higher resonances to construct desired force potential, which are not show here.

To construct potential wells or plateaus, we simply choose frequency contours which encircle resonant frequency peaks or basins on Fig. 3.4a, c. Cyan frequency contours of illumination frequency illustrate how to build potential wells clearly. As the frequency of illumination is lower than all the resonant frequencies inside the contour, at those displacements the operating frequency is lower than the resonance and therefore 2π upward phase jump

has not happened yet, which can be obviously seen in Fig. 3.3. As a result, the phases at positions within the cyan contours are 2π lower than those at positions elsewhere. The alignment resolution is determined by the sharpness of potential well edges which is proportional to the decay rates at that position, i.e. $\Delta r = 2\gamma/\nabla_r\omega$. The decay rates on the potential edges for an operating frequency can be found on the surfaces of decay rate maps along the pathway of projection of iso-frequency contour on the xy-plane. In Fig. 3.4b and Fig. 3.4d, the winding curves of decay rates are shown in the same color of corresponding iso-frequency contour. It is evident that the decay rates on cyan curves corresponding to frequency of $0.3781(c/a)$ are lower than those on yellow curves corresponding to frequency of $0.3762(c/a)$ in Fig. 3.4a, and thus the alignment resolution is also improved via increasing operation frequency. When the movable object is trapped to perfect position, in which the phase map is similar to that in Fig. 3.4f, the alignment resolution achieved can be as small as $7 \times 10^{-4}a$, which is efficient for sub-nanoscale auto-alignment for photonic crystal slabs with lattice constant up to $1.4\mu m$. Additionally, the sharp edges of potential produces strong optical force to align the PC slab at moderate input power.

The use of rectangular unit cell here is intentional to simplify the design of force potential landscape, as it separates two high-Q cavity modes far away from each other in frequency domain, and therefore only one set of resonant frequency map and decay rate map is needed for predicting force potential at the frequency of interest. As seen in Fig. 3.3, the well-spaced

low-frequency resonance and high-frequency resonance never exchange their positions in spectrum thanks to the 1.4×1 rectangular unit cell. As the contour line for a specific frequency only appears on either ω_A map in Fig. 3.4a or ω_B map in Fig. 3.4c, one does not need to refer to both resonant frequency maps simultaneously when designing the desired force potential.

3.3 Quantification of conservativeness of optical force via Helmholtz-Hodge decomposition

The perfectly conservative force field predicted in theory does not exist because of the parasitic unintended ports either from loss or depolarization. However, the non-conservative component of the force field can be suppressed to levels orders of magnitude smaller than that of the conservative component. It is therefore important to develop techniques that can decompose an arbitrary force field, and quantitatively compare the levels of conservative and non-conservative components. This comparison also provides a numerical proof to the prediction from the response theory that single-port system generates conservative forces, up to the numerical error from spatial discretization. To this end, we apply Helmholtz-Hodge decomposition (HHD) which has been well developed for computational fluid dynamics[87].

In this section, I present an easy-to-implement HHD to decompose periodic optical force field into scalar optical force potential and scalar optical force stream, from which we can judge the conservativeness of optical force through appropriate figure of merit and extract the phase gradient singularities

when optical vortex exists.

3.3.1 Introduction to Helmholtz-Hodge decomposition

Any vector field which is well defined (second-order integral exists) within fixed domain and fulfills certain boundary conditions (various valid boundary conditions will be discussed later) can be uniquely decomposed into curl-free component (irrotational) component, divergence-free (solenoidal) component, and the remaining harmonic term by Helmholtz-Hodge decomposition as

$$\mathbf{u} = \mathbf{u}_{\parallel} + \mathbf{u}_{\perp} + \mathbf{h} = \nabla\phi + \nabla \times \psi + \mathbf{h} \quad (3.16)$$

where \mathbf{u}_{\parallel} and \mathbf{u}_{\perp} denote curl-free and divergence-free components respectively, and the remaining harmonic component is represented by \mathbf{h} . The curl-free part can be interpreted as the sink or source of energy flow, while the divergence-free part carries circulating energy.

Various numerical methods of HHD with or without mesh have been proposed in the past decade. For example, Least-square Finite-element Method (LS-FEM) which only works for triangular mesh was proposed in 2003 [Polthier et.al.] and soon later applied to rectangular lattice by Guo et. al. However, a regularization weight has to be introduced to derive unique solution because the rank of $N \times N$ stiffness matrix is $N - 1$ and these methods are only suitable for so-called normal-parallel (N-P) boundary condition, i.e. curl-free component is normal to boundary and divergence-free component is parallel to boundary. Curl-free and divergence-free wavelets method can be applied

to periodic vector field, but this algorithm is hard to be parallelized as it is based on iteration method. In this section, I propose to use Greens Function Method to decompose periodic vector field, which can be applied to arbitrary mesh and ideal for parallelization on supercomputer. HHD based on Greens Function Method was first proposed by Li [34] to segment aperiodic discrete vector field to aid computer vision. Here we extend this method to periodic case under what condition we demonstrate the uniqueness of HHD and perform critical error analysis, from which the conservativeness of optical force field can be judged.

3.3.2 Helmholtz-Hodge decomposition using Green's function method

According to [34] the curl-free potential can be expressed as discrete convolution between the gradient of Greens function and the original vector field

$$\phi(r_i) = \sum_j [\nabla G(r_i - r_j) \cdot \mathbf{u}(r_j)] \quad (3.17)$$

where r_i is the location where the curl-free potential is calculated and r_j is scanning all locations in the space, and $\mathbf{u}(r_j)$ is the original vector at the location r_j . Similarly but not identically, the divergence-free potential can be derived from

$$\psi(r_i) = \sum_j [\nabla \times G(r_i - r_j) \cdot \mathbf{u}(r_j)] \quad (3.18)$$

where G is the Greens Function and particularly in 2-dimension it is defined as

$$G(r_i - r_j) = -\frac{1}{2\pi} \ln(|r_i - r_j|) \quad (3.19)$$

The harmonic component does not exist in periodic force field as will be discussed in uniqueness theorem in the next section. Even though Li et al only deals with aperiodic boundary condition, it is straightforward to extend Eq. 3.17) to periodic boundary condition where the decomposition is unique as we demonstrated before

$$\phi(r_i) = \sum_{m,n=-\infty}^{\infty} \left[\sum_{j_{m,n}} \nabla G(r_i - r_{j_{m,n}}) \cdot u(r_{j_{m,n}}) \right] \quad (3.20)$$

where m and n denote m^{th} and n^{th} period along two perpendicular directions and they can go to infinity only in ideal case. $r_{j_{m,n}}$ is the recurring location of $r_{j_{0,0}}$ in the m^{th} and n^{th} period. The calculation of potentials at each position can be parallelized perfectly as it does not depend on potentials elsewhere. Since $\mathbf{u}(r_{j_{m,n}})$ are periodic, we can extract the vector field in the primary period (denoted by 0^{th} period) to rewrite Eq. 3.20 as

$$\phi(r_i) = \sum_{\substack{|r_{j_0}^x| \leq \frac{a}{2}, |r_{j_0}^y| \leq \frac{b}{2}}} \left\langle u(r_{j_{0,0}}) \cdot \left\{ \begin{array}{l} G[r_i - [r_{j_{0,0}} - (Ma, Nb)]] + \dots + G[r_i - [r_{j_{0,0}} - (a, b)]] \\ + G(r_i - r_{j_{0,0}}) + \\ G[r_i - [r_{j_{0,0}} + (a, b)]] + \dots + G[r_i - [r_{j_{0,0}} + (Ma, Nb)]] \end{array} \right\} \right\rangle \quad (3.21)$$

where a and b are the lattice constants of 2D photonic crystal slab, M and N are the numbers of single-sided truncation period. Similarly, the divergence-free component can be obtained from the spatial convolution between the curl of the Green's function and the force field, over the entire space. Such a folded Greens function allows us to simply increase the value of M and N to reduce the truncation error and realize more than 80dB of numerical dynamic range.

3.3.3 Uniqueness of Helmholtz-Hodge decomposition of periodic vector field

Given any arbitrary force field, it turns out to be conservative provided that no divergence-free component exists after HHD, if and only if the decomposition is unique. However, the harmonic term \mathbf{h} can also be expressed as the gradient of a scalar potential as $\nabla\beta$ where β satisfies the Laplacian equation $\nabla^2\beta$, and thus \mathbf{h} can be either included into curl-free component or divergence-free component without contributing any redundant qualities to the original field provided that $\nabla \times (\nabla\beta) = 0$ and $\nabla \cdot (\nabla\beta) = 0$. Since the solution to the Laplacian equation is not trivial, the uniqueness of Helmholtz-Hodge decomposition is not a necessary condition for all boundary conditions.

In contrast to HHD within a limited domain where appropriate boundary conditions must be presumed to find the harmonic function as a solution to the Laplacian equation, periodic boundary condition in actuality forces HHD to process the infinite domain. From another point of view, the harmonic term only depends on the vector flow outside the observed domain and there is no “outside” region if boundary is periodic. The solution to the Laplacian equation is either the minimal energy (constant Laplacian potential $\nabla\beta = C_{min}$ (e.g. $\Phi = x + y$) producing zero vector field) or surface relaxation state fulfilling mean value theory (e.g. $\Phi_t = x^2 - y^2$) without local maxima or minima. Obviously, the surface relaxation state does not satisfy the periodic boundary condition, and thus no harmonic term contains in periodic force field.

The orthogonality of decomposed curl-free component and divergence-

free component, as a result of zero harmonic term, is the sufficient condition of unique Helmholtz-Hodge decomposition, which is defined as zero overlap integral within a given volume

$$\int_V \mathbf{u}_{\parallel} \cdot \mathbf{u}_{\perp} dV = 0 \quad (3.22)$$

Eq. 3.22 can be interpreted as neither curl-free component nor divergence-free component contain harmonic term. Since $\nabla \cdot \mathbf{u}_{\perp} = 0$ and $\mathbf{u}_{\parallel} = \nabla\phi$ due to Gauss Theorem Eq. 3.22 can be rewritten as

$$\int_{\partial V} \phi \mathbf{u}_{\perp} \cdot \mathbf{n} dS = \int_{\partial V} \phi \frac{\partial \beta}{\partial n} dS = 0 \quad (3.23)$$

where ∂V is the boundary of volume V and \mathbf{n} is the unit vector normal to the boundary. Even though $\mathbf{u}_{\perp} \cdot \mathbf{n}$ is not trivial when ψ varies along the boundary, the integral adds up to zero under periodic boundary condition, which agrees with constant minimal energy β as we analyzed before. Therefore, the optical force field on periodic photonic crystal slab can be uniquely decomposed without worrying about the harmonic term.

3.3.4 Error convergence of Helmholtz-Hodge decomposition

Error analysis is essential to determine the appropriate figure of merit to examine the conservativeness of the optical force. For periodic optical force field, the linear dependence of error on the truncation period in log-log scale, rather than the dependence of error on resolution, can effectively indicate the conservativeness of optical force, because truncation error dominates among all types of errors. For conservative force without divergence-free component,

the error is estimated through Frobenius norm of decomposed divergence-free component normalized by total force as

$$E = \|u_{\perp}\|_F / \|u\|_F \quad (3.24)$$

where the Frobenius norm of a 2D discrete vector field is defined as

$$\|u\|_F = \sqrt{\sum_{i=1}^m \sum_{j=1}^n (u_{x,ij}^2 + u_{y,ij}^2)} \quad (3.25)$$

For conservative force field, Eq. 5.3 must approach to zero as resolution of discrete force field becomes higher or truncation period increases. In non-conservative case, Eq. 5.3 should converge to certain level well beyond zero as $\|u_{\perp}\|_F \neq 0$.

There are three types of errors in discrete HHD coming from the scaling factor in discrete Greens Function at singularity, the discretization of vector field, and the truncation of periodic force field. The scaling factor is deliberately introduced to avoid infinity at singularity so that the Greens Function is defined as

$$G(\mathbf{r}) = -\frac{1}{2\pi} \ln \left(\sqrt{|\mathbf{r}|^2 + \delta} \right) \quad (3.26)$$

Even though the minimum error can be achieved by sweeping the scaling factor δ , the value of δ minimizing the error also depends on the resolution, truncation period and the characteristic of vector field. Therefore, we keep using a reasonably small $\delta = 4.8329 \times 10^{-9}$ throughout this section for both conservative force and non-conservative force even when the resolution and truncation period are modified.

The second type of error comes from the discretization of a smooth vector field and thus is called discretization error. If decomposed properly, the numerator of Eq. 5.3 is estimated to be below $C(a/m)^p$ where C is a constant related to the vector field itself, a is the lattice constant in periodic field, m is the number of grids along one side, and p represents the rate of convergence [6]. In log-log scale, the error clearly shows a linear dependence on the resolution as

$$\log E = -p \cdot \log m + p \cdot \log a + \log C \quad (3.27)$$

However, when other types of errors exist, the linear dependence will be bent and converge to the magnitude of total error at higher resolution, and therefore it is not suitable to judge the conservativeness of the vector field based on this figure of merit.

The third type of numerical error called truncation error is as well unavoidable as the vector field has to be truncated at finite number of periods in programs. Similar to discretization error in Eq. 3.27, truncation error also has an upper bound for a given truncated period number M and N in Eq. 3.21, which is equivalent to state that the sum of Greens Function converges to certain value and it does as M and N go to infinity. It is straightforward to write out the truncation error in terms of solenoidal potential for conservative vector field as

$$E_T = \frac{\psi - \tilde{\psi}}{\psi} = \frac{\sum_{n=N}^{\infty} \left[\sum_{j_n} \nabla \times G(r_i - r_{j_n}) \cdot u(r_{j_n}) \right]}{\sum_{n=-\infty}^{\infty} \left[\sum_{j_n} \nabla \times G(r_i - r_{j_n}) \cdot u(r_{j_n}) \right]} \quad (3.28)$$

where Ψ is the decomposed divergence-free potential truncated at and one can define the truncation error for curl-free vector field similarly. Like discretization error, the truncation error, in conservative case, also presents a linear dependence on single-sided truncation period M and N in $\log - \log$ scale (See Appendix C).

Applying discrete HHD to numerically decompose optical force fields, we can reconstruct quite distinguishable divergence-free potentials as shown in Fig. 3.5(b) and (d) for one-port system and two-port system respectively. The vector potential $\Psi((r))$ for the one-port conservative system (Fig. 3.5c) vanishes, while $\Psi((r))$ oscillates between large positive and negative values in the two-port non-conservative system (Fig. 3.5d). Here, peaks of positive $\Psi((r))$ indicates that the upper PC slab is driven to rotate clockwise, while trough of negative $\Psi((r))$ indicates counter-clockwise rotation. The error convergence with respect to resolution m which is the number of grids along the longer side from 0 to b in log-log scale is plotted in Fig.3.5 (e) when the number of truncation period is set to be 20. Even though the error of conservative case is more than 3 orders lower than non-conservative case, we cannot judge the conservativeness of the optical force field as we do not know whether the redundancy is from divergence-free potential or other types of numerical error. Since at $N = 20$ truncation error overwhelms discretization error, we can clearly observe the linear dependence of error with respect to truncation period in conservative case from Fig. 3.5(f) when plotted in log-log scale. Around $N = 1000$, a minima is achieved after which the numerical error caused by

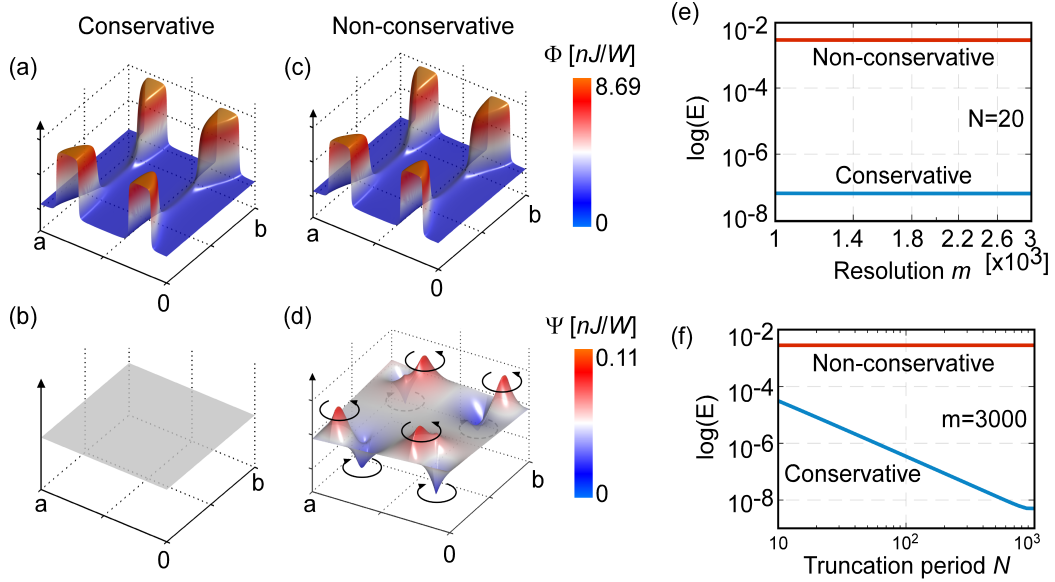


Figure 3.5: Decomposed curl-free potential Φ and divergence-free potential Ψ for conservative optical force and non-conservative optical force, and error convergence plot with respect to resolution m on longer side $[0, b]$ and truncation period N , respectively. (a)-(b) Decomposed potentials for conservative optical force in one-port system, and the divergence-free potential is almost flat when plotted in the same scale as non-conservative optical force in system without polarizer. (c)-(d) Decomposed potentials for non-conservative optical force with truncation period=20, and the vortex is obvious on divergence-free potential; (e) Error convergence with respect to number of grids on longer side in log-log scale. Due to existence of relatively large truncation error, both errors stop decreasing at the magnitude of truncation error. (f) Error convergence with respect to truncation period in log-log scale with resolution $m=3000$. Obviously, the error of conservative case linearly decrease with increasing truncation period.

machine precision limit will deteriorate the decomposition results.

The overall non-conservativeness level for a given force field can be further described by the rotational ratio, defined as the Frobenius norm of the rotational component divided by that of the total force, $\|\nabla \times \psi(\mathbf{r})\|_F / \|\mathbf{F}(\mathbf{r})\|_F$. Only when the value of N ($M=N$ in program) in Eq. 3.21 is sufficiently large to make the truncation error negligibly small, the rotational ratio for a conservative force field reduces to the discretization error. However, the rotational ratio for a non-conservative force field converges to the non-zero divergence-free component which is several orders of magnitude larger than both truncation error and discretization error, and thus does not depend on the value of N as shown in Fig. 3.5f. Therefore, directly based on the original force field, HHD demonstrates the conservativeness of optical force in one-port system which has already been analytically proved by RTOF. Moreover, due to tiny rotational component of optical force which is several orders smaller than irrotational counterpart in system without polarizer above, the above movable photonic crystal slab can still be trapped by conservative component of optical force but exhibits weak vibrations.

3.4 Computation Concerns

Generally speaking, 3D finite-element-method numerical simulation requires large RAM (usually $\geq 32GB$) and long time to derive the inverse matrix. Given current computing power (CPUs: Xeon E5-1650 and Xeon E3-1245), a distributed computation system is required to accelerate the computation

time. The distributed computation infrastructure is built on 4 servers connected with high-speed optical network. Since the parallel mechanism is realized using message-passing principle, there is no specific requirements on operating system or hardware (I do use different CPUs) on each server. The master node keeps sending query message to all the worker nodes, and once the simulation on some worker node is done the simulation results start to transfer to master node from the worker node. To minimize the necessary message passing through the network, only variables and results are transmitted. Therefore, each worker node has COMSOL server running and simulation scripts are broadcast at the very beginning of the whole simulation.

On the other side, we use Helmholtz-Hodge decomposition to demonstrate the optical force conservativeness numerically because as more and more constraints are added to the system such as polarization rotation, polarizer, multiple resonances, and unequal decay rates it becomes extremely difficult to analytically prove the conservativeness of the optical force. Even though this problem is provable, the proof time will be quite long given current CPU specifications. However, numerical demonstration also requires a lot of computation powers because the results shown in Fig. 3.5 has force field resolution of 3000×2143 (corresponding to 1.4×1 aspect ratio of unit cell) and maximum single-sided truncation period of 1000, which is equivalent to operate on matrices with dimension of 6000000×4286000 . Decomposition of such high matrix sequentially requires an extremely large RAM and quite long computation time. Therefore, I developed C++ codes to perform Helmholtz-Hodge decom-

position on Lonestar supercomputer of Texas Advanced Computing Center (TACC) using OpenMP library and MPI environment. The parallel MATLAB program for Helmholtz-Hodge decomposition is also developed to run on a multicore processor. One can compare and confirm the equality of these two programs by experimenting on a smaller vector field. Both codes are given in Appendix and free to use under GNU license.

3.5 Conclusion Remarks

The stack of two photonic crystal slabs is the essential part of realizing various applications such as self-alignment, completely reflective mirror, and optical filter. However, the temporal coupled-mode theory for the simplest two slab stack has not been reported up to date, which helps to understand the transmission behavior of such structure thoroughly. Combined with a perfect mirror substrate, the stack of photonic crystal slabs has a potential application in tunable optical filter as the resonant frequency depends on the relative position of the two slabs and photonic crystal slabs generally possess ultra-high Q-factor.

The presenting divergence-free potential in the absence of polarizer is extremely weak, account for up to 0.6% of the total power when the Q-factor is 6×10^8 . On the simulation side, the mesh and structure are both carefully optimized. During the data processing, the phase response is primarily fitted via least-squared curve fitting techniques, after which the least significant bits of resonant frequencies and decay rates into x - and y - polarizations are

further fined-tuned from the reflection coefficient spectra.

Chapter 4

Novel optical trapping in topological photonic integrated system

4.1 Introduction

One-way waveguide by breaking time reversal symmetry offers a revolutionary control of light flow direction and thus blazes a trail for a broad range of unprecedented applications on manipulating Micro-/Nano-structures and micro-fluid, which are extremely desired in Biology, Integrated Photonics, Cold Ions, and Microfluidic Devices. In this section we elaborate on the underlying mechanism of conservative optical force and related optical potential in uniform one-way waveguide, as well as present an example of controlling both the position and orientation of an asymmetric particle simultaneously benefitting from the force conservation.

4.2 Simultaneously trapping and orientation of asymmetric particle in unidirectional waveguide-resonator system

4.2.1 Conservative optical force in unidirectional waveguide-resonator system

In this chapter, we introduce a novel way to simultaneously trap and orientate an asymmetric dielectric particle in a hollow metal-box optical cavity coupled with a one-way waveguide mode (Fig. 4.1). A purely conservative optical gradient force field whose curl is zero, i.e. $\nabla \times \mathbf{F} = 0$, is constructed in the optical cavity to stably trap the particle to the optical intensity maxima. Although well-established Maxwell stress tensor (MST) and the Kelvin force give the macroscopic forms of calculating the optical force, they require the distributions of the electromagnetic field and dielectric constant which are complicated to derive the conservative optical force condition in the resonator-waveguide structure. Having been applied to many integrated photonic systems which can be described as an n-port system, the response theory of optical force (RTOF) is used here to relate the conservative optical force condition to a new set of physical quantities at the lumped ports [84]. In generality, a regular resonator-waveguide structure is a multi-port system in that most optical waveguides have backscattered propagation and multiple spatial modes. Neglecting the absorption and scattering loss, in RTOF scheme the optical force on a movable particle in a multi-port resonator-waveguide system is computed based on the power and the changes in phase response of the scattered waves as a function of the particle displacement r

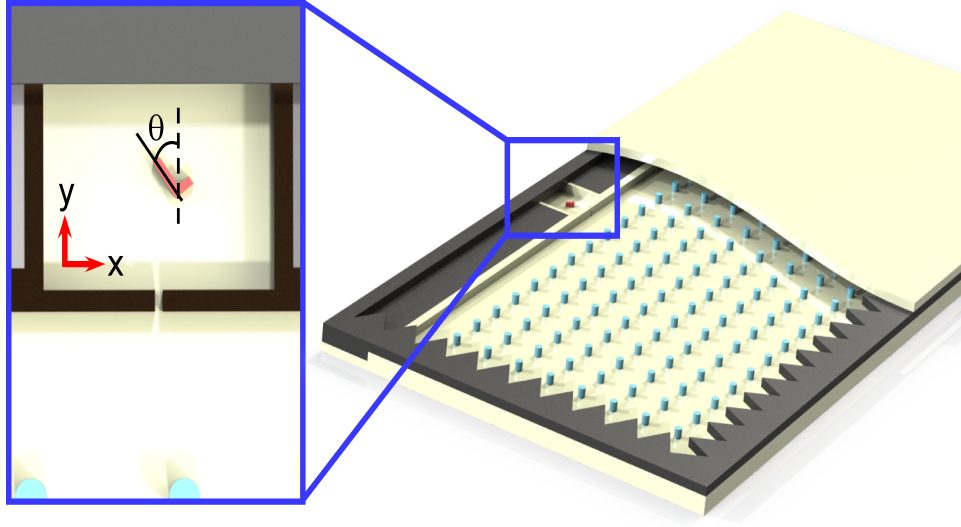


Figure 4.1: Trapping and orientating an L-shaped particle using resonator-enhanced conservative optical force in a single-port system. The single-port condition is realized by the single-mode one-way waveguide which is formed between the metal wall and the magnetized (+z) YIG photonic crystals (light blue). The light is coupled from the one-way waveguide to the square metal-box resonator (inset) through a small gap opened on the domain wall. The side length of the resonator is chosen to be $1.16a$ to ensure the resonant frequency always falls into the band gap of magneto-optical photonic crystal wherever L-shaped particle moves and orients. The rotation angle θ is defined as the angle between longer side of L-shaped particle and y-axis anticlockwise (inset).

at all the output ports, i.e. $\mathbf{F}(\mathbf{r}) = 1/\omega \cdot \sum_i [P_i(\mathbf{r})\nabla_{\mathbf{r}}\phi_i(\mathbf{r})]$, where ω is the angular frequency of the optical illumination, P_i and ϕ_i are the power and phase response of the scattered wave at the i^{th} port, respectively. Noting that the gradient of the phase response is curl-free, the curl of the optical force \mathbf{F} becomes $\nabla_{\mathbf{r}} \times \mathbf{F}(\mathbf{r}) = 1/\omega \cdot \sum_i [\nabla_{\mathbf{r}}P_i(\mathbf{r}) \times \nabla_{\mathbf{r}}\phi_i(\mathbf{r})]$. To establish a conservative optical force field in the hollow metal box (inset of Fig. 4.1), the sum of the cross products $\nabla_{\mathbf{r}}P_i(\mathbf{r}) \times \nabla_{\mathbf{r}}\phi_i(\mathbf{r})$ at all the output ports of the system has to add up to zero in the entire range of interest of the displacement \mathbf{r} . The output power and the gradient of phase response at each port of a tunable optical trapping system where the strength and direction of the optical forces constantly change with the particle displacement \mathbf{r} are non-zero according to RTOF. More specifically in a multi-port system, the output power at each port varies with the particle displacement, resulting in non-zero gradient of output power. It is practically impossible to maintain a zero sum of cross products $\nabla_{\mathbf{r}}P_i(\mathbf{r}) \times \nabla_{\mathbf{r}}\phi_i(\mathbf{r})$ in a tunable multi-port system, and even unrealizable to make the gradient of output power parallel to the gradient of phase response at every lumped port. One special case producing the conservative optical gradient force, regardless how complex a system would be, is a one-port system in which the zero gradient of constant output power equal to the input power P_{in} makes the curl of the optical force vanished and therefore the conservative optical force only arises from the gradient of phase response, i.e. $\mathbf{F}(\mathbf{r}) = (P_{in}/\omega)\nabla_{\mathbf{r}}\phi(\mathbf{r})$. In an effective optical trapping system where the restoring optical force is the negative gradient of the scalar potential U

($\mathbf{F} = -\nabla U$), the phase response is proportional to the shape of optical trap. Considering the schematic of an asymmetric dielectric particle inside a hollow metal box, the rotation of the particle will alternate the spatial distribution of dielectric constant and thus modify the phase response by modulating the effective optical length. Consequently, the variable optical trap orientates the particle along the direction which maximizes the phase delay at the output port.

For concreteness, to construct a conservative optical force field to simultaneously trap and orientate an L-shaped particle (inset of Fig. 4.1), we build a special one-port resonator-waveguide system, unlike most waveguides having reflection scattered back from the coupled optical resonator, immune to scattering from any structure disorder in the waveguide. The essential part of this one-port system is a single-mode one-way photonic crystal waveguide which prevents mode conversion and back-scattering propagation (Fig. 4.1). The photonic crystal is made of magneto yttrium-ion-garnet (YIG) pillars which under 1600 Gauss +z magnetic field at 4.28 GHz has relative permeability tensor as

$$\mu = \begin{bmatrix} 14 & 12.4i & 0 \\ -12.4i & 14 & 0 \\ 0 & 0 & i \end{bmatrix} \mu_o \quad (4.1)$$

The opposite off-diagonal elements in permeability arise because of gyrotropy of magneto material and result in non-zero Chern number by breaking the time-reversal symmetry. The number of chiral edge states (CESs) is equal to the sum of the Chern numbers of all the bulk bands under the band gap

of magneto-optical photonic crystal opened by the applied $+z$ magnetic field. Therefore, the unidirectional propagation of the optical mode along the edge of the magneto-optical photonic crystal is topologically protected and therefore immune to any disorder in the geometry. The radii of the YIG pillars are $0.0978a$ ($a = 40mm$ being the lattice constant). To confine the one-way waveguide to be operated in the single-mode regime, the width of the waveguide (inset of Fig.4.1, defined as the distance from the metal cladding to the edge of the nearest row of magneto-optical photonic crystal) is $0.65a$ which is narrow enough to support only one spatial mode. Since this one-way waveguide is robust to any scattering structural disorder, a square optical resonator (hollow metal box) can be coupled to the waveguide through a small slot on the metal cladding without introducing additional reflection port. The side length of the square resonator is $1.16a$ to make the resonant frequency of the fundamental cavity mode always fall into the band gap of the magneto-optical photonic crystal wherever the L-shaped particle locates or orients. When the one-way mode is excited and coupled with the optical resonator, the resonance-enhanced optical force traps the particle to the destination where the overlap between dielectric constant and optical intensity achieves its maximum. The L-shaped particle (relative permittivity $\epsilon_r = 6.25$) for demonstration possesses a length of $0.1a$ along its longer side and $0.0667a$ along its shorter side, both have identical width of $0.0333a$. The rotational angle θ of the particle (inset of Fig. 4.1) is defined as the angle between the longer side of the particle and $+y$ axis anticlockwise. The rotation of the asymmetric particle modifies

the overlap between dielectric constant distribution and optical intensity profile, which subsequently modulates the effective optical length between input and output ports and phase delay. The optical trap which is proportional to the spatial phase response distribution shifts its potential bottom accordingly. Therefore, particle orienting along different directions will be trapped to different locations, and conversely particle locating at different positions will be orientated along different directions by the conservative optical force.

4.2.2 Trapping the particle

To illustrate the effectiveness of trapping a particle within the optical resonator in this single-port system, we recorded the trajectories of particle motion of ten independent trials in which the particle is always trapped to the same position. In these ten trials, the particle is released at the grids of $x = (0.1a, 0.3a, 0.5a, 0.7a, 0.9a)$ and $y = (0.1a, 0.9a)$ as shown in Fig. 4.2a, and the rotational angle θ is kept at 0° . The optical force field is numerically computed from the Maxwell stress tensor using the finite-element method at the frequency of $0.5838c/a$. The trajectories (Fig. 4.2) of the particle motion are calculated in the particle tracing model where the color is proportional to the particle velocity. The black points in Fig. 4.2b d presents the positions of the particle moving along the trajectories at the times of $0.1ms$, $0.5ms$, and $3ms$. The dynamic viscosity is set to be $10^{-6}Pa \cdot s$, so that the particle slowly loses its kinetic energy and is stably trapped to the same location (Fig. 4.2d) after $3ms$ in all these ten trials.

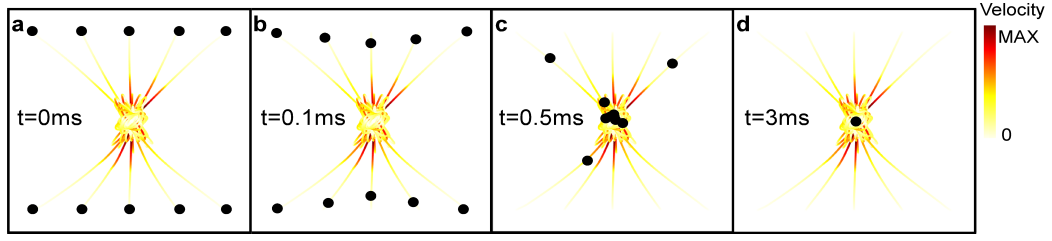


Figure 4.2: Trajectories of 10 trials of releasing L-shaped particle at 10 different initial locations at $x = (0.1a, 0.3a, 0.5a, 0.7a, 0.9a)$ and $y = (0.1a, 0.9a)$ (the orientation of particle is always kept at 0°). The L-shaped particle has a permittivity of 6.25, and a longer side of $0.0667a$ and a shorter side of $0.0333a$. Four snapshots of particle locations (black dots) at $t = 0ms$, $t = 0.1ms$, $t = 0.5ms$, and $t = 3ms$ are shown in (a) (d) (the dynamic viscosity is set to be $10^{-6} Pa \cdot s$). The color scale of the trajectories denotes the magnitude of particle velocities. In all trials, the particle is always stably trapped to the same position.

4.2.3 Orientating the particle

Since rotation of asymmetric particle will change the spatial distribution of dielectric constant, the bottom of optical force potential depends on the orientation of L-shaped particle, which provides us the capability of controlling another degree of freedom. To explore at what position and along what orientation the particle will be trapped, we reconstruct the optical force potentials based on the optical force fields numerically calculated in finite-element method using Helmholtz-Hodge decomposition for twelve rotational angles equally spaced between 0° and 330° (Fig. 4.3a). Beyonds trapping the particle to the maximum intensity point by the resonantor-enhanced optical force, the orientation of an asymmetric particle can be also precisely and stably controlled by the conservative optical force in such one-port system. The

trapping destinations of particle orientating along various directions are plotted in xy -plane as shown in Fig. 4.3b (green curve), and the projections of the optical force potential bottom on $x\theta$ - and $y\theta$ -planes are plotted in Fig. 4.3c and Fig. 4.3d, respectively. It is obvious that the optical force potential bottom is a strong function of particle orientation, and vice versa. The purely conservative gradient force in such one-port system, on one hand, traps the particle to the maximum intensity point without rotating it, and on the other hand, orientates the particle along a fixed direction if the particle is pinned at certain location. In this section, we provide an efficient and convincing method to simultaneously trap and orientate a non-centrosymmetric particle simply by tuning the frequency in a one-way single-port system. Such one-port system is realized by attaching an optical resonator to a topologically protected one-way waveguide which exhibits strong robustness to large impurities, and thus allows simultaneous operations on a chain of various optical cavities in which non-centrosymmetric particles can have their own location and orientation without cross-talking to each other. Stable trapping and orientating particles can be only realized in a conservative optical force field, which is strictly demonstrated by using RTOF whose results are validated by Lorentz force density as well as MST. Our novel way allows manipulating an additional degree of freedom to orientate the particles, which has never been realized, and will provide more effective controlling of live cells and virus in Biology.

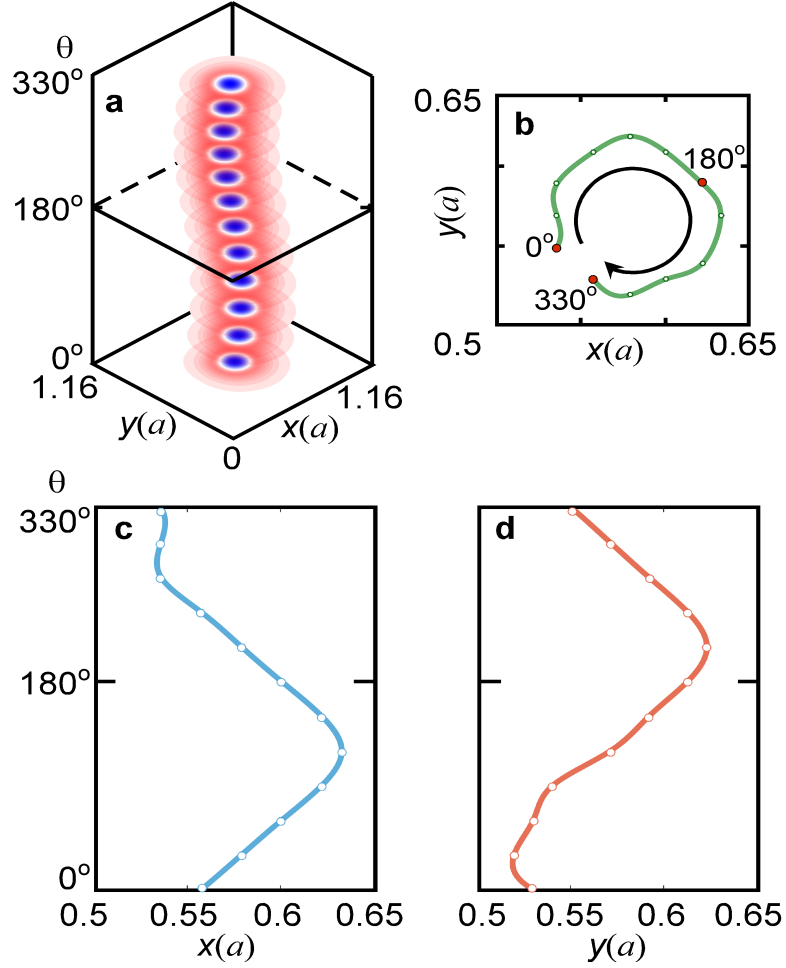


Figure 4.3: Variable optical potential bottom locations for different rotation angles at the frequency of $0.5838(c/a)$. (a) Color representation of twelve optical potentials at rotational angles equally spaced from 0° to 330° , which indicates that particle with different rotational angles will be ultimately trapped to different locations. (b) Projection of optical force potential minima on xy -plane for twelve rotational angles. The arrows denotes the rotational angle increases clockwise. (c) (d) projection of optical force potential minima on x - and y -planes, respectively.

4.2.4 Tuning the resolution of the optical trap

The landscape of the optical trap, which is proportional to the spatial phase response profile, can be deduced from the temporal coupled-mode theory (CMT) which reveals the frequency-dependence of phase response at the lumped port. The resonator-waveguide system shown in Fig. 4.1 has a fundamental cavity mode in the hollow metal box denoted by A and a single output port denoted by S_- propagating to the right end. Off the resonance when the cavity mode does not couple with the one-way mode, the system response is simply a phase delay, $S_- = e^{i\phi_0} S_+$. When the operating frequency is near the resonant frequency of the cavity mode A , the cavity mode is excited and the coupled-mode equations are

$$\begin{aligned} \frac{dA}{dt} &= -i\omega_0 A - \gamma_0 A + \sqrt{2\gamma_0} e^{i\theta_0} S_+ \\ S_- &= e^{i\phi_0} S_+ + \sqrt{2\gamma_0} e^{i\theta_0} A \end{aligned} \quad (4.2)$$

where ω_0 is the angular resonant frequency of cavity mode A , γ_0 is the decay rate, θ_0 is the phase shift when cavity mode is coupled with one-way mode. The complex-value transmission coefficient can be uniquely determined by CMT using energy conservation law and time reversal symmetry

$$T(\omega, \mathbf{r}) = \frac{S_-}{S_+} = \frac{-i[\omega - \omega_o(\mathbf{r})] - \gamma_o(\mathbf{r})}{-i[\omega - \omega_o(\mathbf{r})] + \gamma_o(\mathbf{r})} \quad (4.3)$$

The magnitude of the transmission coefficient is always unity, which is consistent with reflection-free phenomena observed in numerical simulations. The phase of the transmission coefficient, on the other hand, exhibits 2π phase transition across the resonance. The resonant frequency and decay rate are extrapolated by fitting the phase of transmission coefficient in Eq. 4.3 (CMT phase)

to the phase spectra from numerical simulations (numerical phase) using least-squared curve fitting. When the rotation angle $\theta = 0$, the fitting results are shown in Fig. 4.4 (a) for x-displacement of $0.55a$ and (b) for y-displacement of $0.53a$ where the CMT phase (surfaces) perfectly agrees with the numerical phases (light earth yellow curves). The advantage of Fig. 4.4(a), (b) is that it reveals the frequency-dependence of phase response as well as the optical trap potential shape. The black curves in Fig. 4.4(a) and (b) are cross sections by cutting through the phase spectra at the operating frequency of $0.5838c/a$. They correspond to two one-dimensional potential wells along x-displacement of $0.53a$ and y-displacement of $0.55a$, both with rounded and deep bottoms which trap the particle to the potential bottom rapidly and firmly as shown in the particle tracing results in Fig. 4.2. These two one-dimensional potential wells pass through the lowest point of the two-dimensional optical trap, shown as the dashed black lines on the proportional phase response in Fig. 4.4(d). If the operating frequency is lower than $0.5838c/a$, the optical trap potential becomes shallower, and if the operating frequency is higher than $0.5838c/a$, the optical trap bottom becomes flat and the particle cannot be held at the potential bottom tightly. An ideal optical trap can be formed at an operating frequency near the lower bound of displacement-dependent resonant frequency $\omega(r)$ (Fig. 4.4c) which can be derived by repeating the curve fitting procedure for the whole particle displacement range. The optical forces calculated from the gradient of displacement-dependent phase response (Fig. 4.4e, f, correspond to the line cross sections of Fig. 4.4d in the same color) in RTOF

scheme agree with the well-established MST calculation in ab-initio numerical simulations perfectly, which confirms our previous analysis on force conservativeness. Another point worthy to mention is that the optical force magnitude is proportional to the slope of the phase variation in space (for examples, black curves in Fig. 4.4a,b and phase landscape in Fig. 4.4d) which is determined by the linewidth of 2π phase transitions of light earth yellow curves in Fig. 4.4a and b. The linewidth of the resonance in phase spectrum is characterized by the decay rate γ_0 in CMT scheme, and therefore slower decay of cavity mode into the waveguide results in steeper slope of phase variation as well as larger stiffness of restoring optical force. Replacing the one-way waveguide by a general two-way waveguide will introduce a second port if the hollow metal box and L-shaped particle are kept unchanged, and the additional reflection port is coupled with the resonator and causes faster decay of cavity mode, leading to deterioration of optical force stiffness.

4.3 Vorticity residual in one-port and two-port system

Beyond the force conservativeness analysis based on RTOF scheme, the residual non-conservative component of the optical force fields can be numerically quantified by applying the discrete Helmholtz-Hodge (HH) decomposition to the simulated force fields directly. Any vector field $\mathbf{F}(\mathbf{r})$ vanishing at boundaries can be uniquely decomposed into three parts by HH decomposition, namely curl-free term, divergence-free term, and a harmonic term $\mathbf{F}(\mathbf{r}) = \mathbf{F}_c(\mathbf{r}) + \mathbf{F}_{nc}(\mathbf{r}) + \mathbf{h}(\mathbf{r}) = \nabla\Phi(\mathbf{r}) + \nabla \times \psi(\mathbf{r}) + \mathbf{h}(\mathbf{r})$ where the curl-

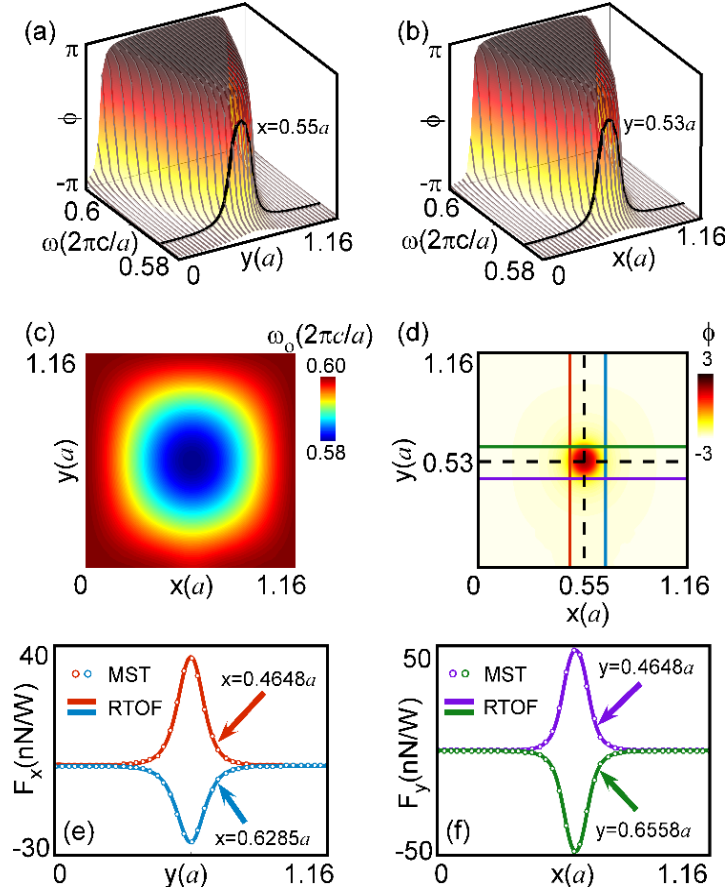


Figure 4.4: Frequency-dependence of the conservative optical force field. (a) Perfect agreement of negative phase response calculated through finite-element method (earth yellow curves) and single-mode temporal coupled-mode theory (curved surface) in the frequency range of $(0.58c/a, 0.6c/a)$ and y -displacement range of $(0, 1.16a)$. The x -displacement is $0.4648a$, and the corresponding negative phase response at the frequency of $0.5838c/a$ is highlighted by the red curve. (b) The negative phase response as a function of particle position over the whole square metal-box resonator at the frequency of $0.5838c/a$. The red and blue lines indicate the vertical movements of particle moving along $x = 0.4648a$ and $x = 0.6285a$, and purple and green lines indicate the horizontal movements of particle along $y = 0.4648a$ and $y = 0.6558a$. (c) (d) Perfect agreement of optical forces calculated through RTOF (solid curves) and MST (dots) as the particle moves along the paths plotted in the same color indicated in (b). In RTOF calculation, the phase response in (b) is used to derive the phase gradient.

free conservative force $\mathbf{F}_c(\mathbf{r})$ is the gradient of a scalar potential $\Phi(\mathbf{r})$, the divergence-free non-conservative force $\mathbf{F}_{nc}(\mathbf{r})$ is the curl of a scalar stream $\Psi(\mathbf{r})$ varying along z -direction, and $\mathbf{h}(\mathbf{r})$ is the harmonic term. To do the comparison, we construct a two-port system by replacing the magneto-optical waveguide by a regular two-way single-mode waveguide. The same L-shaped particle with rotational angle $\theta = 0^\circ$ is placed in the identical hollow metal boxes of both systems, and moving on the discretized square grid whose resolution is defined as the number of mesh points along the side. The optical force fields are evaluated by integrating MST surrounding the particle at the frequency of $0.5838c/a$. The optical force does not vanish when the particle is near the slot on the metal interface between the cavity and the waveguide because the optical power is flowing through the slot and exerts force on the particle. This non-vanishing optical force near the boundary introduces a non-conservative force in HH decomposition even in one-port system. However, the non-conservative force induced by the discretization of optical force field should be reduced by finer resolution. We apply Greens function method to the measured optical force fields from which the scalar potential is the spatial convolution between gradient of the Greens function and the simulated optical force and the scalar stream is the spatial convolution between the curl of the Greens function and the simulated optical force. A scaling factor δ is introduced to the Greens function $G(\Delta\mathbf{r}) = -\mathbf{1}/2\pi \cdot \ln(|\Delta\mathbf{r}| + \delta)$ to avoid the singularity at the particle location ($\delta r = 0$). The scaling factor δ is chosen to minimize the normalized Frobenius norm of curl-free component during every

HH decomposition. The decomposed scalar potential and scalar stream of the optical force field in one-port system and two-port system are shown in Fig. 4.5a,b. Since the radius of scalar potential at half depth in one-port system is much smaller than that in two-port system, the stiffness of conservative restoring optical force in one-port system is much larger than that in two-port system, which provides stronger trapping capability when one-way waveguide is used. As mentioned before, the stiffness of the optical trapping force is reduced in the two-port system because the cavity mode is coupled with two counter-propagating waveguide modes and decays faster than the one-port system. The additional reflection port also produces non-conservative optical force driving the L-shaped particle into rotational motion. Comparing the scalar streams plotted in the same color scale as the corresponding scalar potentials in Fig. 4.5a and Fig. 4.5b, the one-port system shows flat Ψ but the two-port system has larger portion of gurgitation in the scalar stream. This discrepancy can be better visualized by plotting the vorticity ratio with respect to the optical force field resolution as shown in Fig. 4.5c, where the vorticity ratio is defined as the normalized Frobenius norm of $\mathbf{F}_{nc}(\mathbf{r})$ over the whole displacement range of the particle.

4.4 Conclusion remarks

In this chapter, I present a way to simultaneously trap and orientate a nano-particle in non-touch manipulation. Even though people have realized to use the single-beam gradient force trap to anchor a nano-particle in biomedical

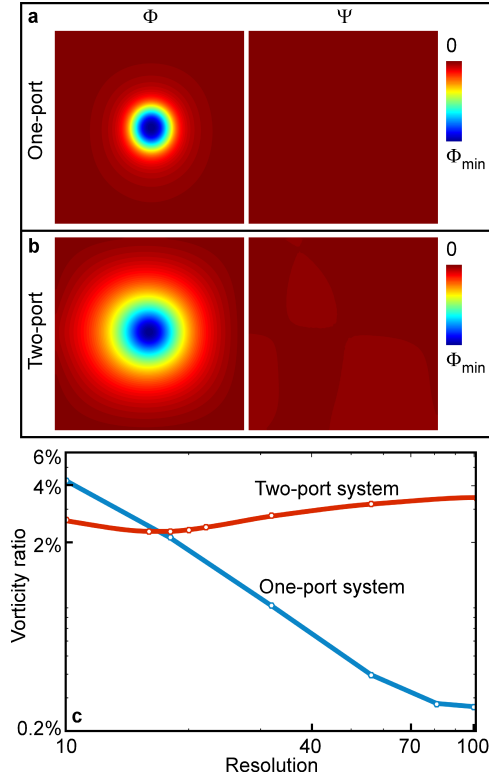


Figure 4.5: Discrete Helmholtz-Hodge decompositions (HHD) for single-port system and two-port system. (a) Reconstructed curl-free potential and divergence-free potential from HHD in single-port system. The rotational angle of L-shaped particle is 0° and the frequency is $0.5838c/a$. (b) reconstructed curl-free potential and divergence-free potential from HHD in two-port system. The two-port system is constructed by replacing the one-way single-mode waveguide by a regular two-way single-mode waveguide. To do the comparison with one-port system, the L-shaped particle has the same rotational angle and the system is operated at the same frequency as well. Compared with one-port case, the curl-free potential has worse confinement, and the divergence-free potential is obviously larger than that in one-port system. (c) Vorticity ratio calculated through normalized Frobenius norm after HHD for one-port system and two-port system. In one-port system, the vorticity ration decreases linearly with the increasing resolution in log-log scale until reaches the error limit (the error comes from the non-zero optical forces on L-shaped particle even when it touches the resonator walls). In two-port system, on the other hand, the vorticity ration hardly drops with increasing resolution.

application, the optical tweezer cannot precisely control the orientation of the nano-particle because of non-conservative scattering force is inevitable in such a system. Therefore, a method of stably orientating a nano-particle is highly desirable in a broad range of applications in biomedical engineering, such as molecularly targeted therapy and direction growth of nerve. Topological one-way waveguide also has other applications. For example, the location of the periodic optical force potential bottom in single-mode one-way waveguide is a function of the permittivity of the photonic crystal rods, which provides a promising way to realize the optical pulling force. However, the material loss which is ubiquitous in magneto-optical photonic crystal will break the optical force conservativeness. A simple remedial way of compensating the material loss and thus recovering the optical force conservativeness will be presented in the next chapter.

Chapter 5

Compensating material loss in topological one-way waveguide

5.1 Introduction

In Chapter 4, we have demonstrated a unidirectional waveguide-resonator system to simultaneously trap and orientate an asymmetric L-particle. Besides constructing conservative optical force field, topological one-way waveguides are also widely used in optical pulling force, optical sensing, and quantum computing/simulations. However, various loss including dispersion loss, scattering loss, and absorption loss will deteriorate the performance of the one-way waveguide system. For example, in temporal coupled-mode theory, the loss is generally treated as an additional port and therefore breaks the single-port requirement for constructing conservative optical force field. Not only does the loss attenuates the optical intensity as light is propagating along the waveguide, which may decrease the optical force strength, but also the loss can introduce rotational component of optical force and thus results in unstable optical trapping. Furthermore, the material loss may harm the immunity of the one-way waveguide to back scattering of guided waves. To make the performance of one-way waveguide system in various applications robust to loss, an applicable method of compensating the loss in such a system is highly

desirable which will be addressed in this chapter.

5.2 Compensating the material lossy using active medium

The simplest way to compensate the material loss of the topological photonic crystal is to add shells made of gain medium surrounding the original magneto-optical photonic crystal rods. The structure is shown in Fig. 5.1 which is exactly the same as that in Fig. 4.1, except now the inner magneto photonic crystal rods (light blue) are assumed to be lossy with permittivity of $14.63 - 0.5i$ and active shells (dark orange) with thickness of $0.0196a$ and permittivity of $1 + \varepsilon''_{shell}$ are coated outside the rods, where a is the lattice constant and ε''_{shell} is the imaginary of the permittivity of the active shells. The permeability matrix of the lossy magneto-optical photonic crystal is still

$$\vec{\mu} = \begin{bmatrix} 14 & 12.4i & 0 \\ -12.4i & 14 & 0 \\ 0 & 0 & i \end{bmatrix} \mu_o \quad (5.1)$$

to ensure the unidirectional light propagation to right. Without the active shells, one can immediately find the decay of electromagnetic field along the propagation direction in the one-way waveguide as shown in Fig. 5.2. Note that the power can only be absorbed when the light is transmitting at the surfaces of the lossy magneto-optical rods. Therefore, the more the optical power is trapped by the square optical resonator, the less the optical power is absorbed by the lossy magneto-optical rods. The amount of trapped optical power in the resonator depends on the displacements and orientation of the L-particle because the resonant frequency depends on the movements of the

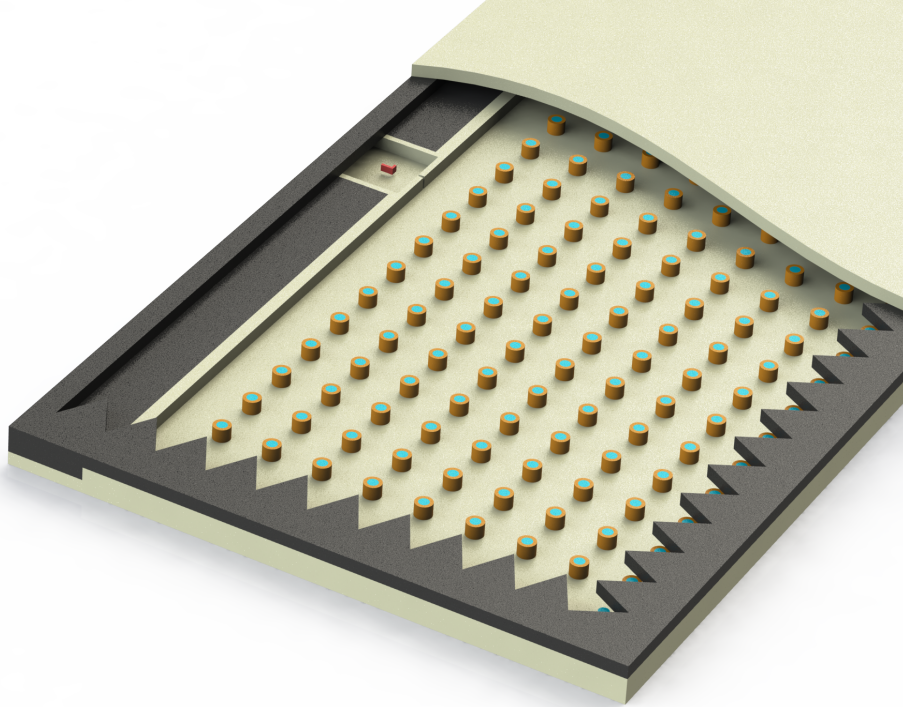


Figure 5.1: Lossy topological photonic crystal (blue rods) with shells made of gain medium (orange shells). The lattice constant a is 0.04, the radii of lossy blue rods are $0.0978a$, and the thickness of the orange shells is $0.0196a$. The complex permittivity of the topological photonic crystal is set to be $14.63 - 0.5i$, and the complex permittivity of the active shells is $1 + \varepsilon''_{shell}$ where the suitable value of ε''_{shell} will be studied. The L-particle in the optical resonator is shown as well, which is kept identical to the that in Fig. 4.1.

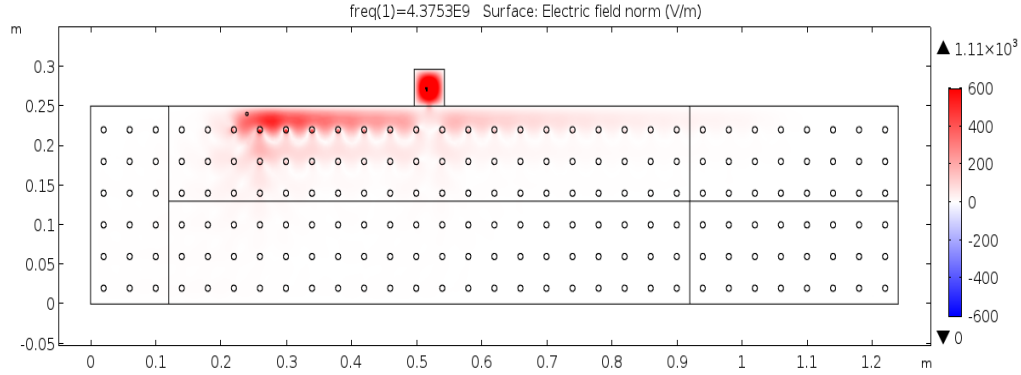


Figure 5.2: Decay of the optical power along propagation direction when the magneto-optical photonic crystal is lossy. The structure is exactly the same as the structure in Fig. 4.1 except the permittivity now is $14.63 - 0.5i$. Since the resonant frequency of the square optical resonator depends on the location and orientation of the L-particle, the amount of optical power trapped by the optical resonator is varied by the L-particle. This will result in a fluctuation in the output power on the right and thus break the optical force conservativeness as the gradient of the output optical power is not zero, according to the conclusion of force conservativeness based on RTOF in Ch.3.

L-particle. As the result, the output power emitted to the right is not constant any more, but changing with the movement of the L-particle. Since the spatial gradient of a varying output power with respect to L-particle displacements becomes non-zero, the conservativeness of the optical force is broken.

To compensate the loss of the optical power while it is propagating along the waveguide, I add the active shells made of gain medium surrounding the lossy magneto-optical rods. To check the effectiveness of the active shells, one can examine whether the optical power, at the operating frequency, becomes constant again across the whole waveguide by carefully tuning the permittivity

of the active shells. However, this approach requires the complete structure to simulate and the examination of constant optical power at each distance along the waveguide for every frequency is hard to perform manually. Therefore, this method is very time-consuming and computationally expensive. Alternatively, I developed the weak-form formulation to find the complex wave vector, whose imaginary part corresponds to the exponential decay of the optical power, for frequencies within the band gap using only one single period (one unit cell length along horizontal direction) of the magneto-optical photonic crystal.

5.2.1 Weak-form formula for topological waveguide

Developing the weak-form formula for topological waveguide used in partial differential equation (PDE) model serves as the basis of numerical modeling, from which the complex wave vector can be derived for certain operating frequency. The imaginary part of the complex wave vector describes the exponential power loss of the one-way waveguide, which is going to be eliminated by choosing proper active shell properties.

To confirm the correctness of the weak-form expression of the wave equation in lossy topological waveguide with the active shells surrounding the magneto-optical rods, the simulation results of the weak-form simulation are corroborated by those using internal COMSOL eigensolver as shown in Fig.5.3. The detailed derivation of weak-form formula is done based on [17], and further consideration of anisotropy of permeability and permittivity in topological photonic crystal is included as shown in Appendix D. Here I used the weak-

form formula for H-field as the permeability is not isotropic (RHS is to be put in COMSOL)

$$\begin{aligned}
& \mathbf{v} \cdot \left\{ \begin{array}{l} -\frac{\mathbf{k}}{\epsilon} \times (\mathbf{k} \times \mathbf{u}) - i\mathbf{k} \times \left(\frac{1}{\epsilon}\nabla \times \mathbf{u}\right) - i\nabla \times \left(\frac{1}{\epsilon}\mathbf{k} \times \mathbf{u}\right) \\ +\nabla \times \left[\frac{1}{\epsilon}(\nabla \times \mathbf{u})\right] - \mu\frac{\omega^2}{c^2}\mathbf{u} \end{array} \right\} \\
& = -(\mathbf{k} \times \mathbf{v}) \cdot \frac{1}{\epsilon}(\mathbf{k} \times \mathbf{u}) - i(\mathbf{k} \times \mathbf{v}) \cdot \left(\frac{1}{\epsilon}\nabla \times \mathbf{u}\right) - \\
& \quad i(\nabla \times \mathbf{v}) \cdot \left(\frac{1}{\epsilon}\mathbf{k} \times \mathbf{u}\right) + (\nabla \times \mathbf{v}) \cdot \left(\frac{1}{\epsilon}\nabla \times \mathbf{u}\right) - \frac{\omega^2}{c^2}\mathbf{v} \cdot \overset{\leftrightarrow}{\mu}\mathbf{u}
\end{aligned} \tag{5.2}$$

where \mathbf{v} is the test function, \mathbf{k} is the wave vector (the eigenvalue to be solved), ω is the angular frequency in the input, ϵ is the complex permittivity, $\overset{\leftrightarrow}{\mu}$ is the anisotropic permeability, and \mathbf{u} is the electric field, which serves as the dependent variable in the weak-form simulation.

5.2.2 Complex dispersion relation of lossy one-way waveguide with loss compensation

The effectiveness of compensating the material loss of topological waveguide can be examined by the imaginary part the complex wave vector derived from the weak-form simulations for every operating frequency. To reduce the amount of simulations, the frequency range of one-way waveguide mode is first determined by the eigensolver simulating the lossless topological photonic waveguide shown as the red dashed curve in Fig.5.4(a),(b), and (c), (the light grey bands are either bulk bands or left-propagating modes at the bottom, and we do not consider here). Then for each frequency on the red dashed curve, the complex wave vector, whose real part is shown in blue in Fig.5.4 and imaginary part is shown in green in Fig.5.4, can be calculated from the weak-form simulations.

Tuning the permittivity of active shell while keeping its thickness con-

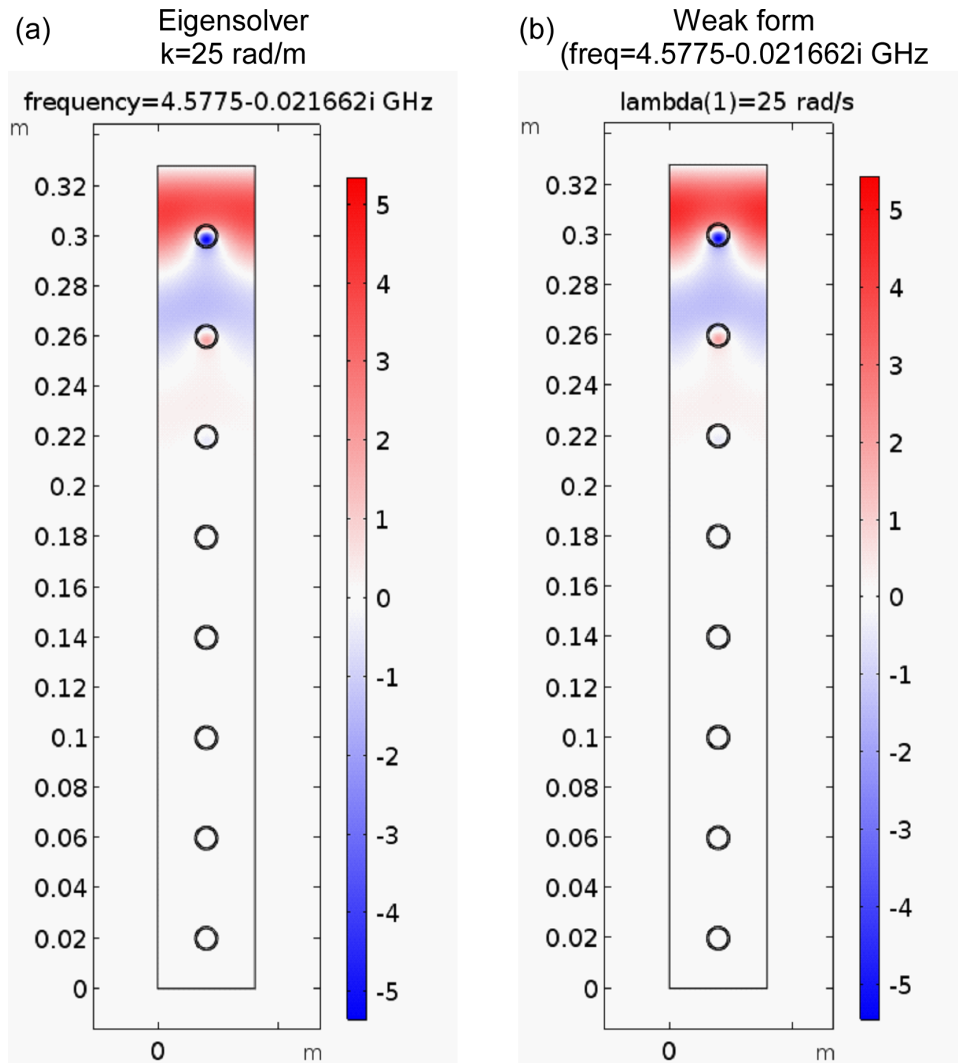


Figure 5.3: Correctness of weak-form simulation of lossy topological waveguide with active shell verified by COMSOL native eigensolver. (a) the z -component (out-of-plane component) of electric field, E_z , calculated by eigensolver at the floquet $k = 25\text{rad}/m$, and the eigenfrequency is calculated as $f = 4.5775 - 0.021662i\text{GHz}$. (b) E_z profile calculated from weak-form simulation for $f = 4.5775 - 0.021662i\text{GHz}$, and the result of floquet wave vector is $25\text{rad}/m$. The identical field profile also verifies the correctness of the weak-form simulation.

stant can compensate the absorbed optical power of the lossy magneto-optical waveguide. In Fig.5.4(a), the imaginary part of the complex wave vector is negative when the active shells are not turned on, i.e. active shell has no positive imaginary part. At this time, the optical power will decay at the ratio of $e^{-2k''_x}$ along the waveguide (x-direction). The imaginary part of k_x can be reduced by increasing the imaginary part of the shell permittivity to 2.2105 as shown in Fig.5.4(b) where k''_x is near to the zero for a wide frequency range. However, further increasing the imaginary part of the shell permittivity will make the imaginary part of k_x to be positive which indicates the extra power is gained at the output port. Like the power loss, the power gain is also a function of the movement and orientation of the L-particle in the optical resonator, and thus breaks the optical force conservativeness. Therefore, we have to carefully tune the shell permittivity to compensate the material loss so that the conservativeness of the optical force can be recovered.

5.3 Recovering force conservativeness using active media

The strategy to recover the optical force conservativeness using active shells includes two steps. First, we want to examine whether the optical power becomes constant again along the optical waveguide. Second, we want to know the most proper value of imaginary part of shell permittivity for a given operating frequency. To corroborate the recovery of the force conservativeness, the vorticity ratio of the optical force at the same operating frequency is compared for different values of imaginary part of the shell permittivity.

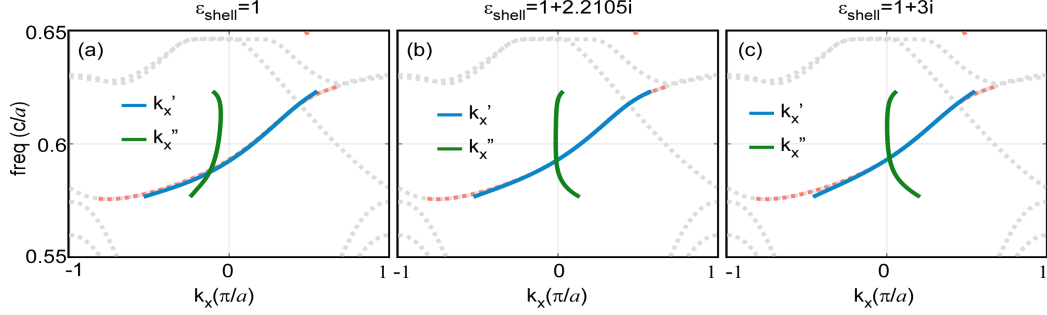


Figure 5.4: Dependence of the real part of complex wave vector k'_x and the imaginary part of complex wave vector k''_x on the permittivity of the active shell. The light grey bands are either bulk bands or left-propagating modes at the bottom of the structure calculated from the COMSOL eigensolver. The red dashed bands are the one-way waveguide modes calculated for the lossless topological photonic crystal waveguide. (a) complex wave vector computed by weak-form simulation within the frequency range of one-way waveguide mode when shell permittivity has no gain, i.e. $\epsilon_{shell} = 1$. k'_x is the real part of the wave vector shown in blue and k''_x is the imaginary part of the wave vector shown in green. (b) the complex wave vector computed from weak-form simulation for $\epsilon_{shell} = 1 + 2.2105i$. In this case, the imaginary part of k_x is reduced to zero for a wide range of frequency. (c) the complex wave vector computed from weak-form simulation for $\epsilon_{shell} = 1 + 3i$ at which the imaginary part of k_x becomes positive. The conservativeness of the optical force is broken as well in this case because the power gained at the output port also depends on the movement and orientation of L-particle in the optical resonator.

5.3.1 Choosing active medium for the operating frequency

Since the imaginary part of wave vector k_x'' is frequency dependent as shown in Fig.5.4, each operating frequency has the best suitable active shell permittivity to reduce k_x'' to 0. This $freq - \epsilon_{shell}''$ relationship can be found whenever $k_x'' = 0$.

To find the $freq - \epsilon_{shell}''$ relationship when $k_x'' = 0$, the first step is to find the dispersion relation with respect to k_x'' (Fig. 5.4 presents 3 examples) by sweeping the imaginary part of shell permittivity ϵ_{shell}'' from 0 to 3, shown in Fig. 5.5(a). The cross-section between the curved surface as the dispersion relation and the cutting plane when $k_x'' = 0$ is the $freq - \epsilon_{shell}''$ relationship we want to find as shown in Fig. 5.5(b). Even though at the frequency of $0.6(c/a)$ the square optical resonator can trap more optical power, the optical force potential bottom is flat, which is not suitable for trapping the L-particle for a high resolution. Therefore, the operating frequency of $0.583(c/a)$ is chosen, and the most suitable value of ϵ_{shell}'' which reduces k_x'' to zero can be read as 2.25.

Whether the optical power along the waveguide becomes constant again can be checked by running the whole-structure simulation in a linear solver. The norm of E-field along the waveguide for the permittivities of active shell equal to $1 + 1.2i$ and $1 + 2.25i$ at the frequency of $0.583(c/a)$ is shown in Fig. 5.6(a) and Fig. 5.6(b), respectively. Unlike the smaller imaginary part of shell permittivity in which case the optical power still decays along the waveguide, the value of shell permittivity equal to $1 + 2.25i$ makes the opti-

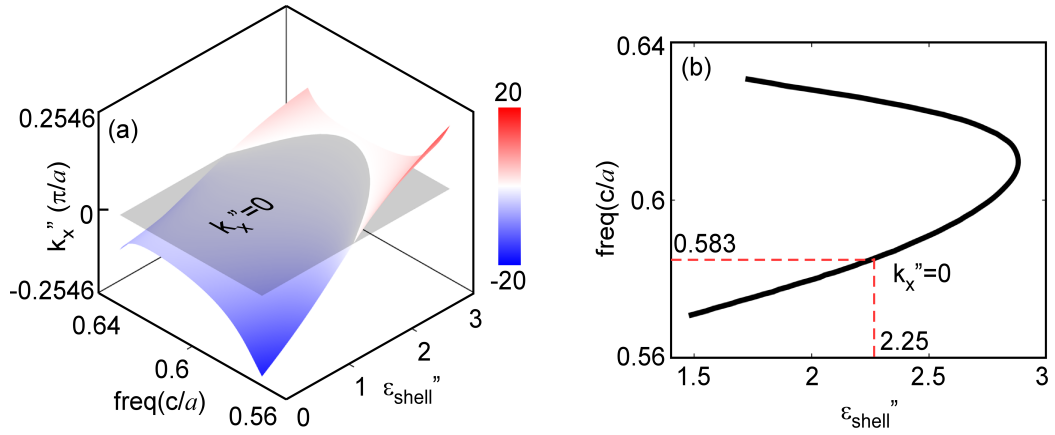


Figure 5.5: $freq - \epsilon_{shell}''$ relationship when $k_x'' = 0$. (a) the curved surface is the dispersion relation of frequency with respect to the imaginary part of floquet wave vector k_x'' within the range of ϵ_{shell}'' from 0 to 3. The cutting plane at $k_x'' = 0$ is shown in semi-transparent light gray. (b) the cross section between the plane and curved surface in (a), which is the $freq - \epsilon_{shell}''$ relationship we want to derive. At the frequency of $0.583(c/a)$ when the bottom of the optical potential in the square resonator is a tip rather than flat corresponds to the most proper imaginary part of shell permittivity equal to 2.25.

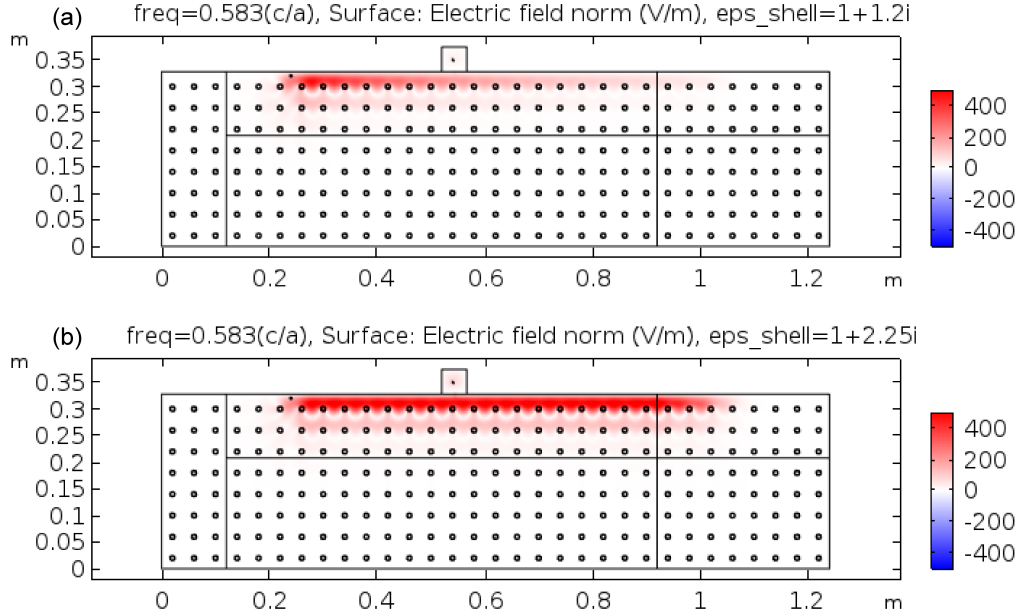


Figure 5.6: Norm of E-field along the waveguide. (a) the permittivity of the active shells is $1 + 1.2i$ and the operating frequency is $0.583(c/a)$. The optical power decays along the waveguide because of small imaginary part of the shell permittivity. (b) the permittivity of the active shells is $1 + 2.25i$ and the operating frequency is still $0.583(c/a)$. The optical power keeps constant along the optical waveguide.

cal power becomes constant again along the waveguide. I will then use this value to construct the whole structure in linear solver to examine whether the conservativeness of the optical force is recovered.

5.3.2 Reduction of vorticity ratio with appropriate active medium

The recovery of optical force conservativeness can be quantitatively described by vorticity ratio which is defined as the ratio of Frobenius norm of

rotational force and Frobenius norm of total force as

$$E = \|u_{\perp}\|_F / \|u\|_F \quad (5.3)$$

where the Frobenius norm of a 2D discrete vector field is defined as

$$\|u\|_F = \sqrt{\sum_{i=1}^m \sum_{j=1}^n (u_{x,ij}^2 + u_{y,ij}^2)} \quad (5.4)$$

The irrotational and rotation components of the total force can be decomposed by using Helmholtz-Hodge decomposition as explained in Ch. 3. The total optical force exerted on the L-particle is calculated by using Maxwell stress tensor integration for every displacement of L-particle from 0 to $1.16a$ along both x-direction and y-direction, at the frequency of $0.583(c/a)$ when the permittivity of the active shells is $1 + 1.2i$ and $1 + 2.25i$, respectively.

The results of Helmholtz-Hodge decomposition are shown in Fig. 5.7. By comparing Fig. 5.7(a) with Fig. 5.7 (c), the depth of the irrotational potential when $\epsilon''_{shell} = 1.2$ is only about half of that when $\epsilon''_{shell} = 2.25$. Since the rotational potential when $\epsilon''_{shell} = 1.2$ is just a little deeper than that when $\epsilon''_{shell} = 2.25$ as shown in Fig. 5.7(b) and Fig. 5.7(d), the vorticity ratio when $\epsilon''_{shell} = 2.25$ is expected to be about half of that when $\epsilon''_{shell} = 1.2$. This conclusion is further corroborated by the values of vorticity ratio for different ϵ''_{shell} as shown in Fig. 5.8. When ϵ''_{shell} is smaller than 1.7, most optical power is absorbed before it reaches the optical resonator, and therefore the modulation effect of L-particle movements on the output power is weak. As a result, the vorticity ratio reduces slowly with increasing ϵ''_{shell} . After $\epsilon''_{shell} = 1.7$, the

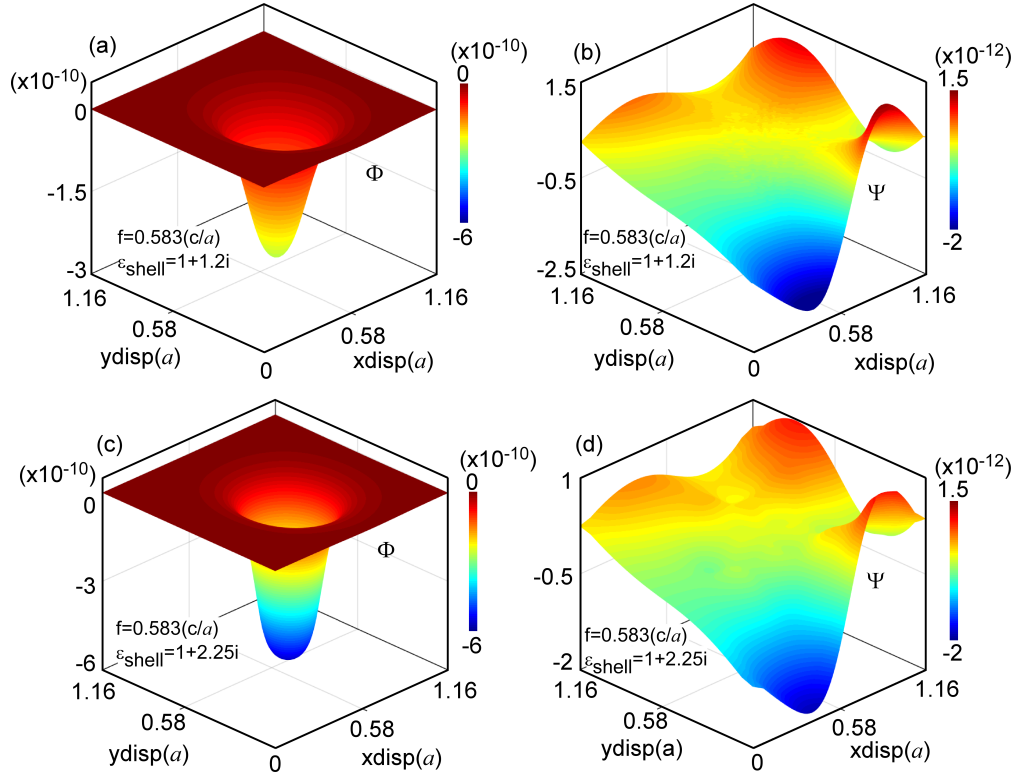


Figure 5.7: Irrotational potential and rotation potential derived by using Helmholtz-Hodge decomposition. (a) and (b) are irrotational potential Φ and rotational potential Ψ for the case when the active shell permittivity is $1 + 1.2i$ at the frequency of $0.583(c/a)$. (c) and (d) are irrotational potential Φ and rotational potential Ψ for the case when the active shell permittivity is $1 + 2.25i$ at the frequency of $0.583(c/a)$. The irrotational potential when $\epsilon''_{shell} = 2.25$ is one time deeper than that when $\epsilon''_{shell} = 1.2$ by comparing (c) with (a), while the rotational potential when $\epsilon''_{shell} = 2.25$ is a bit shallower than that when $\epsilon''_{shell} = 1.2$. Therefore, the vorticity ratio when $\epsilon''_{shell} = 2.25$ is expected to be about half of that when $\epsilon''_{shell} = 1.2$.

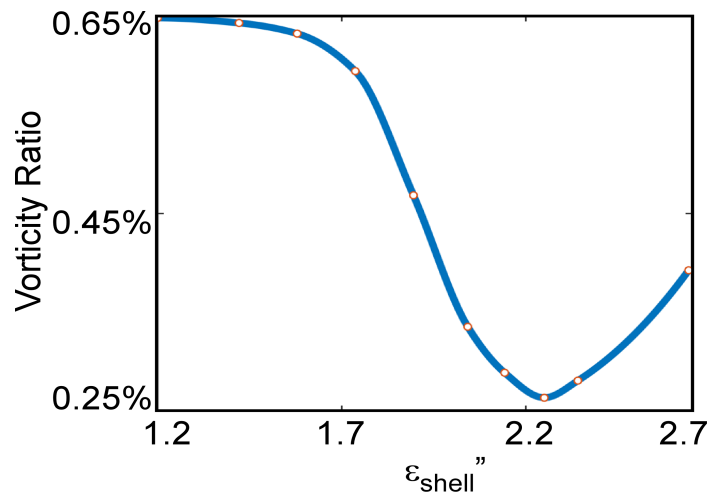


Figure 5.8: Vorticity ratio for different values of ϵ''_{shell} . When $\epsilon''_{shell} < 1.7$, most optical power is absorbed before reaching the square optical resonator and therefore the vorticity ratio changes slowly with ϵ''_{shell} . The vorticity ratio is minimized when ϵ''_{shell} is around 2.25, and then increases as the gained power at the output port breaks the force conservativeness again.

vorticity ratio rapidly drops down and reaches its minimum around ϵ''_{shell} at 2.25. As ϵ''_{shell} continues increasing, the gained power which changes with L-particle's movements will break the force conservativeness again and increase the vorticity ratio.

5.4 Conclusion remarks

In this chapter, I provided a straightforward way to compensate the material loss of topological one-way waveguide by coating the lossy ferrite rods with shells made of gain medium. The purpose is to maintain the conservativeness of the optical force in real world when material loss presents. As seen in Fig. 5.8, the conservativeness of the optical force can be recovered by the active shell coating and provides a promising future of optical trapping using one-way waveguide. The other interesting fact I found but now showed here is that, the material loss (ϵ_{rods} has imaginary part) does not break the time-reversal symmetry but only attenuates the optical power of propagating wave.

Chapter 6

Self-aligned topological photonic crystals

6.1 Introduction

Self-aligned or self-assembled structures with tunable compositions and structures have attracted wide attention of researchers in the past several decades because the well-defined superstructures present special physical, chemical, and mechanical characteristics. For example, the photonic crystals with perfect aligned structure exhibit photonic band gap preventing the light propagating through the bulk, which is essential in realizing topological one-way edge mode. Since 1950s, various self-assembly methods have been proposed for monodisperse polymer microspheres based on a broad range of phenomena including electrostatic interaction[45, 91, 93], charge compensation effect[33], bonding interaction[36], hydrophilic/hydrophobic effect[39], and capillary force. However, all the proposed methods are based on self-assembly where the particles are either touch with each other (or near to each other enough) or surrounded with fluid, which limits the tunable range of the superstructure. In this chapter I show the rods of topological photonic crystal can be self-aligned using conservative optical force generated by external input optical power. Since the optical force is not generated from the interaction between the neighboring rods of the topological photonic crystal, this method provides much

large freedom on the lattice constant of the photonic crystal and therefore is suitable for wider range of applications.

6.2 Mode profiles in topological photonic crystal with honeycomb lattice

Unlike the magneto photonic crystal presented in Chapter 4 with square lattice where the most optical intensity is outside the rods, in this chapter I use the honeycomb lattice in order to search for modes which trap majority of optical power inside the rods for both chiral edge modes and bulk mode, based on the principle that the rods are trapped to the highest optical intensity region. To construct single-port system where conservative optical force field can be created, we still need to break the time-reversal symmetry to realize one-way waveguide. To this end, gyromagnetic anisotropy is employed because the ferrite rods for the TM polarization is commercially available [3]. Under the DC magnetic field of $1884G$ along the axis of rods (z -axis in Fig. 6.1), the ferrite has the magnetic permeability tensor as

$$\mu = \begin{bmatrix} 0.78484 & -0.74363i & 0 \\ 0.74363i & 0.78484 & 0 \\ 0 & 0 & 1 \end{bmatrix} \mu_o \quad (6.1)$$

The topological photonic crystal structure under study shown in Fig.6.1 has a lattice constant of a ($a = 0.01m$ in the FEM simulation), and the radius of photonic crystal rod is set to be $0.23a$. Even though the chiral edge mode propagates within the boundary ferrite rods, the metal wall is still necessary to tune the highest optical power position along y -direction as well as to construct

the “perfect” bulk mode to finalize the alignment of all the ferrite rods.

6.2.1 K-group rods and K'-group rods in row-by-row fabrication procedures

Similar to most self-assembly methods, it is convenient to align the magneto-optical photonic crystal by adding a new row of rods to the existing bulk photonic crystal which is already perfectly aligned. The reflection-free single-mode chiral edge mode ensures the conservativeness of optical force, which is promising to automatically align the newly added row of rods. In honeycomb lattice, the rods can be categorized into two groups, K-group (white rods in Fig.6.1) and K'-group (gray rods in Fig. 6.1). Therefore, the optical force exerted on these two groups of rods through chiral edge states are investigated separately.

6.2.2 Edge-mode profiles of boundary rods of K-group and K'-group

The first step of this study is to derive the band diagrams for two categories of structures with boundary rods of K-group and K'-group by sweeping the floquet wave vector along x-direction in an eigensolver using the finite-element method. From the band diagrams, we can immediately determine the operating frequency range and floquet k_x range as shown in the left panels of Fig. 6.2 and Fig. 6.3. The band gap of magneto-optical photonic crystal opens the operating frequency range within which we can excite the chiral edge modes as shown in the right panels of Fig. 6.2 and Fig. 6.3. The corre-

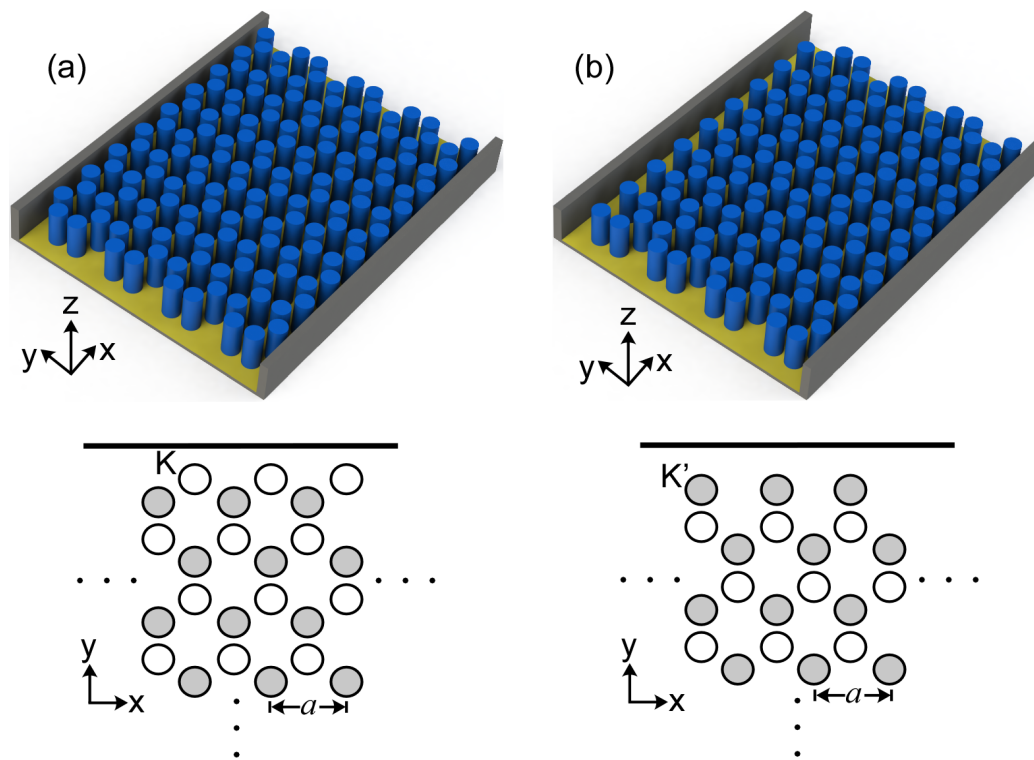


Figure 6.1: Categorization of ferrite rods in honeycomb lattice. The categorization is determined by the nearest row of rods to the further metal wall along $+y$ -direction. (a) ferrite rods of group K (shown as white rods) are adjacent to the metal wall further along $+y$ -direction; (b) ferrite rods of group K' (shown as gray rods) are adjacent to the metal wall further along $+y$ -direction. The definition of lattice constant a is also labeled in the corresponding top-view illustrations in the bottom of corresponding devices.

sponding operating frequency and floquet kx are labeled by red dashed lines on the left half of the same figures. Since the group velocity of chiral edge mode is proportional to the slop of band diagram, we are only looking at the top right-propagating modes whose bands are non-decreasing with respect to floquet wave vector. By examining the highest optical intensity region of these mode profiles, we can make initial inference whether the rods can be aligned by the optical force. As we can see from the mode profiles, the highest optical intensity regions are superpositioned with the target locations of the top-row (or boundary) ferrite rods in a perfectly aligned photonic crystal along x-direction, and thus the chiral edge states are promising to align the boundary ferrite rods along x-direction.

6.2.3 Self-assembled bulk-mode profile

As we shall discuss later, though the chiral edge states are capable of aligning the boundary ferrite rods along x-direction by nature, the alignment along y-direction is hard to realized by merely using the chiral edge states. Therefore, we need to find the “perfect” bulk mode which has all the highest optical intensity regions coincident with the well-defined photonic crystal. Fortunately, this ”perfect” bulk mode does exist in the higher order mode as shown in Fig. 6.4. One thing worthy to be mentioned is that this kind of bulk mode only appears around floquet $kx = 2n\pi/a, n = 1, 2, 3, \dots$

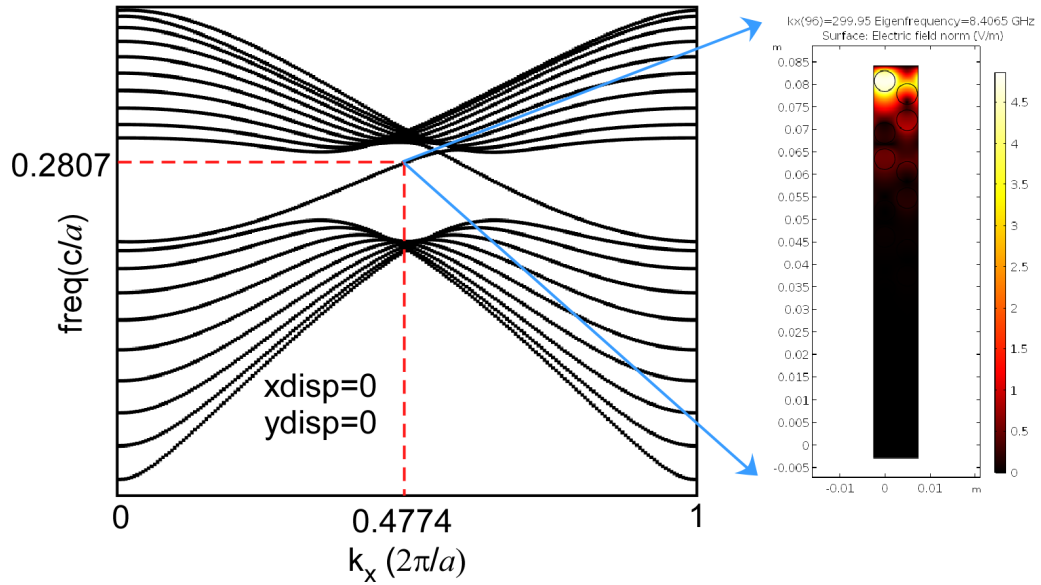


Figure 6.2: Band diagram and mode profile of chiral edge state when K-group rods are the nearest to the top metal wall. Left: band diagram when the x-displacements of boundary rods and y-displacements of boundary rods are both 0. The normalized electric field intensity distribution corresponding to frequency of $0.2807(c/a)$ and floquet wave vector of $0.4774(2\pi/a)$ is plotted on the right half of the figure. The dispersion relation of one-way chiral edge mode depends on the displacements of the boundary rods.

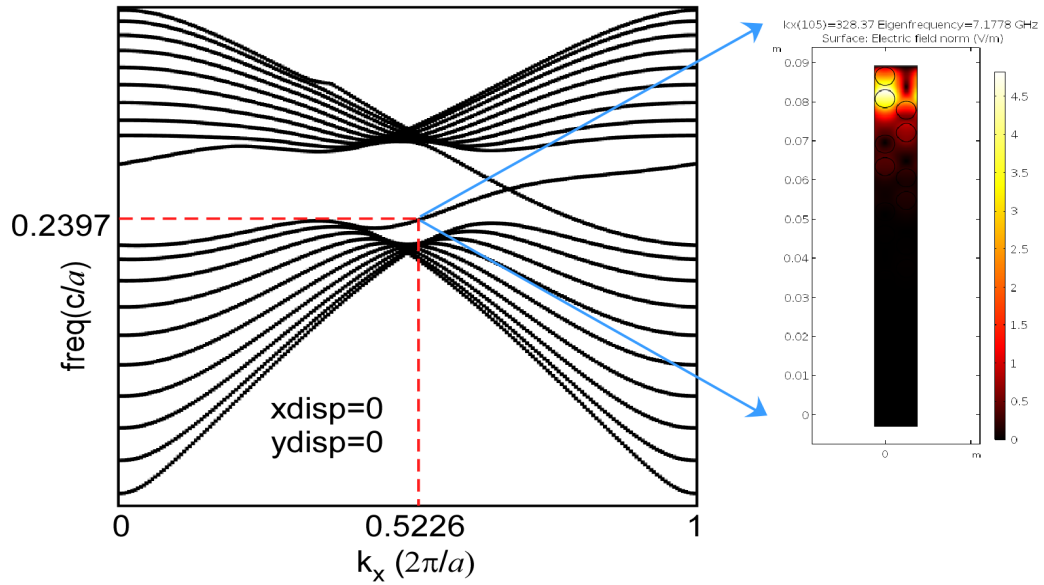


Figure 6.3: Band diagram and mode profile of chiral edge state when K' -group rods are the nearest to the top metal wall. Left: band diagram when the x-displacements of boundary rods and y-displacements of boundary rods are both 0. The normalized electric field intensity distribution corresponding to frequency of $0.2397(c/a)$ and floquet wave vector of $0.5226(2\pi/a)$ is plotted on the right half of the figure. The dispersion relation of one-way chiral edge mode also depends on the displacements of the boundary rods.

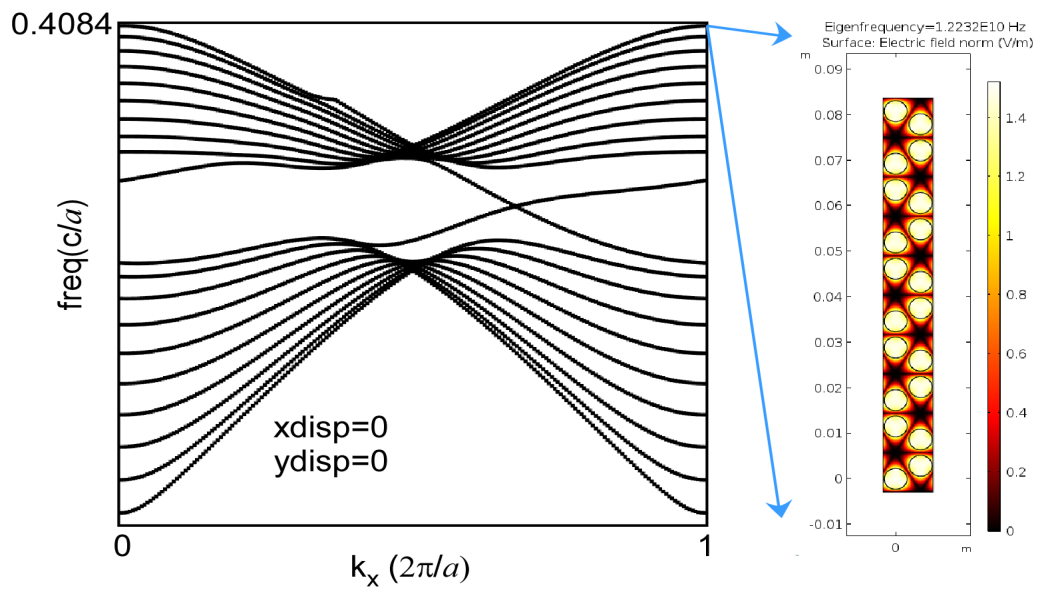


Figure 6.4: Band diagram and mode profile of “perfect” bulk mode. Left: band diagram when the x-displacements of boundary rods and y-displacements of boundary rods are both 0. The normalized electric field intensity distribution corresponding to frequency of $0.4084(c/a)$ and floquet wave vector of $1(2\pi/a)$ is plotted on the right half of the figure. The dispersion relation of this “perfect” bulk mode also depends on the displacements of the boundary rods.

6.3 RTOF based on phase response as a function of floquet wave vector

Even though normalized electric field profiles are important as indicators of locations of optical potential bottom, i.e. where the ferrite rods will be trapped, the actual optical force field is highly desired to reveal the real-world picture. However, the calculation of the optical force via Maxwell stress tensor by using the formula in Appendix A is computationally expensive and hard to reveal the optical potential shapes. The alternative way of calculating the optical force is to use the response theory of optical force (RTOF) which is previously shown in Eq. 3.1. Since in RTOF we need to extract the phase response at the output port, which can be found as the product between floquet wave vector and lattice constant, $k_x \cdot a$, in eigensolver simulating one single unit cell. Therefore, we want to, for each operating frequency, relate the optical force potential to the floquet wave vector defined in eigensolver via numerical interpolation.

6.3.1 Spatial phase response derived from floquet wave vector

Since the band diagrams shown in Fig. 6.2 - Fig. 6.4 depend on the displacements of boundary ferrite rods in magneto-optical photonic crystal, the chiral edge bands and “perfect” bulk bands for the boundary magneto-optical photonic crystal rods of Group K and Group K’ are calculated with respect to every movement of the boundary rods. The dependence of the dispersion relation on the displacements of boundary rods is demonstrated by

4 combinations of (x,y)-displacements in each case as shown in Fig. 6.5 - Fig. 6.8. In Fig. 6.5, the chiral edge modes (also called waveguide bands) for 4 combinations of (x,y)-displacements, i.e. $(0, 0.03a)$, $(0.06a, 0.03a)$, $(0, 0)$, and $(0.06a, 0)$, are plotted on the range of floquet k_x from $0.8(\pi/a) - 0.95(\pi/a)$. The dispersion relation is affected by the y-displacement more significantly than x-displacement, and therefore the optical force potential is expected to be more sensitive to y-displacement, which shall be discussed in more detail later. The individual floquet wave vector at certain operating frequency corresponding to different displacements can be then derived by the intersections between the dispersion relation curves and the isofrequency line at the operating frequency (the green dash horizontal line in Fig. 6.5). If we do exactly the same thing for every displacement for one operating frequency, we can derive the floquet wave vector map as a function of (x,y)-displacements, which is actually the phase map divided by the lattice constant a , which shall be shown later. Similarly, we can numerically calculate the dispersion relation of chiral edge state for the boundary magneto-optical rods belonging to the K'-group for different sets of (x,y)-displacements as shown in Fig. 6.6. As you can see from Fig. 6.6, the dispersion relation is almost not sensitive to the x-displacement, which results in smaller optical force F_x during the alignment process.

The “perfect” bulk modes for the boundary magneto-optical rods of Group K and Group K' of 4 different sets of (x,y)-displacements are calculated on a narrower range of floquet wave vector from $-0.015(\pi/a)$ to $0.015(\pi/a)$ because the desired bulk modes only appear near the zero wave vector, as shown

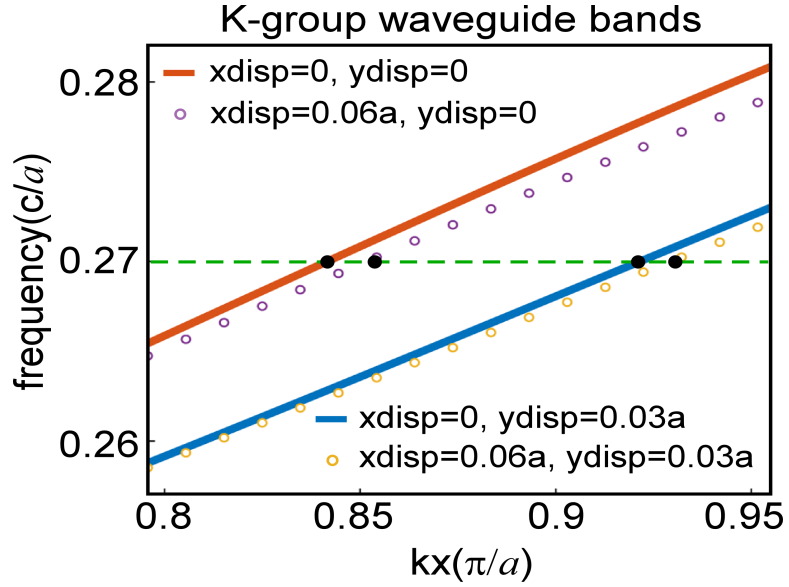


Figure 6.5: Dependence of dispersion relation of chiral edge state when the boundary magneto-optical rods belonging to K-group. At the operating frequency of $0.27(c/a)$, the floquet wave vector corresponding to different displacements can be found from the intersections between the dispersion relation curves and the isofrequency line shown as green dashed line. The dispersion relation is more sensitive to y-displacement, which results in larger vertical optical force along y-axis according to RTOF.

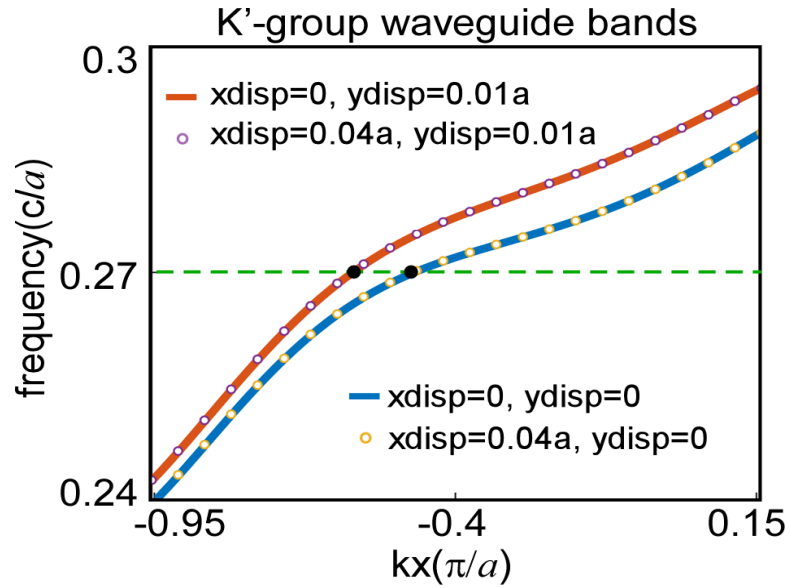


Figure 6.6: Dependence of dispersion relation of chiral edge state when the boundary magneto-optical rods belonging to K' -group. At the operating frequency of $0.27(c/a)$, the floquet wave vector corresponding to different displacements can be found from the intersections between the dispersion relation curves and the isofrequency line shown as green dashed line. In this case, the dispersion relation is not quite sensitive to x-displacement, which results in horizontal optical force along x-axis very small

in Fig. 6.7 and Fig. 6.8. However, near $k_x = 0$ the well-defined structure (the blue band in Fig. 6.7, $xdisp = 0, ydisp = 0$) has symmetric bulk mode which allows both right-propagating and left-propagating waves, and therefore there can be two floquet wave vectors corresponding to the intersections between the blue curve in Fig. 6.7 and the operating frequency along the horizontal direction. These two bulk modes result in one stable equilibrium point trapping the ferrite rods and the other unstable equilibrium point expelling the ferrite rods which will be shown later. Once the displacements are non-zero, the breaking of perfect superlattice will generate an one-way waveguide dispersion relation which is not symmetric with respect to $k_x = 0$ like the dispersion relation shown in red, for example, in Fig. 6.7. In this situation, the optical force potential only has a local minimum point which creates a stable equilibrium able to trap the ferrite rods. Moreover, due to the limit range of floquet wave vector, it is possible there is no intersection between certain bands with the horizontal operating frequency line in green. For example, the blue band in Fig. 6.7 has no intersection with the green dashed line, and thus at such operating frequency we cannot find the corresponding k_x within the available simulation data, which results in vacancies in Fig. 6.9.

Now that we already know the dispersion relations of both chiral edge states and “perfect” bulk modes for either K-group boundary rods and K'-group boundary rods depend on the displacements of the boundary rods, we can, for one chosen operating frequency, derive the phase $k_x a$ for every possible (x,y)-displacement. Four examples of phase maps are given in Fig. 6.9, where

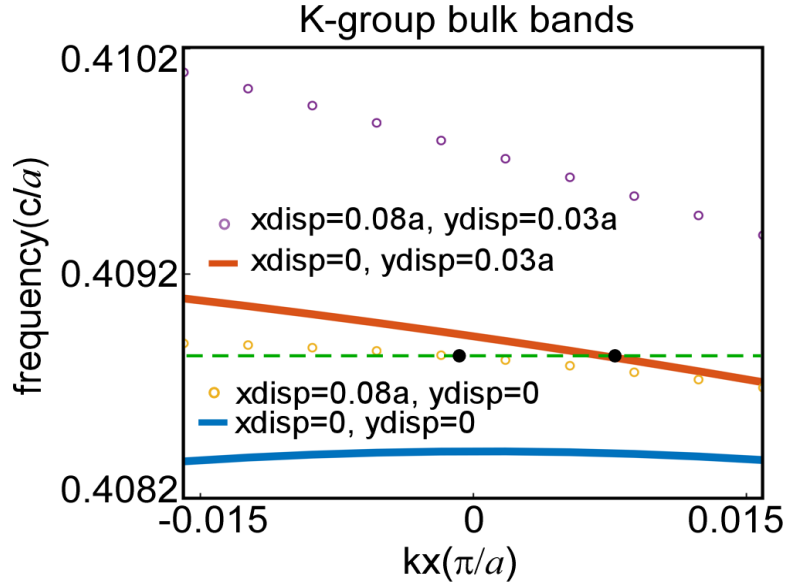


Figure 6.7: Dependence of dispersion relation of “perfect” bulk mode when the boundary ferrite rods belong to K-group. The floquet wave vector corresponding to different combinations of (x,y)-displacements can be found from the intersections between the dispersion curves and the isofrequency line in green. Since the dispersion relations of displacements $(0.08a, 0.03a)$ and $(0, 0)$ do not have intersections with the dashed green line, the floquet wave vectors at this operating frequency are not available at this two displacements based on the existing simulation data.

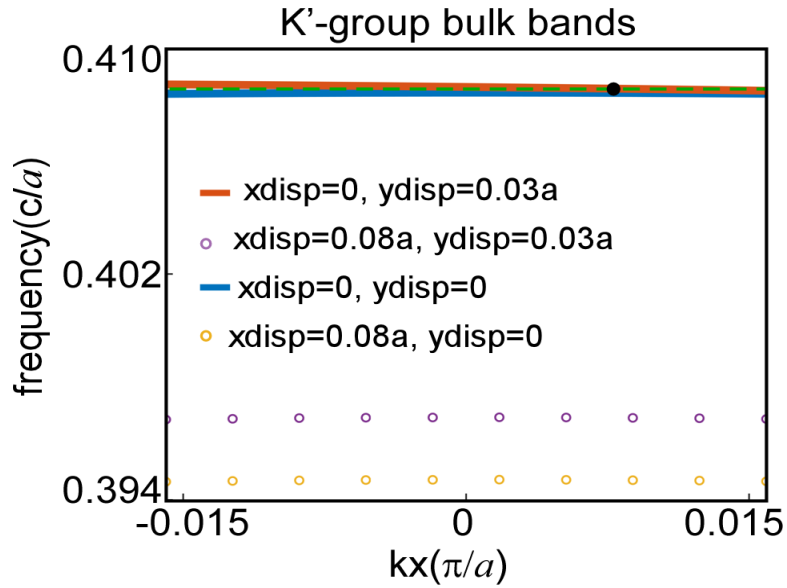


Figure 6.8: Dependence of dispersion relation of “perfect” bulk mode when the boundary ferrite rods belong to K' -group. The floquet wave vector corresponding to different combinations of (x,y)-displacements can be found from the intersections between the dispersion relation curve and the green horizontal isofrequency line. In this case, since the dispersion relation weakly depends on y-displacement, the optical force long y-direction is expected to be much smaller than the optical force along x-direction.

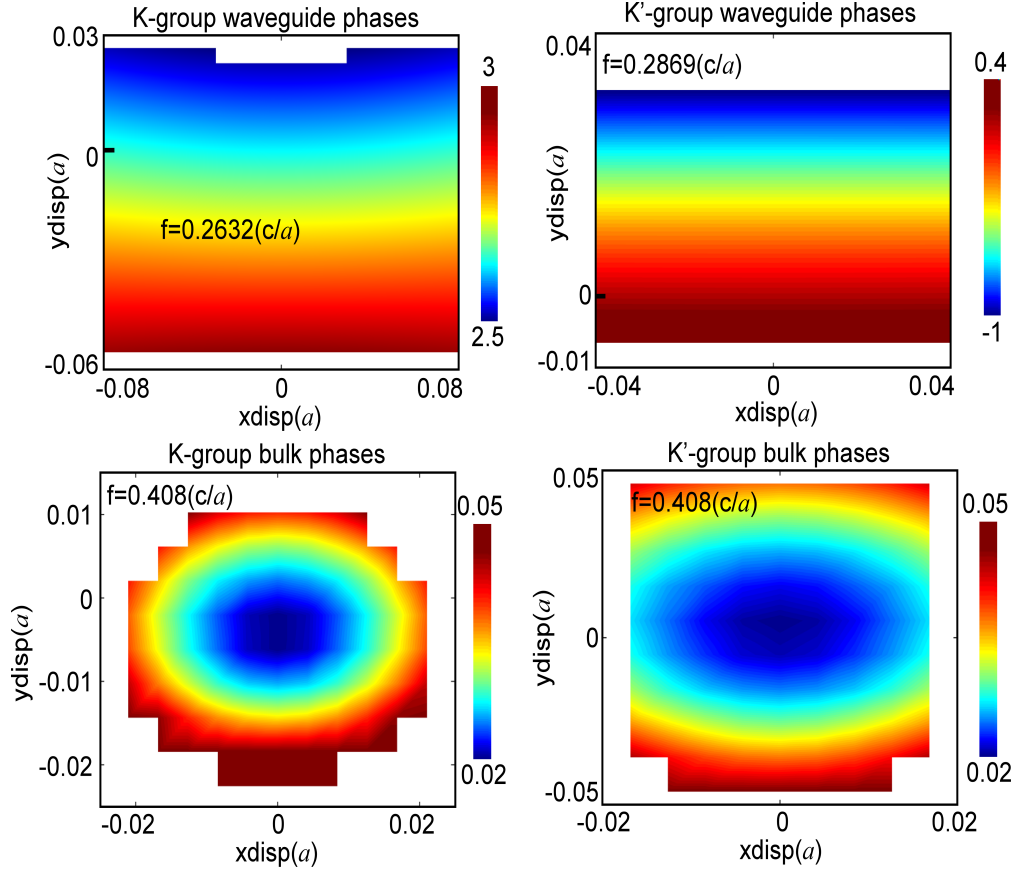


Figure 6.9: Four examples of phase maps at one single operating frequency. (a) phase map at the frequency of $0.2532(c/a)$ when the chiral edge state is excited for the boundary magneto-optical rods of Group K. (b) phase map at the frequency of $0.2869(c/a)$ for the boundary magneto-optical rods of Group K' when the chiral edge state is excited. (c) phase map at the operating frequency of $0.408(c/a)$ for the boundary magneto-optical rods of Group K when the “perfect” bulk mode is excited. (d) phase map at the operating frequency of $0.408(c/a)$ for the boundary magneto-optical rods of Group K' when the “perfect” bulk mode is excited.

Fig. 6.9(a) shows the phase map for the movements of boundary magneto-optical rods of Group K at the frequency of $0.2632(c/a)$ at which the chiral edge state can be excited and Fig. 6.9(b) presents the phase map for the movements of boundary magneto-optical rods of Group K' at the frequency of $0.2869(c/a)$ when the chiral edge states are triggered as well. According to RTOF, i.e. $F = -1/\omega \nabla(k_x a) = -\nabla U$, the phase map is proportional to the optical force potential. The optical force generated by the chiral edge states in Fig. 6.9(a)(b) tends to push the boundary magneto-optical rods upwards along y-axis until they hit the metal wall for both K-group and K'-group structures. The following step is that we need the bulk modes to create conservative optical force fields which have minimum potential bottom around the target position of ferrite rods in a perfect structure. Fortunately, the phase maps at the frequency of $0.408(c/a)$ where the “perfect” bulk mode can be excited present phase minima for both boundary rods of Group K and Group K'.

6.3.2 Optical force exerted by edge topological modes

By using RTOF, the optical force can be calculated as the product between the inverse of the operating frequency and the gradient of the phase maps shown in Fig. 6.9. In this section, I show the agreement between RTOF and the surface integration of Maxwell stress tensor (expressions of MST are given in Appendix A) as shown in Fig. 6.10 and Fig. 6.11. Since the optical force potentials created by the chiral edge states are not sensitive to x-displacements as shown in Fig. 6.9 (a),(b), looking at the optical force in

further details helps to determine whether the equilibrium when optical force is zero is stable or unstable.

The x-components and y-components of the optical force generated by chiral edge states (or known as waveguide modes) behave quite differently, as whether F_x is stable or not not only depends on the frequency but also depends on y-displacements, while F_y always pushes the boundary rods towards the metal wall. For example, F_x generated by chiral edge states on boundary rods of Group K at the operating frequency of $0.2632(c/a)$ can trap the rods to the perfect location when y-displacements are $0.02a$ and $-0.01a$ and expel the rods when y-displacement is $-0.05a$ as shown in Fig. 6.10(a). Similar force behavior on the boundary rods of Group K' can be seen in Fig. 6.10(c). We can deduce that, when y-displacement is zero, the optical force is able to trap the boundary magneto-optical rods to the perfect location along x-axis. However, the optical force generated by chiral edge states along y-direction cannot align the boundary magneto-optical rods of either Group K or Group K'. This task will be accomplished by using the “perfect” bulk mode.

6.3.3 Optical force exerted by “perfect” bulk modes

Although the optical force generated by the chiral edge states can be used to align the boundary magneto-optical rods along x-direction, this optical force pushes the boundary rods towards the metal wall and thus the bulk modes are needed to create the optical force field to trap the boundary rods along y-direction. Fig. 6.11 (a), (b) show the F_x and F_y generated by the bulk

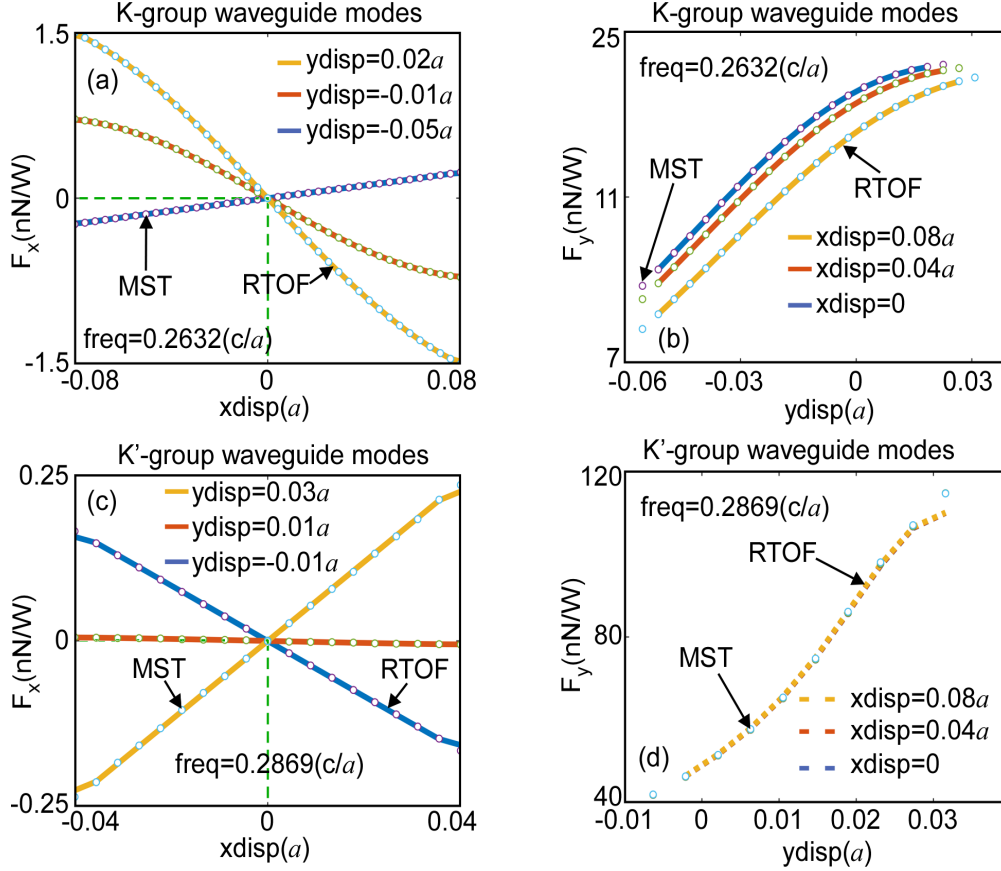


Figure 6.10: Agreement of the optical force calculation by using RTOF (curves) and Maxwell stress tensor integration (dots). (a) F_x on boundary magneto-optical rods of K-group at the frequency of $0.2632(c/a)$ for 3 y-displacements of $-0.05a$, $-0.01a$, and $0.02a$. (b) F_y on boundary magneto-optical rods of K-group at the operating frequency of $0.2632(c/a)$ for 3 x-displacements of 0 , $0.04a$, and $0.08a$. (c) F_x on boundary magneto-optical rods of K'-group at the operating frequency of $0.2869(c/a)$ for 3 y-displacements of $-0.01a$, $0.01a$, and $0.03a$. (d) F_y on boundary magneto-optical rods of K'-group at the operating frequency of $0.2869(c/a)$ for 3 x-displacements of 0 , $0.04a$, and $0.08a$.

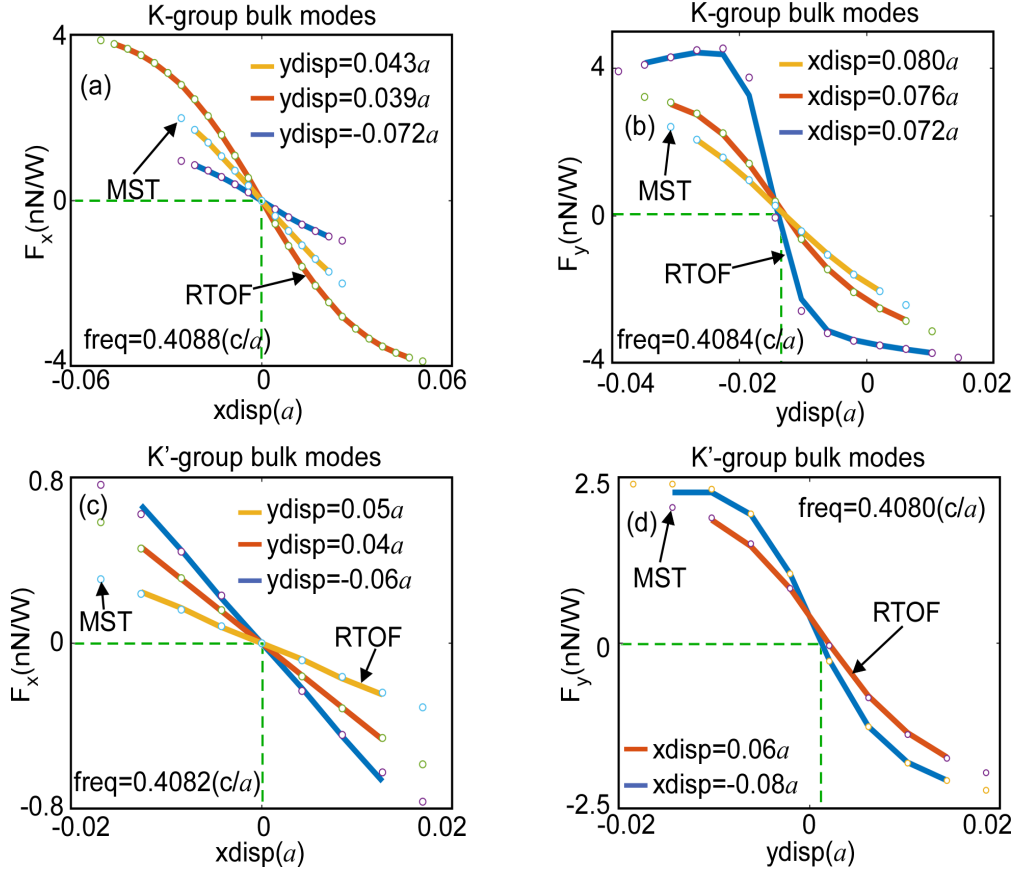


Figure 6.11: Agreement between RTOF and Maxwell stress tensor integration on optical force generated by bulk modes for boundary magneto-optical rods of Group K and Group K'. (a) F_x on boundary magneto-optical rods of K-group at the frequency of $0.4088(c/a)$ for y -displacements of $-0.072a$, $0.039a$, and $0.043a$. (b) F_y on boundary magneto-optical rods of K-group at the frequency of $0.4084(c/a)$ for x -displacements of $0.072a$, $0.076a$, and $0.080a$. (c) F_x on boundary magneto-optical rods of K'-group at the frequency of $0.4082(c/a)$ for the y -displacements of $-0.06a$, $0.04a$, and $0.05a$. (d) F_y on boundary magneto-optical rods of K'-group at the frequency of $0.4080(c/a)$ for x -displacements of $0.06a$ and $-0.08a$.

modes can trap the boundary magneto-optical rods of K-group along both x-direction and y-direction. Similarly, the boundary magneto-optical rods of K'-group can be trapped by the optical force generated by the bulk modes as well. By tuning the operating frequency, one can control the final position where the boundary ferrite rods will be trapped to.

6.4 Force potential as a function of operating frequencies for bulk modes

In Fig. 6.9, I gave the phase maps, which are proportional to the real optical force potential, for 4 different cases, each with a single operating frequency. Since the operating frequency plays a significant role in shaping the optical force potential, it is highly desirable to present the shapes of different optical force potential for arbitrary operating frequency. Therefore, the eigenfrequencies are plotted with respect to combinations of wave vectors and (x or y)-displacements, as shown in Fig. 6.12 and Fig. 6.13. The isofrequency contours for different operating frequencies are highlighted on these figures as well, and the interesting fact is that the frequency contour versus displacements is proportional to the optical force potential according to RTOF.

The optical force tends to trap the boundary magneto-optical rods to the target perfect position when the rods are offset from the origins. For instance, in Fig. 6.12 (a) and (b), both F_x and F_y at appropriate operating frequencies can trap the boundary rods to the location where the optical force potentials achieve their minima. At a closer examination, we can find F_x will

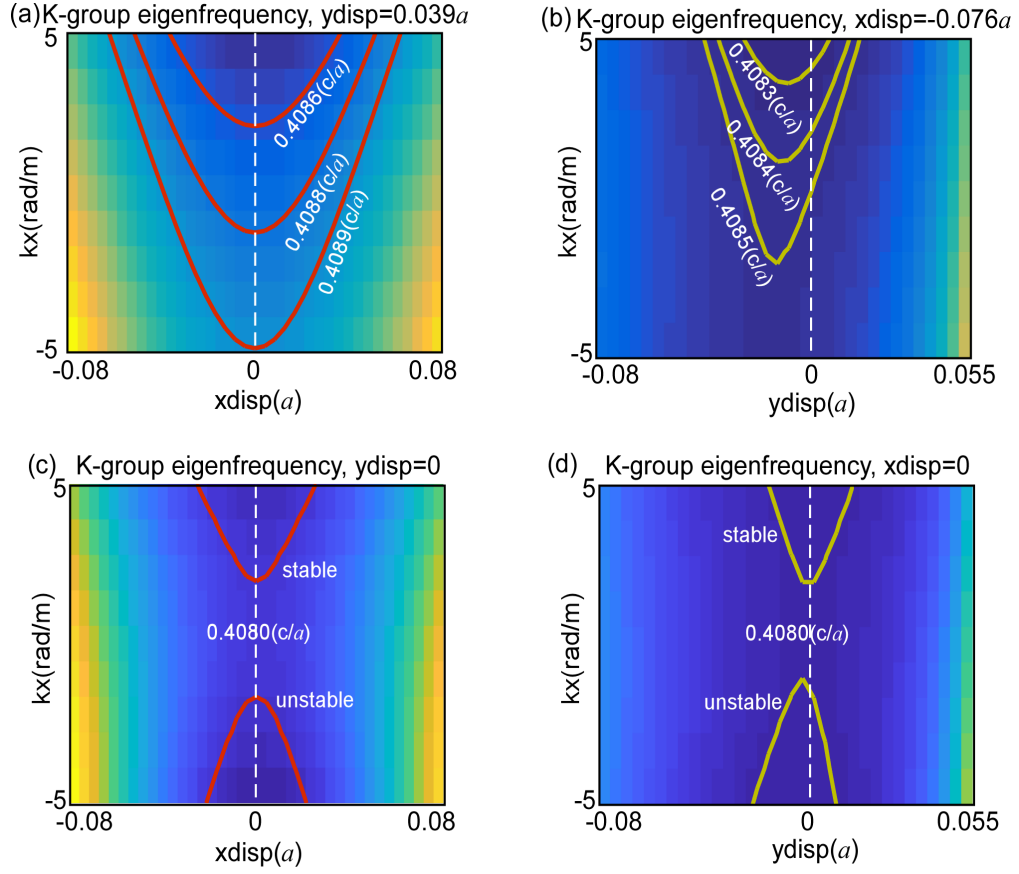


Figure 6.12: Eigenfrequencies versus floquet wave vectors and displacements for boundary rods of Group K. (a). Eigenfrequencies versus $(k_x, xdisp)$ when y -displacement= $0.039a$, the isofrequency contours of $0.4086(c/a)$, $0.4088(c/a)$, and $0.4089(c/a)$ are highlighted as red curves which is proportional to the optical force potential. (b) Eigenfrequencies versus $(k_x, ydisp)$ when x -displacement= $-0.076a$, and the isofrequency contours of $0.4083(c/a)$, $0.4084(c/a)$, and $0.4085(c/a)$ are highlighted by yellow curves. (c) Eigenfrequency versus $(k_x, xdisp)$ when y -displacement= 0 , and the isofrequency contour of $0.4080(c/a)$ is highlighted by red curves. The top branch indicates optical potential with minimum which will trap the boundary rods to $xdisp = 0$, while the lower branch means optical force potential expels the boundary rods away from the origins when the light propagates to $-x$ direction. (d) Eigenfrequency versus $(k_x, ydisp)$ when x -displacement= 0 , and the isofrequency= $0.4080(c/a)$ is highlighted by the yellow curves. Similarly, the top branch indicates stable equilibrium and the bottom branch means unstable equilibrium.

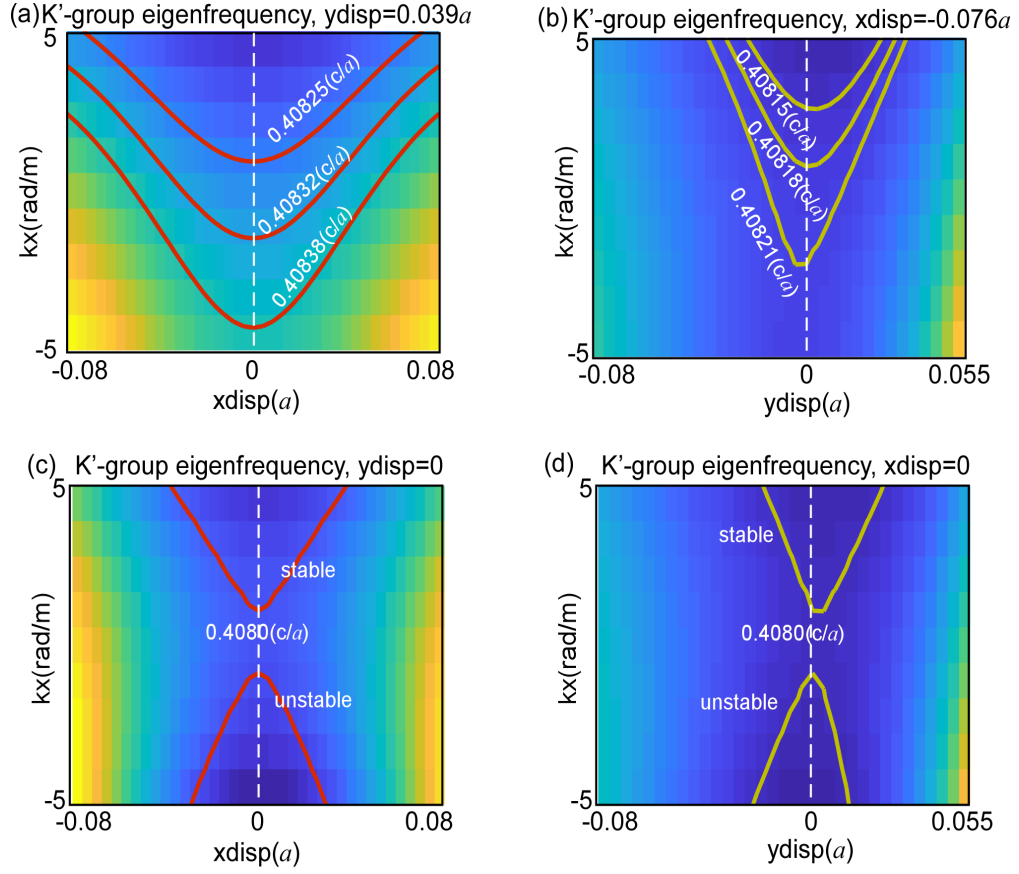


Figure 6.13: Eigenfrequencies versus floquet wave vectors and displacements for boundary rods of Group K'. (a). Eigenfrequencies versus $(k_x, xdisp)$ when y -displacement= $0.039a$, the isofrequency contours of $0.40825(c/a)$, $0.40832(c/a)$, and $0.40838(c/a)$ are highlighted as red curves which is proportional to the optical force potential. (b) Eigenfrequencies versus $(k_x, ydisp)$ when x -displacement= $-0.076a$, and the isofrequency contours of $0.40815(c/a)$, $0.40818(c/a)$, and $0.40821(c/a)$ are highlighted by yellow curves. (c) Eigenfrequency versus $(k_x, xdisp)$ when y -displacement= 0 , and the isofrequency contour of $0.4080(c/a)$ is highlighted by red curves. The top branch indicates optical potential with minimum which will trap the boundary rods to $xdisp = 0$, while the lower branch means optical force potential expels the boundary rods away from the origins when the light propagates to $-x$ direction. (d) Eigenfrequency versus $(k_x, ydisp)$ when x -displacement= 0 , and the isofrequency= $0.4080(c/a)$ is highlighted by the yellow curves. Similarly, the top branch indicates stable equilibrium and the bottom branch means unstable equilibrium.

always drag the boundary rods to $x_{disp} = 0$, and since the optical force potential along y-axis also depends on x-displacement the boundary rods will be finally trapped to $y_{disp} = 0$ as we can see from the upper branch of isofrequency contour in Fig. 6.12(d). One more thing worthy to be mentioned in Fig. 6.12(d) is that the lower isofrequency contour indicates that the boundary rods will be expelled from the origins when the floquet wave vector is along negative x-axis. However, once the boundary rods are pushed away from the origins, one-way waveguide will be created and the lower isofrequency contour will disappear, which means the boundary rods will be trapped back to the origins again. Similar conclusion can be drawn for the boundary rods of Group K' as we can see from Fig. 6.13.

6.5 Conclusion remarks

Unlike the magneto-optical photonic crystal of square lattice in which the optical power is outside the ferrite rods, the magneto-optical photonic crystal of honeycomb lattice has the optical power propagating within the ferrite rods, and therefore the honeycomb lattice is suitable to realize self-aligned photonic crystal. In row-by-row fabrication technique, the newly added row of rods with random positions forms a single-mode one-way waveguide, and the optical force capable of trapping the new row of rods, which is generated by the chiral edge states, is investigated in this chapter. In the finalized step, the optical force generated by the bulk mode is also studied, which is proved that when the optical modes are propagating along +x-direction the optical force

will trap the ferrite rods to the perfect locations. In the future, time-domain modulation on magneto-optical material is promising to bend down the left half of the “perfect” bulk mode and thus to remove the unstable equilibrium. In this case, the self-aligned topological photonic crystal will be completely realized.

Chapter 7

Acoustic trapping of phononic crystal slabs

7.1 Introduction

Even though Ch. 3 has shown the conservative optical force field can be constructed to automatically align the photonic crystal slabs in layer-by-layer fabrication technique, it is difficult to apply this optical alignment mechanism to larger objects because of small magnitude of the optical force. Due to the momentum conservation, the force exerted on certain object is given by $\mathbf{f} = \mathbf{P}/\mathbf{v}$ in the simplest scenario where all the incident wave is reflected back to the direction opposite to its incident direction, where \mathbf{P} is the energy flux or power and \mathbf{v} is the wave speed. Since the light speed is usually on the order of 10^8m/s even in dielectric material, the optical force is generally very weak and we have to design and fabricate ultra-high quality optical resonators so that the lifetimes of photons trapped in the optical resonators are long enough for photon-matter interaction and the oscillating mode in the resonator is significantly enhanced to generate a large optical force. Now that the optical force is hard to be implemented, we can use other forms of waves to realize the similar automatic alignment and trapping systems because the sufficient condition for conservative force derived previously has nothing to do with the type of force and thus can be applied to any single-port system. Since the sound speed is

6 orders lower than the light speed, thus the acoustic force is 6 orders larger than the optical force given that the input power is identical. Besides large force strength, the acoustic force is easy to be excited by piezoelectric material, safe to live cells, and transparent to light-opaque materials. However, the calculation of acoustic force based on the divergence of Reynold stress tensor (analogy to Maxwell stress tensor in Electromagnetics) has been under debate for almost 80 years. Until 2012, Bruus [9] introduced a correction form to Reynold stress tensor and derived correct form of calculating acoustic force for compressible objects of arbitrary shape (COMSOL expressions of Reynold stress tensor are given in Appendix A). His formula is further corroborated by the response theory of acoustic force (RTAF), and we can use the latter to predict the shape of acoustic potential based on the phase response.

7.2 Response theory of acoustic force – RTAF

During the design of a trapping system, a method capable of predicting the big picture of the force potential shape is very important. The response theory of acoustic force states that the force potential is proportional to the the phase response with respect to the displacements of the moving object. Therefore, if the correctness of RTAF is corroborated by the first-principle calculation of the acoustic force using Reynold stress tensor (RST), it will significantly facilitate the design and modeling of a mechanically variable system driven by the acoustic force. Furthermore, the response theory of acoustic force greatly simplifies the calculation of the acoustic pressure compared with

the traditional way using RST.

7.2.1 Reynold stress tensor: traditional way of calculating the acoustic radiation pressure

We start with the acoustic radiation pressure computed from Reynold stress tensor on a compressible object in nonviscous fluid when the gravity is neglected. If the shear mode is not considered, the time-averaged second-order pressure can be derived from the second-order Navier-Stokes equation (also known as momentum conservation) as [8, 9, 18, 68]

$$\langle p_2 \rangle = \frac{1}{2\rho_0 c_0^2} \langle p_1^2 \rangle - \frac{1}{2}\rho_0 \langle v_1^2 \rangle = \left\langle \frac{\rho_0}{2} \left(\frac{1}{c_0} \partial_t \phi \right) - \frac{\rho_0}{2} |\nabla \phi|^2 \right\rangle \quad (7.1)$$

where ρ_0 is the density of the surrounding fluid, c_0 is the sound speed in fluid, p_1 is the pressure of first-order perturbation with linear approximation (the product of two first-order perturbation is neglected), v_1 is the velocity of the first-order perturbation, and ϕ is the velocity potential. The $\langle A(t)B(t) \rangle = 1/2 \text{Re}[A_0 B_0^*]$ is the time-averaged integral over one period. The acoustic radiation pressure in the simplest form is given by the negative surface integral on a time-varying volume $V(t)$, which can be transformed to the surface integral on a fixed surface by adding a correction term, which is given by

$$\mathbf{F}^{rad} = - \int_{\partial V(t)} \langle p_2 \rangle d\mathbf{S} = - \int_{\partial V_{fixed}} d\mathbf{S} [\langle p_2 \rangle \mathbf{n} + \rho_0 \langle (\mathbf{n} \cdot \mathbf{v}_1) \mathbf{v}_1 \rangle] \quad (7.2)$$

where $\rho_0 \langle (\mathbf{n} \cdot \mathbf{v}_1) \mathbf{v}_1 \rangle$ is the correction term. The surface integral of Reynold stress tensor on a fixed surface can be easily calculated in finite-element sim-

ulations, and the detailed COMSOL expressions of RST both in 2D and 3D are given in Appendix A.

7.2.2 Agreement between RTAF and Reynold stress tensor

Derived from energy conservation, the response theory of acoustic force should give identical calculation results of traditional method using Reynold stress tensor, but in a much simpler way. The response theory of acoustic force only requires the output power and phase response at each output port as well as the movement information of the target object to calculate the acoustic force exerted on the moving part. Similar to RTOF, the RTAF is given by

$$\mathbf{F}^{rtaf} = \frac{Power}{\omega} \nabla \Phi \quad (7.3)$$

where ω is the angular frequency of the acoustic wave, Φ is the phase response at the output port, and the power of a plane sound wave can be calculated as $Area \cdot Pressure^2 / \rho_0 c_0$.

Before we rely on the formula of \mathbf{F}^{rtaf} to perform further analysis on force conservation, we need to make sure $\mathbf{F}^{rtaf} = \mathbf{F}^{rad}$ as a cross check of the valid force calculation. The correctness of RTAF has been verified by two examples as shown in Fig. 7.1 and Fig. 7.2. In Fig. 7.1, the movable nylon slab is put on top of a fixed substrate nylon slab and a layer of oil membrane to eliminate the friction (zero-friction assumption in finite-element simulations) is smeared on top surface of the substrate. The input pressure wave is only incident from the side of the substrate as shown in the illustration

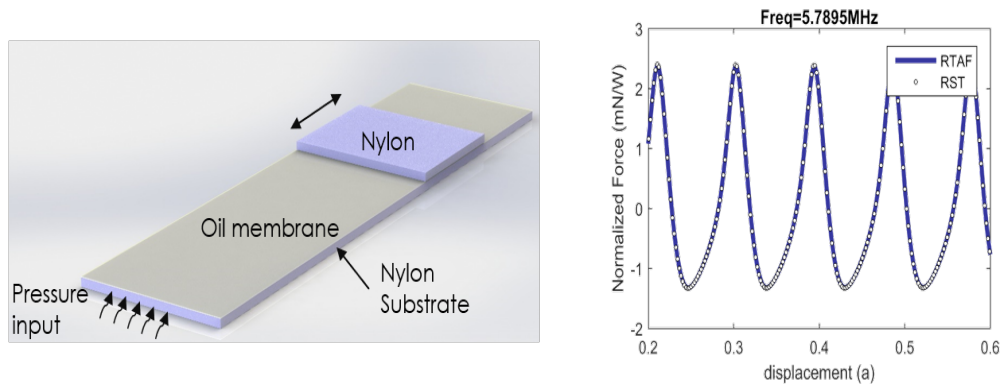


Figure 7.1: Agreement between the Reynold stress tensor and the response theory of acoustic force for 1D movement. The incident acoustic wave only consists of pressure wave and exerts on the bottom Nylon substrate, and therefore a single-port system is created. Because of the interference between the incident acoustic wave and the reflected acoustic wave, periodic acoustic intensity pattern is formed along the Nylon substrate and part of the acoustic power penetrates into the top movable Nylon slab. The top Nylon slab can freely slide on the oil membrane (assume no friction), and thus is trapped to highest acoustic intensity regions by acoustic gradient force.

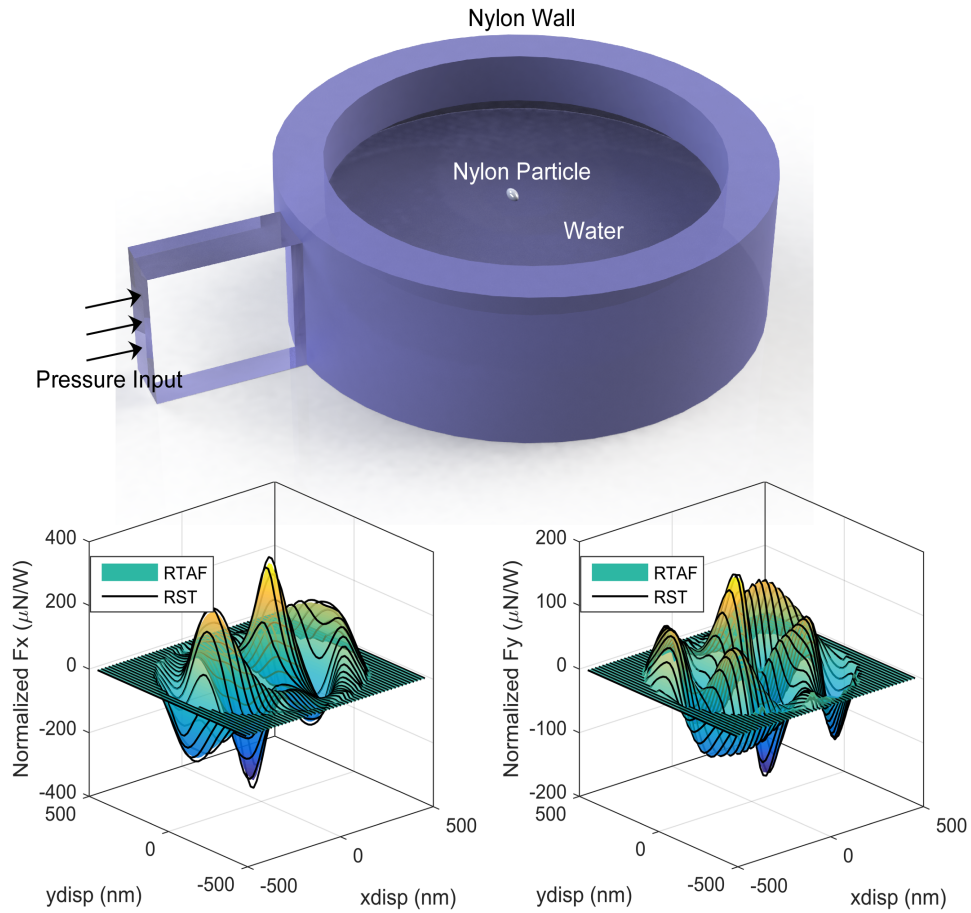


Figure 7.2: Agreement between the Reynold stress tensor and the response theory of acoustic force for 2D movement. The incident pressure wave hits the wall of the cylindrical cup made of Nylon and the elastic energy is transferred to the water inside the cup and applies acoustic radiation pressure on the small Nylon particle in the water. The radius of the Nylon cup is $500nm$, the longer side of the elliptical particle is $30.9nm$, and the shorter side of the elliptical particle is $19.1nm$.

of Fig. 7.1 and is able to create periodic force potential trapping the top moving slab because of the standing elastic wave formed by the interference between the incident wave and the reflected wave in the substrate. Even though this example is easy to be modeled in a 2D simulation, the top nylon slab can only move along the longer side of the substrate (1D movement) to verify the correctness of RTAF in 1D. To further verify the correctness of RTAF, another example where the nylon particle can move within a 2D plane is presented in Fig. 7.2. In this case, a small elliptical nylon particle can move in the water in a cylindrical cup made of nylon, and we can see both F_x and F_y calculated through RTAF and RST agree with each other as shown in the bottom half panel of Fig. 7.2. Even though both structures do not possess high-Q resonance, the normalized acoustic force per Watt is generally two orders higher the optical force generated by a high-Q optical resonance. Therefore, a significant enhancement in magnitude of the acoustic force over the optical force is expected in a well-designed acoustic system with high-Q resonance.

7.3 Conservative acoustic force in single-port system

As concluded from Ch. 3, a conservative force field can be established in a single-port system. Here, instead of using nonviscous fluidic pressure waveguide (only pressure wave or P-wave is supported in this kind of waveguide) which is hard to make in true experiments, I use a plane acoustic wave in free space to create a single-port acoustic system as shown in Fig. 7.3. Two iden-

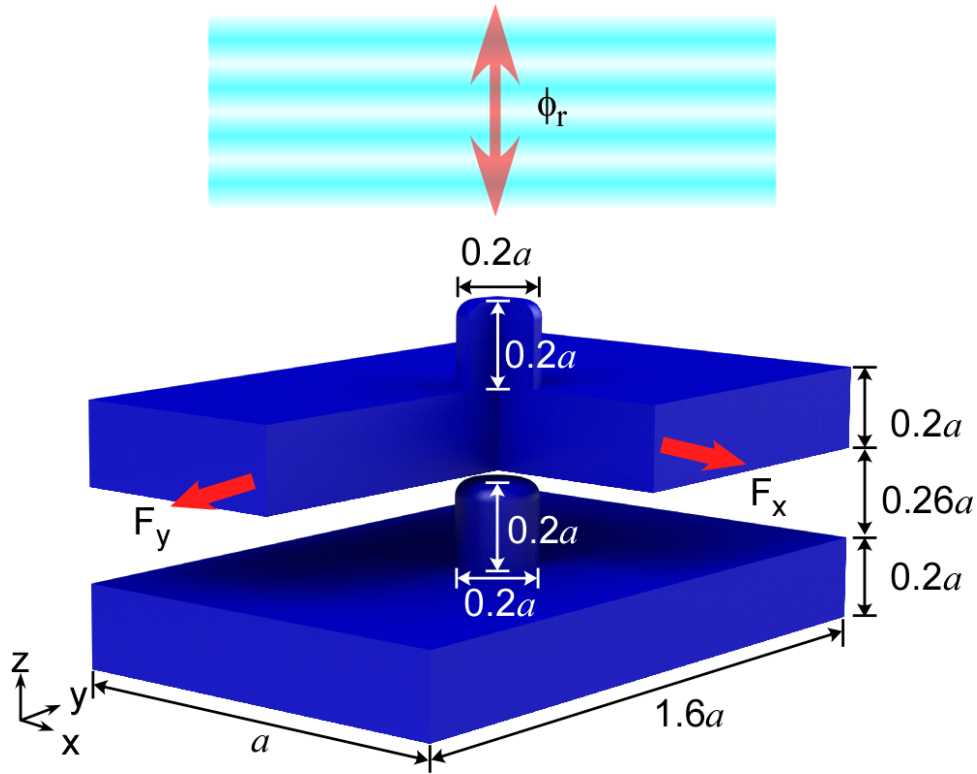


Figure 7.3: Structure of single-port acoustic system in which conservative acoustic force exerting on the top phononic crystal can be created. The width and length of one unit cell is a and $1.6a$, respectively, to separate two resonances far away enough from each other to simplify the data processing steps. The thickness of both slabs is kept as $0.2a$, and the distance between two slabs is $0.26a$. The height and diameter of the pillars on both slabs are $0.2a$. The plane acoustic pressure wave is incident from the top and is then completely reflected from the bottom sound hard wall. The phase difference between the incident wave and the reflected wave Φ_r is measured for every displacement of the upper phononic crystal slab.

tical phononic crystal slabs are stacked to form an acoustic resonator whose resonance and decay rates change with the displacements of the top phononic crystal slab. According to the temporal coupled mode theory, the phase response as a function of resonant frequencies and decay rates also depends on the displacements of the upper phononic crystal slab, and therefore an acoustic force potential which is proportional to the phase response can be constructed. Simply by tuning the operating frequency, the shape of acoustic potential can be modulated based on which one can choose the desired potential shape.

To implement the conclusion that trapping of the phononic crystal slab can be realized in a single-port system, we now look into details of this concrete example. The phononic crystal is made of rectangular lattice whose width is a and length is $1.6a$ to separate two resonant frequencies far away enough in frequency domain to ease the later data processing step. The thickness of the slab is $0.2a$, as well as the height and diameter of the rods. The phononic crystal slab on the top can move freely in xy -plane. The plane acoustic wave in free space is incident from the top and is completely reflected back because the bottom surface of the substrate phononic crystal is sound hard boundary, and therefore a single-port system is created. As the upper phononic crystal is moving, although the reflected acoustic wave power keeps constant, the acoustic force can be arise from the phase component and is conservative because of zero gradient of reflected acoustic power according to RTAF. For example, at the operating frequency of $0.1768(c/a)$, the phase response as the upper phononic crystal slab is moving from $-0.5b$ to $0.5b$ ($b = 1.6a$) along

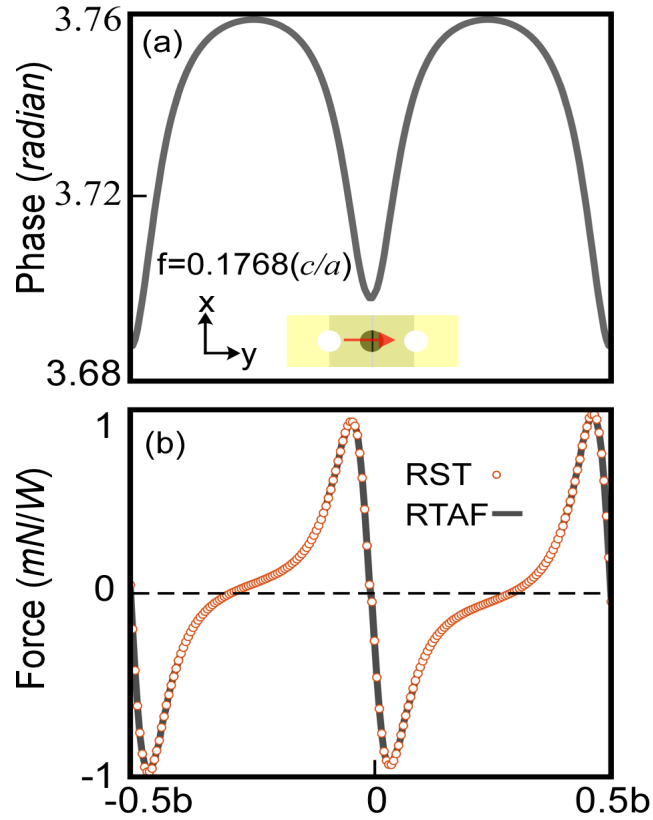


Figure 7.4: Acoustic force barrier formed along y-axis at the operating frequency of $0.1768(c/a)$. (a) the phase response as the upper phononic crystal is moving from $-0.5b$ to $0.5b$ along y-axis where $b = 1.6a$, as shown in the embedded illustration. This phase response is proportional to the actual acoustic force potential according to RTAF. (b) the acoustic force calculated using RTAF (curve) from the phase response has a perfect agreement with the first-principle calculation of the acoustic force using RST (dots). Note that the normalized acoustic force is on the scale of mN per Watt, which is much larger than the optical force, even though the stacked phononic crystal slabs at this operating frequency is not on resonance.

y-axis is shown in Fig. 7.4(a). Note that the system is not exactly on the resonance because the difference between the minimum and the maximum of the phase response is much smaller than 2π , but the acoustic force is already on the scale of mN/W which is 3 orders larger than the optical force even when the optical resonance is right on the resonance. As this finite-element simulation is computed in a 3D model, I use the RST in 3D case in Appendix A which verifies the correctness of RTAF formula shown in Fig. 7.4(b) in which RTAF has a perfect agreement with Reynold stress tensor.

7.3.1 Phase response predicted by temporal coupled mode theory

As explained in Ch.3, the temporal coupled mode theory is able to calculate the phase response for arbitrary operating frequency once the resonant frequencies and decay rates are already known, which not only saves a huge amount of simulation time but also helps us to determine the shape of acoustic potential shape based on the resonant frequency maps and to predict force strength by looking at the decay rate maps. In this single-port multiple resonance system, the complex reflection coefficient is given by

$$S = \frac{S_-}{S_+} = e^{i\phi_0} \left(1 + \frac{2i\gamma_A(\omega - \omega_B) + 2i\gamma_B(\omega - \omega_A)}{-(\omega - \omega_A)(\omega - \omega_B) - i\gamma_A(\omega - \omega_B) - i\gamma_B(\omega - \omega_A)} \right) \quad (7.4)$$

where $\omega_{A,B}$ are resonant frequencies and $\gamma_{A,B}$ are decay rates. The phase response predicted by Eq. 7.4 has a perfect agreement with that calculated from FEM simulations, as shown in Fig.7.5, for three different displacements $(0.5a, 0.5b)$ (green), $(0, 0.5b)$ (orange), and $(0.5a, 0)$ (blue). The first fact can

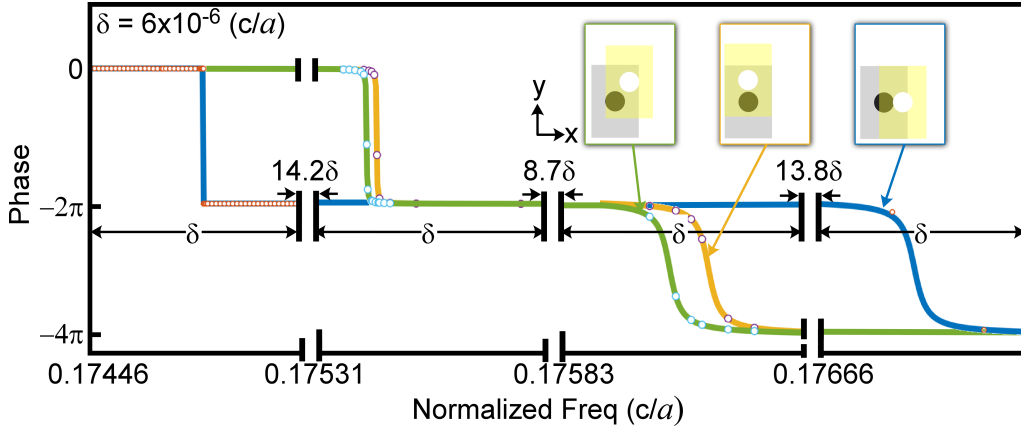


Figure 7.5: Fitting the temporal coupled mode theory (curves) to the first-principle FEM simulation (dots). The blue curve corresponds to displacements of $(0.5a, 0)$, the green curve corresponds to displacements of $(0.5a, 0.5b)$, and the orange curve corresponds to displacements of $(0, 0.5b)$. In all three cases, the phase response predicted by the temporal coupled mode theory have perfect agreement with those from FEM simulations. Different displacements of the upper phononic crystal slab will cause the resonant frequencies to change. Moreover, the dependence of the resonant frequency along y -direction is larger than that along x -direction.

be immediately found is that the resonant frequency depends on the displacement. At a closer look at the phase response, the resonant frequency is more dependent on y -displacement than x -displacement, as half-cell y -displacement will shift the resonant frequency more than 10δ but the half-cell x -displacement can only shift the resonant frequency within 1δ . Moreover, decay rates also depend on the displacements because the decay rate is obviously the smallest when both x -displacement and y -displacement are zero where the 2π phase transition is sharper than anywhere else.

7.3.2 System characterization using temporal coupled mode theory

In the last section, I showed the fitting of the temporal coupled mode theory to the phase response calculated from the first-principle FEM simulations for only 3 sets of displacements. The same procedure can be repeated for every displacement of the upper moving phononic crystal in xy-plane, and thus we can derive the resonant frequencies and decay rates as functions for every displacement in xy-plane as shown in Fig. 7.6. Unlike the stacked photonic crystal slabs, both the resonant frequency maps and decay rate maps in stacked phononic crystal slabs are not quite sensitive to x-displacement as those to y-displacements. Therefore, it is highly possible to create acoustic potential barrier along y-axis and hard to create round or elliptical potential wells as in electromagnetic counterpart. On the other hand, similar to photonic crystal slabs, the high quality factor guarantees favorably large acoustic force to trap the phononic crystal slab along y-direction.

7.3.3 Realization of 1D acoustic trapping along the longer side of phononic crystal unit cell

1D acoustic trapping along the longer side of the phononic crystal unit cell can be constructed by carefully choosing the operating frequency. However, 2D acoustic trapping is only possible within a very narrow bandwidth of the operating frequency because the resonant frequency maps of stacked phononic crystal slabs do not vary obviously with the displacements long the shorter side of the phononic crystal unit cell, which is quite different from the

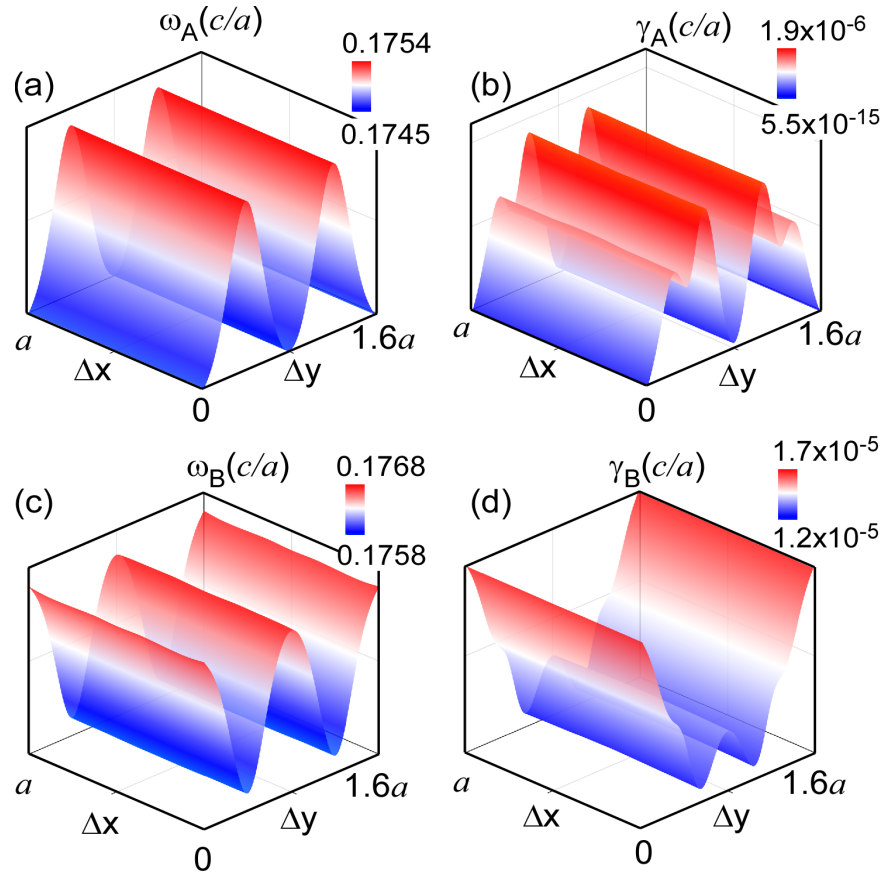


Figure 7.6: Resonant frequency maps and decay rate maps with respect to the displacements of the upper phononic crystal slab in xy -plane. (a) resonant frequency map of the red resonance with respect to the displacements in xy -plane. (b) decay rate maps of the red resonance with respect to the displacements in xy -plane. (c) resonant frequency map of the blue resonance with respect to the displacements in xy -plane. (d) decay rate maps of the blue resonance with respect to the displacements in xy -plane. Both red resonant frequency and blue resonant frequency are not sensitive to x -displacement compared with their dependence on y -displacement. Similarly, decay rates are more dependent on y -displacement than x -displacement. Since the shape of acoustic force potential is determined by the resonant frequency map, it is much easier to create 1D acoustic barrier along y -direction without fine tuning of the operating frequency.

stacked photonic crystal slabs.

To illustrate how the resonant frequency map facilitates the prediction of acoustic force potential, one example of operating frequency of $0.1766(c/a)$ is given in Fig. 7.7. The isofrequency plane at $0.1766(c/a)$ is shown in green in Fig. 7.7(a), which intersects with the blue resonant frequency map already presented in Fig. 7.6(c). Whenever the operating frequency hits the resonant frequency, a phase transition of 2π is triggered at that displacement and therefore we can construct the phase map at the operating frequency with 2π phase transition at the intersections in Fig. 7.7(a). Based on RTAF, the sharp and huge phase variation will produce favorably large acoustic force. For example, if we cut the phase map in Fig. 7.7 (b) at the plane of $\Delta x = 0.5a$, the cross section is black curve as shown in Fig. 7.7(c) based on whose gradient the acoustic force can be calculated using RTAF and agrees with the traditional force calculation via RST as shown in Fig. 7.7(d). As previously mentioned, this acoustic force is 3 orders higher than the optical force in this similar structure (even optical resonator possesses a much higher Q-factor up to 6×10^8 , while acoustic resonator generally has Q-factor on the order of 10^{4-5}) because of much lower sound speed compared with the light speed. This normalized acoustic force on the order of N per $Watt$ is more suitable for realistic application in auto-alignment than the optical force which is on the order of mN per $Watt$. Also, the plane acoustic wave in free space is easier to generate than plane optical wave which requires collimated laser beam.

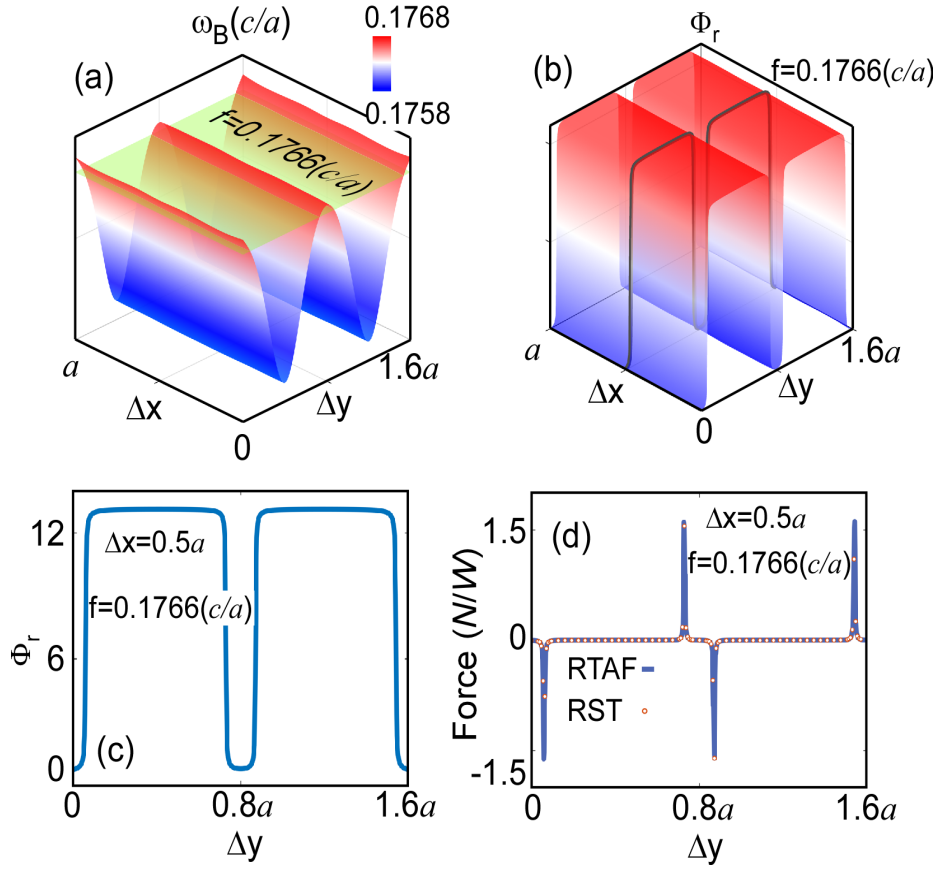


Figure 7.7: 1D acoustic potential barrier as well as acoustic force calculated based on resonant frequency map and decay rate map derived from the temporal coupled mode theory. (a) intersection between the isofrequency plane of $0.1766(c/a)$ and the resonant frequency map of the blue resonance. The curves at the intersections determines the shape of acoustic force potential. (b) The phase response predicted by the temporal coupled mode theory at the operating frequency of $0.1766(c/a)$. The 2π phase transition happens at the displacements where the operating frequency plane intersects with the resonant frequency map. The intersection between the cut plane at $\Delta x = 0.5a$ and the phase response map is shown as the black curve. (c) the intersection between the cut plane at $\Delta x = 0.5a$ and the phase response map, i.e. the black curve in (b). (d) the acoustic force calculated based on the phase response in (c) using RTAF agrees with the acoustic force calculated using RST. Since the single-port CMT is used to do RTAF calculation, the acoustic force is conservative.

7.4 Computation Concerns

Even though the structure has been carefully selected and designed to avoid complicated and fine features, the 3D FEM simulation of stacked phononic crystal slabs mentioned in last section is very computationally expensive. The whole simulations in 7.3.1 is finished on distributed computation platform consisting of 4 servers (CPUs: 2 of Xeon E5-1650 and 2 of Xeon E3-1245) connected with high-bandwidth optical internet network. Unlike multicore platform where a shared memory is accessible by all CPUs, the distributed computation infrastructure adopts a message-passing mechanism to realized parallelism. To minimize the information transmitted via network, the task is parallelized according to displacements and operating frequencies, so that only two variables and computed phase/power/RST are transported within the network. Compared with sequential computation program, the total simulation time is reduced by 80%.

7.5 Conclusion Remarks

In this chapter, I presented the response theory of acoustic force which calculates the force from the point of view of energy conservation. The perfect agreement between RTAF and RST with correction term given by Bruus et al corroborates the correct form of calculating the acoustic radiation pressure which was under long-time debate until 2012. More importantly, RTAF provides concise insight to the force property in an acoustic system, which facilitate the design and modeling of a mechanically driven system by the

acoustic force.

Even though a concrete example realizing acoustic trapping is given in this chapter, 2D acoustic trapping is hard to construct in this kind of stacked phononic crystal slabs system because of insensitive change of the resonant frequency with respect to the displacement along certain direction. However, one can still use this structure to do automatic alignment in layer-by-layer fabrication technique, in which we can have two sets of perpendicular stacked phononic crystal attached to the corners of the wafers and each set of phononic crystal is responsible for aligning the wave in their own prefer direction.

Appendices

Appendix A

General stress tensor expressions in COMSOL

A.1 General Maxwell Stress Tensor in COMSOL

General form of MST in Eq 2.9 is suitable to compute the total force for any type of material such as anisotropic material or even magneto photonic crystals. The default MST in COMSOL such as “dnTx”, “unTx”, “dnTy”, “unTy”, “dnTz”, and “unTz” require one to artificially plot a bigger box enclosing the target entirely and integrate the MST over the surface of the box to calculate the total optical force coming from radiation pressure. The MST expressions in this chapter is adapted to do the integral right on the surface of the target without necessity of the outer box, even if the permittivity or permeability at the interface jumps. Again, it is suitable for any kinds of materials and has been verified through comparison with default MST expressions in COMSOL.

$$\begin{aligned} uT_{mx} &= 0.5 * \text{real} \left(\text{up}(\text{emw}.Bx) * (\text{up}(\text{conj}(\text{emw}.Hx)) * \text{emw}.unx + \text{up}(\text{conj}(\text{emw}.Hy)) * \text{emw}.uny + \text{up}(\text{conj}(\text{emw}.Hz)) * \text{emw}.unz) - 0.5 * \right. \\ &\quad \left. \text{emw}.unx * (\text{up}(\text{emw}.Bx) * \text{up}(\text{conj}(\text{emw}.Hx)) + \text{up}(\text{emw}.By) * \text{up}(\text{conj}(\text{emw}.Hy)) + \text{up}(\text{emw}.Bz) * \text{up}(\text{conj}(\text{emw}.Hz))) \right) \\ dT_{mx} &= 0.5 * \text{real} \left(\text{down}(\text{emw}.Bx) * (\text{down}(\text{conj}(\text{emw}.Hx)) * \text{emw}.dnx + \right. \\ &\quad \left. \text{down}(\text{conj}(\text{emw}.Hy)) * \text{emw}.dny + \text{down}(\text{conj}(\text{emw}.Hz)) * \text{emw}.dnz) - 0.5 * \text{emw}.dnx * \right. \\ &\quad \left. (\text{down}(\text{emw}.Bx) * \text{down}(\text{conj}(\text{emw}.Hx)) + \text{down}(\text{emw}.By) * \text{down}(\text{conj}(\text{emw}.Hy)) + \text{down}(\text{emw}.Bz) * \text{down}(\text{conj}(\text{emw}.Hz))) \right) \end{aligned}$$

$$\begin{aligned}
& \text{emw.unz} * (\text{up}(\text{emw.Dx}) * \text{up}(\text{conj}(\text{emw.Ex})) + \text{up}(\text{emw.Dy}) * \text{up}(\text{conj}(\text{emw.Ey})) + \text{up}(\text{emw.Dz}) * \text{up}(\text{conj}(\text{emw.Ez}))) \\
dTez = & 0.5 * \text{real}(\text{down}(\text{emw.Dz}) * (\text{down}(\text{conj}(\text{emw.Ex})) * \text{emw.dnx} + \text{down}(\text{conj}(\text{emw.Ey})) * \text{emw.dny} + \text{down}(\text{conj}(\text{emw.Ez})) * \text{emw.dnz}) \\
& - 0.5 * \text{emw.dnz} * (\text{down}(\text{emw.Dx}) * \text{down}(\text{conj}(\text{emw.Ex})) + \text{down}(\text{emw.Dy}) * \text{down}(\text{conj}(\text{emw.Ey})) + \text{down}(\text{emw.Dz}) * \text{down}(\text{conj}(\text{emw.Ez}))))
\end{aligned}$$

A.2 General Reynold Stress Tensor in COMSOL

The Reynold stress tensor in COMSOL can be computed as

2D-axisymmetric structure in Pressure-acoustics model

$$\begin{aligned}
p2av &= 0.25 / \text{rho0} / c0^2 * \text{abs}(\text{acpr.p_t})^2 - 0.5 * \text{rho0} * \text{acpr.v_rms}^2 \\
f1densz &= p2av * \text{acpr.nz} \\
f1densr &= p2av * \text{acpr.nr} \\
f2densz &= 0.5 * \text{rho0} * (\text{real}(\text{conj}(\text{acpr.vz}) * (\text{acpr.vr} * \text{acpr.nr} + \text{acpr.vz} * \text{acpr.nz}))) \\
f2densr &= 0.5 * \text{rho0} * (\text{real}(\text{conj}(\text{acpr.vr}) * (\text{acpr.vr} * \text{acpr.nr} + \text{acpr.vz} * \text{acpr.nz}))) \\
Fz &= -\text{intop1}(f1densz + f2densz)
\end{aligned}$$

3D structure in Pressure-acoustics model

$$\begin{aligned}
fx &= ((1 / (2 * \text{rho0} * c0^2) * \text{acpr.p_t} * \text{conj}(\text{acpr.p_t}) / 2 - 1 / 2 * \text{rho0} * (\text{acpr.vx} * \text{conj}(\text{acpr.vx}) + \text{acpr.vy} * \text{conj}(\text{acpr.vy}) + \text{acpr.vz} * \text{conj}(\text{acpr.vz})) / 2) * \text{acpr.nx} + \text{rho0} * \text{real}((\text{acpr.nx} * \text{acpr.vx} + \text{acpr.ny} * \text{acpr.vy} + \text{acpr.nz} * \text{acpr.vz}) * \text{conj}(\text{acpr.vx}))) / 2) \\
fy &= ((1 / (2 * \text{rho0} * c0^2) * \text{acpr.p_t} * \text{conj}(\text{acpr.p_t}) / 2 - 1 / 2 * \text{rho0} * (\text{acpr.vx} * \text{conj}(\text{acpr.vx}) + \text{acpr.vy} * \text{conj}(\text{acpr.vy}) + \text{acpr.vz} * \text{conj}(\text{acpr.vz})) / 2) * \text{acpr.ny} + \text{rho0} * \text{real}((\text{acpr.nx} * \text{acpr.vx} + \text{acpr.ny} * \text{acpr.vy} + \text{acpr.nz} * \text{acpr.vz}) * \text{conj}(\text{acpr.vy}))) / 2) \\
fz &= ((1 / (2 * \text{rho0} * c0^2) * \text{acpr.p_t} * \text{conj}(\text{acpr.p_t}) / 2 - 1 / 2 *
\end{aligned}$$

```

rho0*(acpr.vx*conj(acpr.vx)+acpr.vy*conj(acpr.vy)+
acpr.vz*conj(acpr.vz))/2)*acpr.nz+rho0*real((acpr.nx*
acpr.vx+acpr.ny*acpr.vy+acpr.nz*acpr.vz)*conj(acpr.vz
))/2)
Fx = -intop1(fx)
Fy = -intop1(fy)
Fz = -intop1(fz)

```

Appendix B

Time reversal symmetry

Time reversal symmetry provides another set of solution to dynamic equation and transfer function of temporal coupled mode theory. If all the progresses could run backward in time, we can imagine the fields would recover to their primary states which can be depicted by a similar but not identical set of solutions to Maxwell equations. While implementing time reversal symmetry, one must be careful about which quantities should be flipped. For example, if the polarization of electric field E_o remains unchanged, the sign of magnetic field H_o must be reversed so that the field propagates in opposite direction to original wave. Accordingly, t must be replaced by $-t$, for example, to make the following Maxwell equations equivalent

$$\nabla \times (E_o e^{-i\omega t}) + \mu_o \frac{\partial (H_o e^{-i\omega t})}{\partial t} = \nabla \times (E_o e^{i\omega t}) + \mu_o \frac{\partial (-H_o e^{i\omega t})}{\partial (-t)} = 0 \quad (\text{B.1})$$

Left-hand side of first equality sign is original Maxwell equation and right-hand side of first equality sign is written in time-reversal manner. For a lossless isotropic medium in which $\varepsilon = \varepsilon^*$, $\mu = \mu^*$, one can take the complex conjugate for the above equation to make ω real so that

$$\nabla \times (E_o e^{-i\omega t}) + \mu_o \frac{\partial (-H_o e^{-i\omega t})}{\partial (-t)} = 0 \quad (\text{B.2})$$

In resonator-waveguide system, the localized mode in resonator decays into waveguide mode with a real photon lifetime τ so that the mode amplitude has a form of $A(t) = A(0)e^{-i\omega_0 t - t/\tau}$ to satisfy the dynamic equation of $dA/dt = -i\omega_0 A - A/\tau$. Instead of exponentially decay into waveguide, the localized mode amplitude exponentially grows as fields feed into resonant cavity in time reversal symmetry with a form of $A(t) = A(0)e^{-i\omega_0 t + t/\tau^*}$. Although the photon lifetime here is real so that it equals to its complex conjugate, the off-diagonal elements in decay matrix $\mathbf{\Gamma}$ are not real if two cavity modes do not decay symmetrically or anti-symmetrically due to mirror symmetry breaking. In this case, we have to take complex conjugate for decay matrix in time reversal symmetry because the phases must accumulate in time reversal manner if they previously lost in original form when coupled to waveguides. In general, the localized mode profile presented by electric field in time reversal symmetry should be expressed as

$$[A(t) = [A(-t)]^* = A^* e^{-i\omega t + t/\tau} \quad (\text{B.3})$$

One the other hand, the propagation modes in time reversal symmetry are simply complex conjugates of the old fields in opposite directions because they are not time-dependent but only directional. It is straightforward that, if phases of original outgoing fields accumulated, new phases should decay as incident waves running backward in time. Therefore, the propagation modes in time reversal symmetry are written as

$$|S_{\pm}\rangle = |S_{-(\pm)}\rangle^* \quad (\text{B.4})$$

Any resonator-to-waveguide transfer matrix \mathbf{K} or \mathbf{D} relating incident waves to localized mode or localized mode to outgoing waves should preserve their primary form because even in time reversal symmetry localized modes and propagation modes must interact with the same fashion as before. In addition, the consideration of phase accumulation or lost has been already included in $A(t)$ and $|S_{\pm}\rangle$ such that \mathbf{K} and \mathbf{D} only depend on medium and structure. To summarize, in time reversal symmetry, the dynamic response equation is written as

$$(-i\omega\mathbf{I} + i\Omega + \Gamma^*) \begin{bmatrix} A^* \\ B^* \end{bmatrix} = \mathbf{K}^T |S_{-}\rangle^* \quad (\text{B.5})$$

Applying complex frequency $\omega = \Omega + i\Gamma$ in time reversal symmetry and $|S_{-}\rangle = \mathbf{D} \begin{bmatrix} A \\ B \end{bmatrix}$ as original propagation modes excited only by resonant cavity to have

$$2\Gamma^* = \mathbf{K}^T \mathbf{D}^* \quad (\text{B.6})$$

Recall that $\mathbf{D}^\dagger \mathbf{D} = 2\Gamma$, we can finally arrive at

$$\mathbf{K} = \mathbf{D} \quad (\text{B.7})$$

Appendix C

Upper limit of truncation error in periodic Helmholtz-Hodge decomposition

Here I present the upper limit of truncation error in periodic Helmholtz-Hodge decomposition and show the nearly linear dependence of truncation error on the single-side truncated period. Getting rid of the scaling factor δ in Eq. 3.26, the divergence-free component can be found by adopting analytical gradient of 2D Green's function and replacing summation in discrete HHD by smooth double integral as

$$\begin{aligned} f(n) &\triangleq \sum_{j_n} \nabla \times G(r_i - r_{j_n}) \cdot u(r_{j_n}) \\ &= \frac{1}{2\pi} \int_{x,y=(n-\frac{1}{2})a}^{x,y=(n+\frac{1}{2})a} \left(\frac{x}{x^2+y^2} u_y - \frac{y}{x^2+y^2} u_x \right) dx dy \end{aligned} \quad (\text{C.1})$$

Without explicit analytical expressions of u_x and u_y , it is impossible to accurately estimate the value of $f(n)$. To make the matter clear and simple, if we assume the vector field has a central-symmetry as well as u_x and u_y are independent of x and y , respectively, we can further simplify Eq. C.1 by integrating x for first term and y for second term to arrive at

$$\begin{aligned} f(n) &= \int_{(n-\frac{1}{2})a}^{(n+\frac{1}{2})a} u_x \ln \frac{[(n+\frac{1}{2})a]^2+x^2}{\sqrt{(na)^2+x^2} \sqrt{[(n+1)a]^2+x^2}} dx \\ &\quad - \int_{(n-\frac{1}{2})a}^{(n+\frac{1}{2})a} u_y \ln \frac{[(n+\frac{1}{2})a]^2+y^2}{\sqrt{(na)^2+y^2} \sqrt{[(n+1)a]^2+y^2}} dy \end{aligned} \quad (\text{C.2})$$

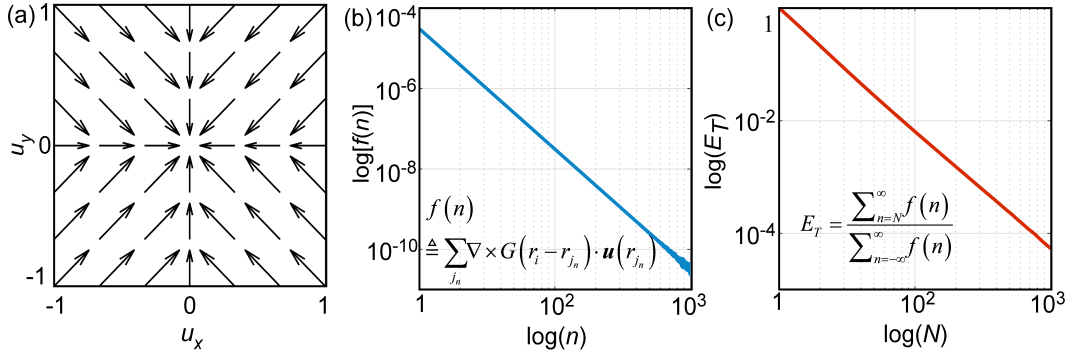


Figure C.1: Linear dependence of truncation error on truncation period in log-log scale. (a) Conservative periodic vector field with both u_x and u_y are -1 in $[-1, 0]$ and 1 in $[0, 1]$; (b) $f(n)$ which is convolution between curl of Greens Function and the periodic vector field in the n^{th} period vanishes at infinity, and it blurs at large n due to limitation of precision of numeric data type of machine; (c) Truncation error E_T presents a linear dependence on truncation period N in log-log scale.

If u_x and u_y have finite values, $f(n)$ obviously approaches to zero as the truncated period n goes to infinity. Furthermore, we can easily calculate $f(n)$ once we know the vector field either analytically or from numerical simulations and practical experiments. The convergence of truncation error with increasing truncation period of a testing vector field which is periodic and conservative is numerically plotted in $\log - \log$ scale in Fig. C.1. Two components of the testing force field u_x and u_y are both set to be 1 in $[(n - \frac{1}{2})a, na]$ and -1 in $[na, (n + \frac{1}{2})a]$ ($a = 2$) as shown in Fig. C.1(a). In this case, $f(n)$ is plotted in Fig.C.1(b) which decreases with increasing n , and it becomes blurred around $n = 1000$ due to precision of numeric data type of machine. It is obvious that the testing vector field is conservative and the truncation error has a rate of

convergence equal to approximately 2 with respect to truncation period N as shown in Fig. C.1(c)

$$\log E_T = \log \frac{\sum_{n=N}^{\infty} f(n)}{\sum_{n=-\infty}^{\infty} f(n)} \approx -2 \log n + C \quad (\text{C.3})$$

Appendix D

Weak-form formula for electromagnetic fields

D.1 Weak form for E-field

In the case when the permeability μ is anisotropic and \mathbf{r} dependent, and ϵ is a complex constant depicting the material loss. The electric field can be written as $\mathbf{E}(\mathbf{r}) = \mathbf{u}(\mathbf{r}) e^{-i\mathbf{k}\cdot\mathbf{r}}$. By using the equation that $\nabla \times (\alpha \mathbf{V}) = \alpha \nabla \times \mathbf{V} + \nabla \alpha \times \mathbf{V}$ we can find the curl of the electric field as $\nabla \times \mathbf{E} = e^{-i\mathbf{k}\cdot\mathbf{r}} \nabla \times \mathbf{u} + \nabla e^{-i\mathbf{k}\cdot\mathbf{r}} \times \mathbf{u} = e^{-i\mathbf{k}\cdot\mathbf{r}} (\nabla \times \mathbf{u} - i\mathbf{k} \times \mathbf{u})$. Starting from the wave equation

$$\nabla \times \left(\frac{1}{\mu} \nabla \times \mathbf{E} \right) - \epsilon \frac{\omega^2}{c^2} \mathbf{E} = 0$$

we can reorganize the wave equation and remove $e^{-i\mathbf{k}\cdot\mathbf{r}}$ on both sides as

$$\begin{aligned} & \nabla \times \left[\frac{1}{\mu} e^{-i\mathbf{k}\cdot\mathbf{r}} (\nabla \times \mathbf{u} - i\mathbf{k} \times \mathbf{u}) \right] - \epsilon \frac{\omega^2}{c^2} \mathbf{u} e^{-i\mathbf{k}\cdot\mathbf{r}} = 0 \\ & \nabla \times \left[e^{-i\mathbf{k}\cdot\mathbf{r}} \frac{1}{\mu} (\nabla \times \mathbf{u}) \right] - \nabla \times \left[e^{-i\mathbf{k}\cdot\mathbf{r}} \frac{1}{\mu} (i\mathbf{k} \times \mathbf{u}) \right] - \epsilon \frac{\omega^2}{c^2} \mathbf{u} e^{-i\mathbf{k}\cdot\mathbf{r}} = 0 \\ & \left\{ e^{-i\mathbf{k}\cdot\mathbf{r}} \nabla \times \left[\frac{1}{\mu} (\nabla \times \mathbf{u}) \right] + \nabla e^{-i\mathbf{k}\cdot\mathbf{r}} \times \left[\frac{1}{\mu} (\nabla \times \mathbf{u}) \right] \right\} - \\ & \left\{ e^{-i\mathbf{k}\cdot\mathbf{r}} \nabla \times \left[\frac{1}{\mu} (i\mathbf{k} \times \mathbf{u}) \right] + \nabla e^{-i\mathbf{k}\cdot\mathbf{r}} \times \left[\frac{1}{\mu} (i\mathbf{k} \times \mathbf{u}) \right] \right\} - \epsilon \frac{\omega^2}{c^2} \mathbf{u} e^{-i\mathbf{k}\cdot\mathbf{r}} = 0 \\ & \left\{ \nabla \times \left[\frac{1}{\mu} (\nabla \times \mathbf{u}) \right] - i\mathbf{k} \times \left[\frac{1}{\mu} (\nabla \times \mathbf{u}) \right] \right\} - \\ & \left\{ \nabla \times \left[\frac{1}{\mu} (i\mathbf{k} \times \mathbf{u}) \right] - i\mathbf{k} \times \left[\frac{1}{\mu} (i\mathbf{k} \times \mathbf{u}) \right] \right\} - \epsilon \frac{\omega^2}{c^2} \mathbf{u} = 0 \end{aligned}$$

$$\begin{aligned} \nabla \times \left[\frac{1}{\mu} (\nabla \times \mathbf{u}) \right] - i\mathbf{k} \times \left[\frac{1}{\mu} (\nabla \times \mathbf{u}) \right] - i\nabla \times \left[\frac{1}{\mu} (\mathbf{k} \times \mathbf{u}) \right] - \mathbf{k} \times \left[\frac{1}{\mu} (\mathbf{k} \times \mathbf{u}) \right] - \varepsilon \frac{\omega^2}{c^2} \mathbf{u} &= 0 \\ -\mathbf{k} \times \left[\frac{1}{\mu} (\mathbf{k} \times \mathbf{u}) \right] - i\mathbf{k} \times \left[\frac{1}{\mu} (\nabla \times \mathbf{u}) \right] - i\nabla \times \left[\frac{1}{\mu} (\mathbf{k} \times \mathbf{u}) \right] + \nabla \times \left[\frac{1}{\mu} (\nabla \times \mathbf{u}) \right] - \varepsilon \frac{\omega^2}{c^2} \mathbf{u} &= 0 \end{aligned}$$

By using another vector equation $A \cdot (B \times C) = B \cdot (C \times A) = C \cdot (A \times B)$,

we can finally derive the weak-form for E-field as

$$\begin{aligned} & \mathbf{v} \cdot \left\{ \begin{aligned} & -\mathbf{k} \times \left[\frac{1}{\mu} (\mathbf{k} \times \mathbf{u}) \right] - i\mathbf{k} \times \left[\frac{1}{\mu} (\nabla \times \mathbf{u}) \right] - \\ & i\nabla \times \left[\frac{1}{\mu} (\mathbf{k} \times \mathbf{u}) \right] + \nabla \times \left[\frac{1}{\mu} (\nabla \times \mathbf{u}) \right] - \varepsilon \frac{\omega^2}{c^2} \mathbf{u} \end{aligned} \right\} \\ &= (\mathbf{k} \times \mathbf{v}) \cdot \left[\frac{1}{\mu} (\mathbf{k} \times \mathbf{u}) \right] + i(\mathbf{k} \times \mathbf{v}) \cdot \left[\frac{1}{\mu} (\nabla \times \mathbf{u}) \right] - \\ & i(\nabla \times \mathbf{v}) \cdot \left[\frac{1}{\mu} (\mathbf{k} \times \mathbf{u}) \right] + (\nabla \times \mathbf{v}) \cdot \left[\frac{1}{\mu} (\nabla \times \mathbf{u}) \right] - \frac{\omega^2}{c^2} \mathbf{v} \cdot \varepsilon \mathbf{u} \end{aligned}$$

D.2 Weak form for H-field

Similar to derivation of weak form for E-field, the periodic harmonic magnetic field is expressed as

$$\mathbf{H}(r) = \mathbf{u}(r)e^{(i\omega t - i\mathbf{k} \cdot \mathbf{r})}$$

, and the curl of the magnetic field can be then written as ($e^{i\omega t}$ is neglected)

$$\nabla \times \mathbf{H} = e^{-i\mathbf{k} \cdot \mathbf{r}} (\nabla \times \mathbf{u} - i\mathbf{k} \times \mathbf{u})$$

. Start from the wave equation

$$\nabla \times \left(\frac{1}{\varepsilon} \nabla \times \mathbf{H} \right) - \mu \frac{\omega^2}{c^2} \mathbf{H} = 0$$

and follow the steps in the last section, one can derive the weak form for H-field

as

$$\begin{aligned} & \mathbf{v} \cdot \left\{ \begin{aligned} & -\frac{\mathbf{k}}{\varepsilon} \times (\mathbf{k} \times \mathbf{u}) - i\mathbf{k} \times \left(\frac{1}{\varepsilon} \nabla \times \mathbf{u} \right) - \\ & i\nabla \times \left(\frac{1}{\varepsilon} \mathbf{k} \times \mathbf{u} \right) + \nabla \times \left[\frac{1}{\varepsilon} (\nabla \times \mathbf{u}) \right] - \mu \frac{\omega^2}{c^2} \mathbf{u} \end{aligned} \right\} \\ &= -(\mathbf{k} \times \mathbf{v}) \cdot \frac{1}{\varepsilon} (\mathbf{k} \times \mathbf{u}) - i(\mathbf{k} \times \mathbf{v}) \cdot \left(\frac{1}{\varepsilon} \nabla \times \mathbf{u} \right) - i(\nabla \times \mathbf{v}) \cdot \left(\frac{1}{\varepsilon} \mathbf{k} \times \mathbf{u} \right) \\ &+ (\nabla \times \mathbf{v}) \cdot \left(\frac{1}{\varepsilon} \nabla \times \mathbf{u} \right) - \frac{\omega^2}{c^2} \mathbf{v} \cdot \vec{\mu} \mathbf{u} \end{aligned}$$

The coded weak-form expressions in COMSOL is given below (Note these expressions are suitable for lossy topological photonic crystals with active shells):

```

k0 2*pi*freq0 [Hz]/c_const ""
kx lambda[1/m] "" "show default solver" to blacken
    lambda/periodic along x-direction"
ky 0[1/m] ""
kz 0[1/m] ""
ux 0[V/m] "uz is dependent"
uy 0[V/m] "uz is dependent"
kcrossux ky*uz-kz*uy ""
kcrossuy kz*ux-kx*uz ""
kcrossuz kx*uy-ky*ux ""
curlux d(uz,y) d(uz,y)-d(uy,z)
curluy -d(uz,x) d(ux,z)-d(uz,x)
curluz 0[V/m^2] d(uy,x)-d(ux,y)
epsilon_r_xx epsr ""
epsilon_r_yy epsr ""
epsilon_r_zz epsr ""
mur_xx mur_diag ""
mur_xy mur_offdiag ""
mur_xz 0 ""
mur_yx -mur_offdiag ""
mur_yy mur_diag ""
mur_yz 0 ""
mur_zx 0 ""
mur_zy 0 ""
mur_zz mur_diag ""
epsrinv_xx 1/epsilon_r_xx ""
epsrinv_yy 1/epsilon_r_yy ""
epsrinv_zz 1/epsilon_r_zz ""
murinv_xx murinv_diag ""
murinv_xy murinv_offdiag ""
murinv_xz 0 ""
murinv_yx -murinv_offdiag ""
murinv_yy murinv_diag ""

```

```

murinv_yz 0 ""
murinv_zx 0 ""
murinv_zy 0 ""
murinv_zz murinv_diag1 ""
weak1Ez k0^2*(test(ux)*epsilon_r_xx*ux+test(uy)*
epsilon_r_yy*uy+test(uz)*epsilon_r_zz*uz) ""
weak2Ez -(test(curlux)*(murinv_xx*curlux+murinv_xy*
curluy+murinv_xz*curluz)+test(curluy)*(murinv_yx*
curlux+murinv_yy*curluy+murinv_yz*curluz)+test(curluz
)*(murinv_zx*curlux+murinv_zy*curluy+murinv_zz*curluz
)) ""
weak3Ez 1i*(test(curlux)*(murinv_xx*kcrossux+murinv_xy*
kcrossuy+murinv_xz*kcrossuz)+test(curluy)*(murinv_yx*
kcrossux+murinv_yy*kcrossuy+murinv_yz*kcrossuz)+test(
curluz)*(murinv_zx*kcrossux+murinv_zy*kcrossuy+
murinv_zz*kcrossuz)) ""
weak4Ez -1i*(test(kcrossux)*(murinv_xx*curlux+murinv_xy*
curluy+murinv_xz*curluz)+test(kcrossuy)*(murinv_yx*
curlux+murinv_yy*curluy+murinv_yz*curluz)+test(
kcrossuz)*(murinv_zx*curlux+murinv_zy*curluy+
murinv_zz*curluz)) ""
weak5Ez -(test(kcrossux)*(murinv_xx*kcrossux+murinv_xy*
kcrossuy+murinv_xz*kcrossuz)+test(kcrossuy)*(
murinv_yx*kcrossux+murinv_yy*kcrossuy+murinv_yz*
kcrossuz)+test(kcrossuz)*(murinv_zx*kcrossux+
murinv_zy*kcrossuy+murinv_zz*kcrossuz)) ""

```

Appendix E

MATLAB codes for HHD

E.1 Sequential program

```
1 function [phi,psi,curlfree_x,curlfree_y,divfree_x,
   divfree_y,hx,hy] = gfm2dhhd(Vx,Vy,x,y,delta,pcb,
   num_period)
2 % GFM2DHHD (Green's Function Method 2D Helmholtz-Hodge
   Decomposition) is
3 % used to decompose vector field into curl-free part and
   divergence-free
4 % part based on Green's Function via minimizing
   Dirichlet energy, i.e.
5 % least squares method.
6 % Vx and Vy are input vector field components which can
   be either aperiodic
7 % or periodic by setting pcb to be 0 or 1, respectively.
   For non-periodic
8 % application, Vx and Vy have to vanish at the boundary,
   and for periodic
9 % application when div-free potential is zero, Vx(:,1)=
   Vx(:,end+1) which
10 % can be shifted to zero, Vx(1,:)=Vx(end+1,:) which is
   not zero, Vy(1,:) =
11 % Vy(end+1,:) which can be shifted to 0, and Vy(:,1)=Vy
   (,:,end+1) which must
12 % not be zero.
13 % x and y are coordinates after meshgrid, default grid
   size is 1.
14 % delta: regulization factor, default value is 1e-6.
15 % num_period: number of period emanating from original
```

```

    unit cell, default
16 % value is 5.
17 % pbc: periodic boundary condition is set to 1 by
    default. Thus, to
18 % decompose an aperiodic vector field, pbc needs to be
    0.
19 % phi: curl-free potential, or scalar potential.
20 % psi: div-free potential (only z-component because x
    and y components are
21 % both zero).
22 % curlfree_x/curlfree_y: curl-free components of vector
    fields
23 % divfree_x/divfree_y: divergence-free components of
    vector fields.
24 % hx/hy: harmonic remainder.
25 % [phi, psi, curlfree_x, curlfree_y, divfree_x, divfree_y, hx,
    hy] = gfm2dhhd(Vx, Vy)
26 % [phi, psi, curlfree_x, curlfree_y, divfree_x, divfree_y, hx,
    hy] = gfm2dhhd(Vx, Vy, x, y)
27 % [phi, psi, curlfree_x, curlfree_y, divfree_x, divfree_y, hx,
    hy] = gfm2dhhd(Vx, Vy, x, y, delta)
28 % [phi, psi, curlfree_x, curlfree_y, divfree_x, divfree_y, hx,
    hy] = gfm2dhhd(Vx, Vy, x, y, delta, pbc, num_period)
29
30 % -Hui Dong- edited on April 27th, 2014, revised on May
    19, 2014 -
31 % $Version1.2$
32 [num_row, num_column] = size(Vx);
33 if (nargin == 2)
34     x = 1:num_column;
35     y = 1:num_row;
36     [x, y] = meshgrid(x, y);
37     delta = 1e-6;
38     pbc = 1;
39     num_period = 5;
40 elseif (nargin == 4)
41     delta = 1e-6;

```

```

42     pbc = 1;
43     num_period = 5;
44 elseif (nargin == 5)
45     pbc = 1;
46     num_period = 5;
47 end
48 xgrid = abs(x(1,2)-x(1,1));
49 ygrid = abs(y(2,1)-y(1,1));
50
51 phi = NaN(num_row,num_column);
52 psi = NaN(num_row,num_column);
53 [num_xgrid,num_ygrid] = meshgrid(0:num_column,0:num_row)
    ;
54 rx = xgrid*num_xgrid;
55 ry = ygrid*num_ygrid;
56 if pbc == 0
57     GFquarter = -1/2/pi*log(sqrt(rx.^2+ry.^2));
58     GFquarter(1,1) = -1/2/pi*log(sqrt(delta));
59 else
60     [xextend,yextend] = meshgrid((num_column-1)*(-
        num_period:num_period),(num_row-1)*(-num_period:
        num_period));
61     xextend = xgrid*xextend; yextend = ygrid*yextend;
62     rx_pb = kron(rx,ones(2*num_period+1))+repmat(xextend
        ,num_row+1,num_column+1);
63     ry_pb = kron(ry,ones(2*num_period+1))+repmat(yextend
        ,num_row+1,num_column+1);
64     temp = -1/2/pi*log(sqrt((rx_pb).^2+(ry_pb).^2));
65     temp(temp == inf)=-1/2/pi*log(sqrt(delta));
66     temp = mat2cell(temp,(2*num_period+1)*ones(1,num_row
        +1),(2*num_period+1)*ones(1,num_column+1));
67     temp = cellfun(@sum,temp,'UniformOutput',false);
68     temp = cellfun(@sum,temp,'UniformOutput',false);
69     GFquarter = cell2mat(temp);
70 end
71 GreenF = [rot90(GFquarter,2), flipud(GFquarter); fliplr(
    GFquarter),GFquarter]; GreenF(num_row+1,:) = []; GreenF

```

```

        (:, num_column+1) = [];
69 [dGx_whole, dGy_whole] = gradient(GreenF, xgrid, ygrid);
70
71 h = waitbar(0, '1', 'Name', ['Decomposing ', num2str(num_row
    ), 'x', num2str(num_column), ' vector matrix']);
72 for icolumn = 1:num_column
73     for irow = 1:num_row
74         dGx = dGx_whole(num_row+2-irow:end-irow,
            num_column+2-icolumn:end-icolumn);
75         dGy = dGy_whole(num_row+2-irow:end-irow,
            num_column+2-icolumn:end-icolumn);
76         phi(irow, icolumn) = sum(sum(dGx.*Vx+dGy.*Vy))*
            xgrid*ygrid;
77         psi(irow, icolumn) = sum(sum(dGy.*Vx-dGx.*Vy))*
            xgrid*ygrid;
78     end
79     formatSpec = 'Computing the %03dth column';
80     waitbar(icolumn/num_column, ...
81         h, sprintf(formatSpec, icolumn));
82 end
83
84 [divfree_x, divfree_y] = gradient(psi, xgrid, ygrid);
85 temp = divfree_x;
86 divfree_x = divfree_y;
87 divfree_y = -temp;
88 [curlfree_x, curlfree_y] = gradient(phi, xgrid, ygrid);
89 hx = Vx-curlfree_x-divfree_x;
90 hy = Vy-curlfree_y-divfree_y;
91 delete(h)

```

E.2 Parallel program

```

1 function [phi, psi, curlfree_x, curlfree_y, divfree_x,
    divfree_y, hx, hy, GreenF] = parGFM2DHHD(Vx, Vy, x, y, delta
    , pbc, num_period)
2 % GFM2DHHD (Green's Function Method 2D Helmholtz-Hodge
    Decomposition) is
3 % used to decompose vector field into curl-free part and

```

```

    divergence-free
4  % part based on Green's Function via minimizing
    Dirichlet energy, i.e.
5  % least squares method.
6  % Vx and Vy are input vector field components which can
    be either aperiodic
7  % or periodic by setting pbc to be 0 or 1, respectively.
    For non-periodic
8  % application, Vx and Vy have to vanish at the boundary,
    and for periodic
9  % application when div-free potential is zero, Vx(:,1)=
    Vx(:,end+1) which
10 % can be shifted to zero, Vx(1,:)=Vx(end+1,:) which is
    not zero, Vy(1,:) =
11 % Vy(end+1,:) which can be shifted to 0, and Vy(:,1)=Vy
    (:,end+1) which must
12 % not be zero.
13 % x and y are coordinates after meshgrid, default grid
    size is 1.
14 % delta: regulization factor, default value is 1e-6.
15 % num_period: number of period emanating from original
    unit cell, default
16 % value is 5.
17 % pbc: periodic boundary condition is set to 1 by
    default. Thus, to
18 % decompose an aperiodic vector field, pbc needs to be
    0.
19 % phi: curl-free potential, or scalar potential.
20 % psi: div-free potential (only z-component because x
    and y components are
21 % both zero).
22 % curlfree_x/curlfree_y: curl-free components of vector
    fields
23 % divfree_x/divfree_y: divergence-free components of
    vector fields.
24 % hx/hy: harmonic remainder.
25 % [phi, psi, curlfree_x, curlfree_y, divfree_x, divfree_y, hx,

```

```

    hy] = gfm2dhhd(Vx,Vy)
26 % [phi , psi , curlfree_x , curlfree_y , divfree_x , divfree_y , hx ,
    hy] = gfm2dhhd(Vx,Vy,x,y)
27 % [phi , psi , curlfree_x , curlfree_y , divfree_x , divfree_y , hx ,
    hy] = gfm2dhhd(Vx,Vy,x,y,delta)
28 % [phi , psi , curlfree_x , curlfree_y , divfree_x , divfree_y , hx ,
    hy] = gfm2dhhd(Vx,Vy,x,y,delta ,pbc , num_period)
29
30 % -Hui Dong- edited on April 27th, 2014, revised on May
    19, 2014 ,revised January , 2015-
31 % $Version1.3$
32
33 [num_row , num_column] = size(Vx);
34 if ( nargin == 2)
35     x = 1:num_column;
36     y = 1:num_row;
37     [x,y] = meshgrid(x,y);
38     delta = 1e-6;
39     pbc = 1;
40     num_period = 5;
41 elseif ( nargin == 4)
42     delta = 1e-6;
43     pbc = 1;
44     num_period = 5;
45 elseif ( nargin == 5)
46     pbc = 1;
47     num_period = 5;
48 end
49 xgrid = abs(x(1,2)-x(1,1));
50 ygrid = abs(y(2,1)-y(1,1));
51
52 phi = NaN(num_row , num_column);
53 psi = NaN(num_row , num_column);
54 [num_xgrid , num_ygrid] = meshgrid(0:num_column , 0:num_row)
    ;
55 rx = xgrid*num_xgrid;
56 ry = ygrid*num_ygrid;

```

```

57 clear 'num_xgrid' 'num_ygrid'
58 if pbc == 0
59     GFquarter = -1/2/pi*log(sqrt(rx.^2+ry.^2));
        GFquarter(1,1) = -1/2/pi*log(sqrt(delta));
60 else
61     GFquarter = NaN(num_row+1,num_column+1);
62     parpool(6);
63     parfor inum_row = 1:num_row+1
64         for inum_column = 1:num_column+1
65             [xextend,yextend] = meshgrid((num_column
                -1+1)*(-num_period:num_period),(num_row
                -1+1)*(-num_period:num_period));
66             xextend = xgrid*xextend; yextend = ygrid*
                yextend;
67             rx_pb = kron(rx(inum_row,inum_column),ones
                (2*num_period+1))+xextend;
68             ry_pb = kron(ry(inum_row,inum_column),ones
                (2*num_period+1))+yextend;
69             temp = -1/2/pi*log(sqrt((rx_pb).^2+(ry_pb)
                .^2)); temp(temp == inf)=-1/2/pi*log(sqrt
                (delta));
70             GFquarter(inum_row,inum_column) = sum(sum(
                temp));
71         end
72     end
73     clear 'temp' 'xextend' 'yextend' 'rx_pb' 'ry_pb'
74     delete(gcf)
75 end
76 %if Vx is MxN, b = (M-1)*dy, a=(N-1)*dx; GreenF is (2M
    +1)x(2N+1) where one
77 %more row and one more column are extended for correct
    Gradient. xextend
78 %and yextend should be (2*num_period+1)x(2*num_period+1)
    whose xgrid is a
79 %and ygrid is b.
80 GreenF = [rot90(GFquarter,2), flipud(GFquarter); fliplr(
    GFquarter),GFquarter]; GreenF(num_row+1,:) = []; GreenF

```

```

      (: , num_column+1) = [];
81 [dGx_whole , dGy_whole] = gradient (GreenF , xgrid , ygrid);
82 % clear 'GFquarter' 'GreenF'
83
84 parpool(5);
85 parfor_progress(num_column);
86 parfor icolumn = 1:num_column
87     for irow = 1:num_row
88         temp_x = dGx_whole;
89         temp_y = dGy_whole;
90         dGx = temp_x(num_row+2-irow:end-irow , num_column
          +2-icolumn:end-icolumn);
91         dGy = temp_y(num_row+2-irow:end-irow , num_column
          +2-icolumn:end-icolumn);
92         phi(irow , icolumn) = sum(sum(dGx.*Vx+dGy.*Vy))*
          xgrid*ygrid;
93         psi(irow , icolumn) = sum(sum(dGy.*Vx-dGx.*Vy))*
          xgrid*ygrid;
94     end
95     parfor_progress;
96 end
97 parfor_progress(0);
98 delete(gcp)
99 clear 'dGx' 'dGy' 'temp_x' 'temp_y'
100
101 [divfree_x , divfree_y] = gradient(psi , xgrid , ygrid);
102 temp = divfree_x;
103 divfree_x = divfree_y;
104 divfree_y = -temp;
105 [curlfree_x , curlfree_y] = gradient(phi , xgrid , ygrid);
106 hx = Vx-curlfree_x-divfree_x;
107 hy = Vy-curlfree_y-divfree_y;

```

Appendix F

Parallel HHD in C++ using OpenMP and MPI

F.1 Head File

```
1 #include <iostream>
2 #include <fstream>
3 #include <math.h>
4 #include <stdio.h>
5 #include <stdlib.h>
6 #include <iomanip>
7 #include <omp.h>
8 #include <time.h>
9 #include <mpi.h>
10
11 using namespace std;
12 #define VERBOSE 0
13
14 class gf2d{
15     private:
16     int m,n;
17
18     public:
19     long double **gf;
20     int ntds;
21     gf2d(int mm, int nn){
22         //to use MPI, 2D array has to be
23         //contiguous, gf[0] is initialized
24         //gf[i] is set
25         int i;
```

```

25         m = mm; n = nn;
26         if (m%2 == 0 || n%2 == 0)
27         {cout<<"Green's Function must have odd
           rows and odd columns...\n";exit(1);}
28         gf = new long double *[m];
29         gf[0] = new long double [mm*nn];
30         for (i=1; i<m; i++) gf[i]=&gf[0][i*n];
31     }
32
33     void aperiodic(long double ,long double , long
           double);
34     void periodic(long double , long double , int ,
           long double , int);
35     void output(char *);
36
37     ~gf2d() {
38         delete [] gf;
39     }
40 };
41
42 class mtsgdt{
43     private:
44     int m,n;
45
46     public:
47     long double **a, **gdtx_a , **gdty_a;
48     mtsgdt(int mm, int nn){
49         int i;
50         m = mm; n = nn;
51         a = new long double *[m];
52         a[0] = new long double [mm*nn];
53         for (i=1; i<m; i++) a[i] = &a[0][i*n];
54         gdtx_a = new long double *[m];
55         gdtx_a[0] = new long double [mm*nn];
56         for (i=1; i<m; i++) gdtx_a[i] = &gdtx_a
           [0][i*n];
57         gdty_a = new long double *[m];

```

```

58         gdt_y_a[0] = new long double [mm*nn];
59         for (i=1; i<m; i++) gdt_y_a[i] = &gdt_y_a
           [0][i*n];
60     }
61     void input(char *);
62     void gdt(long double, long double, long double **)
           ;
63     void output(char *, char *);
64     ~mtxgdt(){
65         delete [] a;
66         delete [] gdt_x_a;
67         delete [] gdt_y_a;
68     }
69 };
70
71 class mtxsum{
72     private:
73     int m,n;
74
75     public:
76     long double **a, sum;
77     mtxsum(int mm, int nn){
78         int i;
79         m=mm; n=nn;
80         a = new long double *[m];
81         for (i=0; i<m; i++) a[i] = new long
           double [n];
82     }
83     void input(char *);
84     long double sumsum();
85     ~mtxsum(){
86         int i;
87         for (i=0; i<m; i++) {delete [] a[i];}
88         delete [] a;
89     }
90 };
91

```

```

92 class potentials{
93     private:
94     int m,n;
95
96     public:
97     long double **phi, **psi; //potentials.phi and
98     potentials(int mm, int nn){
99         int i;
100        m = mm; n=nn;
101        phi = new long double *[m];
102        phi[0] = new long double [m*n];
103        for (i=1; i<m; i++) phi[i] = &phi[0][i*n
104        ];
105        psi = new long double *[m];
106        psi[0] = new long double [m*n];
107        for (i=1; i<m; i++) psi[i] = &psi[0][i*n
108        ];
109    }
110    void cal_potentials(int , int , int , int , long
111    double , long double , long double **, long
112    double **, long double **, long double **,
113    int);
114    ~potentials(){
115        delete [] phi;
116        delete [] psi;
117    }
118 };

```

F.2 Class File

```

1 #include "gf2dhhd.h"
2
3 //2D Green Function
4 void gf2d::aperiodic(long double dx, long double dy,
5     long double delta){
6     int m_quarter=(m+1)/2;
7     int n_quarter=(n+1)/2;

```

```

7         long double pi = 1/3.141592653589793;
8         int i=0,j=0;
9
10        for (i=0; i<m_quarter; i++){
11            for (j=0; j<n_quarter; j++){
12                if (i==0 && j==0){
13                    gf[m_quarter-1][n_quarter-1] = -0.5*
14                        pi*log(sqrt(delta));
15
16                #if VERBOSE >=1
17                    printf("%f ",gf[
18                        m_quarter-1][
19                            n_quarter-1]);
20                #endif
21            }
22            else { //dy is vertical grid and
23                //applied to rows, while dx is
24                //horizontal grid and applied on
25                //column
26                gf[m_quarter-1+i][n_quarter-1+
27                    j] = -0.5*pi*log(sqrt(pow(i
28                        *dy,2)+pow(j*dx,2)));
29                #if VERBOSE >=1
30                    printf("%f ",gf[m_quarter-1+i
31                        ][n_quarter-1+j]);
32                #endif
33            }
34        }
35    }
36
37    cout<<endl;
38
39    #endif
40
41    for (i=0; i<m_quarter-1; i++){
42        for (j=0; j<n_quarter; j++){
43            gf[i][n_quarter-1+j]=gf[m-1-i][
44                n_quarter-1+j];
45        }
46    }

```

```

34     }
35
36     for (i=0; i<m; i++){
37         for (j=0; j<n_quarter-1; j++){
38             gf[i][j] = gf[i][n-1-j];
39         }
40     }
41 }
42 void gf2d::periodic(long double dx, long double dy, int
    num_period, long double delta, int ntds){
43     if (num_period%2 == 0) {cout<<"Number of period
        has to be odd because period is truncated
        evenly...\n"; exit(1);}
44     long double ax = dx*(0.5*(n-1)); //ax is lattice
        constant along x-direction, n is odd, gf2d
        is 2x2 of unit cell
45     long double ay = dy*(0.5*(m-1));
46     long double *rx_pb = new long double [num_period
        ];
47     for (int i=0; i<num_period; i++) rx_pb[i] = (i-(
        num_period-1)/2)*ax; //-2ax,-ax,0,ax,2ax if
        num_period=5
48     long double *ry_pb = new long double [num_period
        ];
49     for (int i=0; i<num_period; i++) ry_pb[i] = (i-(
        num_period-1)/2)*ay;
50
51     int m_quarter = (m+1)/2;
52     int n_quarter = (n+1)/2;
53     long double pi = 1/3.141592653589793;
54     long double subGF;
55     int i, j;
56     omp_set_num_threads(ntds);
57 #pragma omp parallel num_threads(ntds) default(shared)
        private(subGF, j)
58 #pragma omp for schedule(static)
59     for (i = 0; i<m_quarter; i++){

```

```

60         for (j = 0; j<n_quarter; j++){
61             //gf[m_quarter-1+i][n_quarter-1+j] =
                0.0;
62             //subGF = 0.0;
63             for (int i1 = 0; i1<num_period;
                i1++){
64                 for (int i2=0; i2<
                    num_period; i2++){
65                     subGF = -0.5*pi*
                        log(sqrt(pow(
                            i*dy+ry_pb[i1
                                ],2)+pow(j*dx
                                    +rx_pb[i2],2)
                                        ));
66                     if (isinf(subGF)
                        ) subGF =
                            -0.5*pi*log(
                                sqrt(delta));
67                     gf[m_quarter-1+i
                        ][n_quarter
                            -1+j] +=
                                subGF;
68                 }
69             }
70 #if VERBOSE >=1
                printf("%f ", gf[m_quarter-1+i][
                    n_quarter-1+j]);
71 #endif
72 #endif
73     }
74 #if VERBOSE >=1
                cout<<endl;
75 #endif
76 #endif
77     }
78     delete [] rx_pb;
79     delete [] ry_pb;
80
81 #pragma omp parallel for num_threads(ntds) default(

```

```

    shared) private(j)
82     for (i=0; i<m_quarter-1; i++){
83         for (j=0; j<n_quarter; j++){
84             gf[i][n_quarter-1+j]=gf[m-1-i][
                n_quarter-1+j];
85         }
86     }
87 #pragma omp parallel for num_threads(ntds) default(
    shared) private(j)
88     for (i=0; i<m; i++){
89         for (j=0; j<n_quarter-1; j++){
90             gf[i][j] = gf[i][n-1-j];
91         }
92     }
93 }
94 }
95 void gf2d::output(char *str1){
96     int i,j;
97     ofstream fout(str1);
98     if (!str1)
99         {cout<<"Cannot create the file "<<str1<<endl;
            exit(1);}
100 #if VERBOSE >=1
101     cout<<"Green's Function is:\n";
102 #endif
103     for (i=0; i<m; i++){
104         for (j=0; j<n; j++){
105             fout<<" "<<std::setprecision(16)<<gf[i][
                j];
106 #if VERBOSE >=1
107             cout<<" "<<gf[i][j];
108 #endif
109         }
110         fout<<endl;
111 #if VERBOSE >=1
112         cout<<endl;
113 #endif

```

```

114         }
115         fout.close();
116     }
117
118
119     //Find Gradient of 2D matrix
120     void mtsgdt::input(char *str1){
121         int i,j;
122         ifstream fin(str1);
123         if (!fin)
124             {cout<<"Input identity "<<str1<<" doesn't
125              exist—mtsgdt.c\n"; exit(1);}
126         for (i=0; i<m; i++){
127             for (j=0; j<n; j++)
128                 fin>>a[i][j];
129         }
130         fin.close();
131     #if VERBOSE >= 1
132         for (i=0; i<m; i++){
133             for (j=0; j<n; j++)
134                 cout<<a[i][j]<<" ";
135             cout<<endl;
136         }
137     #endif
138     }
139     void mtsgdt::gdt(long double dx, long double dy, long
140                     double **a){
141         int i,j;
142
143         for (i=0; i<m; i++){
144             for (j=1; j<n-1; j++){
145                 gdtx_a[i][j] = 0.0;
146                 gdtx_a[i][j] = 0.5*(a[i][j+1]-a[
147                     i][j-1])/dx;
148             }
149             gdtx_a[i][0] = 0.0;
150             gdtx_a[i][0]=(a[i][1]-a[i][0])/dx;

```

```

148             gdtx_a[i][n-1] = 0.0;
149             gdtx_a[i][n-1]=(a[i][n-1]-a[i][n-2])/dx;
150         }
151     #if VERBOSE >= 1
152         for (i=0; i<m; i++){
153             for (j=0; j<n; j++)
154                 cout<<gdtx_a[i][j]<<" ";
155             cout<<endl;
156         }
157     #endif
158
159     for (j=0; j<n; j++){
160         for (i=1; i<m-1; i++){
161             gdty_a[i][j] = 0.0;
162             gdty_a[i][j] = 0.5*(a[i+1][j]-a[
163                 i-1][j])/dy;
164         }
165         gdtx_a[0][j] = 0.0;
166         gdtx_a[0][j] = (a[1][j]-a[0][j])/dy;
167         gdtx_a[m-1][j] = 0.0;
168         gdtx_a[m-1][j] = (a[m-1][j]-a[m-2][j])/
169             dy;
170     }
171     #if VERBOSE >= 1
172         for (i=0; i<m; i++){
173             for (j=0; j<n; j++)
174                 cout<<gdty_a[i][j]<<" ";
175             cout<<endl;
176         }
177     #endif
178 }
179 void mtngxdt::output(char *str2 ,char *str3){
180     int i,j;
181     ofstream foutx(str2);
182     if (!str2)
183         {cout<<"Cannot open the file"<<str2<<endl;exit
184             (1);}

```

```

182 #if VERBOSE >= 1
183     cout<<" Gradient x-component is:\n";
184 #endif
185     for (i=0; i<m; i++){
186         for (j=0; j<n; j++){
187             foutx<<" " <<std::setprecision
                (16)<<gdtx_a[i][j];
188 #if VERBOSE >= 1
189                 cout<<" " <<gdtx_a[i][j];
190 #endif
191             }
192             foutx<<endl;
193 #if VERBOSE >= 1
194             cout<<endl;
195 #endif
196         }
197         foutx.close();
198
199         ofstream fouty(str3);
200         if (!str3)
201             {cout<<" Cannot open the file" <<str3<<endl; exit
                (1);}
202 #if VERBOSE >= 1
203             cout<<" Gradient y-component is:\n";
204 #endif
205             for (i=0; i<m; i++){
206                 for (j=0; j<n; j++){
207                     fouty<<" " <<std::setprecision
                        (16)<<gdty_a[i][j];
208 #if VERBOSE >= 1
209                         cout<<" " <<gdty_a[i][j];
210 #endif
211                 }
212                 fouty<<endl;
213 #if VERBOSE >= 1
214                 cout<<endl;
215 #endif

```

```

216         }
217         fouty.close();
218     }
219
220
221     //Find Sum of 2D Matrix, This class is not necessary
222     void mtxsum::input(char *str1){
223         int i,j;
224         ifstream fin(str1);
225         if (!fin)
226             {cout<<"Input matrix "<<str1<<" doesn't exist—
                mtxsum.c/n";exit(1);}
227         for (i=0; i<m; i++){
228             for (j=0; j<n; j++)
229                 fin>>a[i][j];
230         }
231         fin.close();
232
233         #if VERBOSE >= 1
234             for (i=0; i<m; i++){
235                 for (j=0; j<n; j++)
236                     cout<<a[i][j]<<" ";
237                 cout<<endl;
238             }
239         #endif
240     }
241     long double mtxsum::sumsum(){
242         int i,j;
243         sum = 0.0;
244         for (i=0; i<m; i++){
245             for (j=0; j<n; j++)
246                 sum += a[i][j];
247         }
248         #if VERBOSE >= 1
249             cout<<sum<<endl;
250         #endif
251         return sum;

```

```

252 }
253
254
255 //Calculate the Potentials, MPI to split irow
256 void potentials::cal_potentials(int rowstart, int rowend
    , int mglobal, int nglobal, long double dx, long
    double dy, long double **Vx, long double **Vy, long
    double **dGx, long double **dGy, int ntds){
257
258     omp_set_num_threads(ntds);
259 #pragma omp parallel for num_threads(ntds)
260     for(int irow=rowstart; irow<=rowend; irow++){
261         for (int icolumn=0; icolumn<nglobal;
            icolumn++){
262             long double sumphi = 0.0, sumpsi
                = 0.0;
263             for (int i=0; i<mglobal; i++){
264                 for(int j=0; j<nglobal;
                    j++){
265                     sumphi += Vx[i][
                        j]*dGx[
                            mglobal-irow+
                                i][nglobal-
                                    icolumn+j]+Vy
                                        [i][j]*dGy[
                                            mglobal-irow+
                                                i][nglobal-
                                                    icolumn+j];
266                     sumpsi += Vx[i][
                        j]*dGy[
                            mglobal-irow+
                                i][nglobal-
                                    icolumn+j]-Vy
                                        [i][j]*dGx[
                                            mglobal-irow+
                                                i][nglobal-
                                                    icolumn+j];

```

```

267         }
268     }
269     phi[irow-rowstart][icolumn] =
        sumphi*dx*dy;
270     psi[irow-rowstart][icolumn] =
        sumpsi*dx*dy;
271     }
272 }
273 }

```

F.3 Main File

```

1 #include "gf2dhhd.h"
2 //COMPILE: mpicxx gf2dhhd.c gf2dhhd_main.c -o
   gf2dhhd_main -std=c99 -openmp -lrt -wd981
3
4 int main(int argc, char **argv){
5
6     MPI_Status status;
7     MPI_File file_phi; //MPI-IO to the same output
   file
8     MPI_File file_psi;
9     MPI_Datatype local_phi; //Create subarray
10    MPI_Datatype local_psi;
11    char procname[32]; //store processor's name
12    int ierr; ierr = MPI_Init(&argc,&argv);
13    int mpirank; ierr |= MPI_Comm_rank(
   MPLCOMM_WORLD, &mpirank);
14    int mpisize; ierr |= MPI_Comm_size(
   MPLCOMM_WORLD, &mpisize);
15    int namelen; MPI_Get_processor_name(procname, &
   namelen);
16
17    char *str1 = "Vx.dat";
18    char *str2 = "Vy.dat";
19    const int m=99,n=70; //Change!
20    const long double delta = 4.832930238571752e-09;
21    int num_period = (argc ==3)? atoi(argv[2]):20;

```

```

22     long double width = 1.0, height=1.4;
23     long double dx = width/n, dy = height/m; //
        changed, Note Vx and Vy are deleted 1 row and
        1 column
24
25     //Divide rows onto different processes
26     const int root = 0;
27     int local_mlen = m/mpisize; //4 proc, 105/4 = 26
28     int rowstart = mpirank*local_mlen; //
        0-25;26-51,...
29     int rowend = (mpirank+1)*local_mlen -1;
30     if (mpirank == mpisize -1){ //78-105
31         rowend = m-1; local_mlen = rowend-
            rowstart+1;
32     }
33
34     //To use MPI_Bcast, these 4 arrays are
        contiguous
35     long double **Vx, **Vy;
36     long double **dGx, **dGy;
37     Vx = new long double *[m]; Vy = new long double
        *[m];
38     Vx[0] = new long double [m*n]; Vy[0] = new long
        double [m*n];
39     for (int i=1; i<m; i++){
40         Vx[i] = &Vx[0][i*n];
41         Vy[i] = &Vy[0][i*n];
42     }
43     dGx = new long double *[2*m+1]; dGy = new long
        double *[2*m+1];
44     dGx[0] = new long double [(2*m+1)*(2*n+1)];
45     dGy[0] = new long double [(2*m+1)*(2*n+1)];
46     for (int i=1; i<2*m+1; i++){
47         dGx[i] = &dGx[0][i*(2*n+1)];
48         dGy[i] = &dGy[0][i*(2*n+1)];
49     }
50

```

```

51     int ntds = (argc == 2)? atoi(argv[1]):6; //
        OpenMP threads number
52     struct timespec tcgstart = {0,0}; //time of
        constructing GF
53     struct timespec tcgend = {0,0};
54     struct timespec tgdstart = {0,0}; //time of
        finding gradient
55     struct timespec tgdend = {0,0};
56     struct timespec tpstart = {0,0}; //time of
        finding potential
57     struct timespec tpend = {0,0};
58
59     //Vx and Vy can be read from the same file by
        different processors
60     if (mpirank == 0) {
61
62         //read force field into memory
63         ifstream Vxin(str1);
64         if (!Vxin) {cout<<"Input file Vx does
            not exist!\n"; exit(1);}
65         for (int i=0; i<m; i++){
66             for (int j=0; j<n; j++){
67                 Vxin>>Vx[i][j];
68             }
69         }
70         Vxin.close();
71         ifstream Vyin(str2);
72         if (!Vyin) {cout<<"Input file Vy does not
            exist!\n"; exit(1);}
73         for (int i=0; i<m; i++){
74             for (int j=0; j<n; j++){
75                 Vyin>>Vy[i][j];
76             }
77         }
78         Vyin.close();
79
80         //Build 2x larger Green Function, use

```

```

81         OpenMP
82         gf2d GreenF(2*m+1,2*n+1);
83         clock_gettime(CLOCK_REALTIME,&tcgstart);
84         GreenF.periodic(dx,dy,2*num_period+1,
85             delta,ntds); //if small, OpenMP, if
86             large OpenMP+MPI (Will See)
87         clock_gettime(CLOCK_REALTIME,&tcgend);
88         cout<<"Time of building Green's Function
89             is " <<(tcgend.tv_sec-tcgstart.tv_sec
90             )*1000+(tcgend.tv_nsec-tcgstart.
91             tv_nsec)/1000000<<"ms\n";
92 #if VERBOSE >=1
93     GreenF.output("GreenF100.dat");
94 #endif
95 //Find Gradient of Green's Function, not
96 //time-consuming, no need to
97 //parallelize
98 mtxgdt GF(2*m+1,2*n+1);
99 #if VERBOSE >=1
100 GF.input("GreenF100.dat");
101 #endif
102         clock_gettime(CLOCK_REALTIME,&tgdstart)
103         ;
104         GF.gdt(dx,dy,GreenF.gf); //OpenMP
105         clock_gettime(CLOCK_REALTIME,&tgdend);
106         cout<<"Time of finding the gradient is "
107             <<(tgdend.tv_sec-tgdstart.tv_sec)
108             *1000+(tgdend.tv_nsec-tgdstart.
109             tv_nsec)/1000000<<"ms\n";
110 #if VERBOSE >=1
111     GF.output("dGx100.dat", "dGy100.dat");
112 #endif
113 //Read dGx.dat and dGy.dat into dGx and
114 //dGy
115 for (int i=0; i<2*m+1; i++) dGx[i] = &GF
116     .gdtx_a[0][i*(2*n+1)];
117 for (int i=0; i<2*m+1; i++) dGy[i] = &GF

```

```

104         .gdy_a [0][ i*(2*n+1)];
        cout<<"Master's Rank which is "<<mpirank
        <<"; and name is "<<procname<<" has
        finished calculating Vx, Vy, dGx, and
        dGy!"<<endl;
105     }
106 //
        //////////////////////////////////////
107
108     //Now we have Vx, Vy, dGx, dGy, they should be
        broadcasted to every process
109     MPI_Bcast(&Vx[0][0], m*n, MPLLONG.DOUBLE, root,
        MPLCOMM_WORLD);
110     MPI_Bcast(&Vy[0][0], m*n, MPLLONG.DOUBLE, root,
        MPLCOMM_WORLD);
111     MPI_Bcast(&dGx[0][0], (2*m+1)*(2*n+1),
        MPLLONG.DOUBLE, root, MPLCOMM_WORLD);
112     MPI_Bcast(&dGy[0][0], (2*m+1)*(2*n+1),
        MPLLONG.DOUBLE, root, MPLCOMM_WORLD);
113
114     //This part is the most time consuming part, no
        need for barrier
115     potentials ptl(local_mlen, n);
116     clock_gettime(CLOCK_REALTIME, &tpstart);
117     ptl.cal_potentials(rowstart, rowend, m, n, dx,
        dy, Vx, Vy, dGx, dGy, ntds);
118     clock_gettime(CLOCK_REALTIME, &tpend);
119     MPI_Barrier(MPLCOMM_WORLD); //not necessary,
        just want to see print screen
120     fflush(stdout);
121     cout<<"The rank "<<mpirank<<" whose name is "<<
        procname<<" calculates rows from "<<rowstart
        <<" to "<<rowend<<";"<<endl;
122     cout<<"\tTime of finding the potential is "<<(
        tpend.tv_sec-tpstart.tv_sec)*1000+(tpend.
        tv_nsec-tpstart.tv_nsec)/1000000<<"ms\n";

```

```

123
124 //Different processes write to the same "phi.txt
    " and "psi.txt" simultaneously—LAST PROBLEM
125 //Create char datatype
126 char phi_file[30], psi_file[30];
127 sprintf(phi_file, "phi_p%d.dat", num_period);
128 sprintf(psi_file, "psi_p%d.dat", num_period);
129 MPI_Datatype phi_as_string;
130 const int charspernum = sizeof(long double)+8;
131 MPI_Type_contiguous(charspernum, MPI_CHAR, &
    phi_as_string);
132 MPI_Type_commit(&phi_as_string);
133 char *phi_as_txt = new char [local_mlen*n*
    charspernum];
134 int count = 0;
135 for (int i=0; i<local_mlen; i++){
136     for (int j=0; j<n-1; j++){
137         sprintf(&phi_as_txt[count*
            charspernum], "%1.15Le ", ptl
            .phi[i][j]);
138         count++;
139     }
140     sprintf(&phi_as_txt[count*charspernum],
        "%1.15Le\n", ptl.phi[i][n-1]);
141     count++;
142 }
143
144 MPI_Datatype psi_as_string;
145 MPI_Type_contiguous(charspernum, MPI_CHAR, &
    psi_as_string);
146 MPI_Type_commit(&psi_as_string);
147 char *psi_as_txt = new char [local_mlen*n*
    charspernum];
148 count = 0;
149 for (int i=0; i<local_mlen; i++){
150     for (int j=0; j<n-1; j++){
151         sprintf(&psi_as_txt[count*

```

```

152         charspnum], "%1.15Le ", ptl
153         .psi[i][j]);
154         count++;
155     }
156     sprintf(&psi_as_txt[count*charspnum],
157             "%1.15Le\n", ptl.psi[i][n-1]);
158     count++;
159 }
160
161 //Create subarray
162 int globalsizes[2] = {m,n};
163 int localsizes[2] = {local_mlen,n};
164 int starts[2] = {rowstart, 0};
165 int order = MPIORDER_C;
166 MPI_Type_create_subarray(2, globalsizes,
167     localsizes, starts, order, phi_as_string, &
168     local_phi);
169 MPI_Type_commit(&local_phi);
170 MPI_Type_create_subarray(2, globalsizes,
171     localsizes, starts, order, psi_as_string, &
172     local_psi);
173 MPI_Type_commit(&local_psi);
174
175 MPI_File_open(MPLCOMM_WORLD, phi_file,
176     MPI_MODE_CREATE|
177     MPI_MODE_WRONLY, //
178     WRONLY: Write only
179     MPI_INFO_NULL, &
180     file_phi);
181 MPI_File_set_view(file_phi, 0, MPLCHAR,
182     local_phi, "native", MPI_INFO_NULL);
183 MPI_File_write_all(file_phi, phi_as_txt,
184     local_mlen*n, phi_as_string, &status);
185 MPI_File_close(&file_phi);
186
187 MPI_File_open(MPLCOMM_WORLD, psi_file,
188     MPI_MODE_CREATE|

```


Bibliography

- [1] G. Agrawal. *Nonlinear Fiber Optics*. Academic Press, 2006.
- [2] M.H. Anderson, J.R. Ensher, M.R. Matthews, C.E. Wieman, and Cornell E.A. Observation of bose-einstein condensation in a dilute atomic vapor. *Science*, 269(5221):198–201, 1995.
- [3] X. Ao, Z. Lin, and C.T. Chan. One-way edge mode in a magneto-optical honeycomb photonic crystal. *Phys. Rev. B*, 80:033105, 2009.
- [4] A. Ashkin. Acceleration and trapping of particles by radiation pressure. *Phys. Rev. Lett.*, 1970.
- [5] M. Barozzi and A. Vannucci. Performance characterization and guidelines for the design of a counter-propagating nonlinear lossless polarizer. *J. Opt. Soc. Am. B*, 30(12):3102, 2013.
- [6] E.B. Becker, G.F. Carey, and J.T. Oden. *Finite elements: An introduction*, volume 1. Prentice Hall, INC, 1981.
- [7] R. Boyd. *Nonlinear Optics*. Academic Press, 2009.
- [8] H. Bruus. *Theoretical Microfluidic*. Oxford University Press, 2008.
- [9] Henrik Bruus. Acoustofluidics 7: The acoustic radiation force on small particles. *Lab on a Chip*, 12(6):1014, 2012.

- [10] Y. Cao, L. Chen, W. Ding, F. Sun, and T. Zhu. Optical collection of multiple spheres in single tightly focused beams. *Opt. Commun.*, 311:332–337, 2013.
- [11] S.A. Chandorkar, R.N. Candler, A. Duwel, R. Melamud, M. Agarwal, K.E. Goodson, and T.W. Kenny. Multimode thermoelastic dissipation. *J. Appl. Phys.*, 105:043505, 2009.
- [12] R.Y. Chiao, C.H. Townes, and B.P. Stoicheff. Stimulated brillouin scattering and coherent generation of intense hypersonic waves. *Phys. Rev. Lett.*, 12:592–595, 1964.
- [13] S. Chu, J.E. Bjorkholm, A. Ashkin, and A. Cable. Demonstration of laser cooling and trapping of atoms. *Atomic Physics*, pages 377–393, 1987.
- [14] Nima Dabidian, Shourya Dutta-Gupta, Iskandar Kholmanov, Kueifu Lai, Feng Lu, Jongwon Lee, Mingzhou Jin, Simeon Trendafilov, Alexander Khanikaev, Babak Fallahazad, Emanuel Tutuc, Mikhail A. Belkin, and Gennady Shvets. Experimental demonstration of phase modulation and motion sensing using graphene-integrated metasurfaces. *Nano Letters*, 16(6):3607–3615, 2016.
- [15] P. Dainese, P. Russell, N. Joly, J. Knight, G. Wiederhecker, H. Fragnito, V. Laude, and A. Khelif. Stimulated brillouin scattering from multi-ghz-guided acoustic phonons in nanostructured photonic crystal fibres. *Nature Phys.*, 2:388–392, 2006.

- [16] J. Fatome. A universal optical all-fiber omnipolarizer. *Sci. Rep.*, 2, 2012.
- [17] C. Fietz, Y. Urzhumov, and G. Shvets. Complex k band diagrams of 3d metamaterial/photonic crystals. *Optics Express*, 19(20):19207–19041, 2011.
- [18] P. et al Glynne-Jones. Efficient finite element modeling of radiation forces on elastic particles of arbitrary size and geometry. *J. Acoust. Soc. Am.*, 4:133, 2013.
- [19] J.P. Gordon. Radiation forces and momenta in dielectric media. *Phys. Rev. A*, 8:14–21, 1973.
- [20] D.J. Griffiths. *Introduction to Eelectrodynamics*. Benjamin Cummings Inc, 2008.
- [21] D. Haefner, S. Sukhov, and Dogarium A. Conservative and nonconservative torques in optical binding. *Phys. Rev. Lett.*, 103(17):173602, 2009.
- [22] H.-Y. Hao and H. Maris. Dispersion of the long-wavelength phonons in ge, si, gaas, quartz, and sapphire. *Phys. Rev. B*, 63:224301, 2001.
- [23] H.A. Haus. *Waves and fields in optoelectronics*. Prentice Hall, 1984.
- [24] H.O. Hill, B.S. Kawasaki, and D.C. Johnson. Cw brillouin laser. *Appl. Phys. Lett.*, 28:608–609, 1976.

- [25] L. S. Hounsome, R. Jones, M. J. Shaw, and P. R. Briddon. Photoelastic constants in diamond and silicon. *physica status solidi A*, 203:3088–3093, 2006.
- [26] J.D. Joannopoulos. Photonics: Self-assembly light up. *nature*, 414(6861):257–258, 2001.
- [27] S.G. Johnson, M. Ibanescu, M.A. Skorobogatiy, O. Weisberg, J. D. Joannopoulos, and Y. Fink. Perturbation theory for maxwell’s equations with shifting material boundaries. *Phys.Rev.E*, 65:066611, 2002.
- [28] I.V. Kabakova, R. Pant, D. Choi, S. Debbarma, B. Luther-Davies, Mad-den S.J., and B.J. Eggleton. Narrow linewidth brillouin laser based on chalcogenide photonic chip. *Opt. Lett.*, 38:3208–3211, 2013.
- [29] M.S. Kang, A. Butsch, and P.S.J. Russell. Reconfigurable light-driven opto-acoustic isolator in photonic crystal fibre. *Nat. Photonics*, 5:549–553, 2011.
- [30] M.S. Kang, A. Nazarkin, Brenn A., and P.S.J. Russell. Tightly trapped acoustic phonons in photonic crystal fibres ad highly nonlinear artificial raman oscillations. *Nat. Phys.*, 5:276–280, 2009.
- [31] W. Ketterle, K.B. Davis, M.A. Joffe, Martin A., and D.E. Pritchard. High densities of cold atoms in a dark spontaneous-force optical trap. *Phys. Rev. Lett.*, 70(15):2253, 1993.

- [32] A. Kobayakov, M. Sauer, and D. Chowdhury. Stimulated brillouin scattering in optical fibers. *Adv. Opt. Photonics*, 2:1–59, 2010.
- [33] G.L. Li, X.L. Yang, F. Bai, and W.Q. Huang. Raspberry-like composite polymer particles by self-assemble heterocoagulation based on a charge compensation process. *J. Colloid Interf. Sci.*, 297:705–710, 2006.
- [34] H.Y. Li, W.B. Chen, and I.F. Shen. Segmentation of discrete vector fields. *IEEE Trans. Vis. Comput. Graph.*, 12(3):289–300, 2006.
- [35] M. Li, H.P. Pernice, C. Xiong, T. Baehr-Jones, M. Hochberg, and H.X. Tang. Harnessing optical forces in integrated photonic circuits. *Nature*, 456(7221):480–484, 2008.
- [36] R. Li, Yang X.L., G.L. Li, S.N. Li, and W.Q. Huang. Core-corona polymer composite particles by self-assembled heterocoagulation based on a hydrogen-bonding interaction. *Langmuir*, 22:8127–8133, 2006.
- [37] Feng Lu, Mingzhou Jin, and Mikhail A. Belkin. Tip-enhanced infrared nanospectroscopy via molecular expansion force detection. *Nature Photonics*, 8:307, 2014.
- [38] M. Maldovan and E.L. Thomas. Periodic structures and interference lithography. *Periodic Materials and Interference Lithography*, pages 97–112, 2008.

- [39] T.C. Merkel, V.I. Bondar, K. Nagal, B.D. Freeman, and I. Pinnau. Gas sorption, diffusion and permeation in poly(dimethylsiloxane). *J. Polym. Sci. Part B: Polym. Phys.*, 38:415–434, 2008.
- [40] P.W. Milonni and Boyd R.W. Momentum of light in a dielectric medium. *Adv. Opt. Photonics*, 2:519–553, 2010.
- [41] C.J. Myers, M. Celebrano, and M. Krishnan. Information storage and retrieval in a single levitating colloidal particle. *Nat. Nanotechnol.*, 10(10):886–891, 2015.
- [42] S. Noda. Full three-dimensional photonic bandgap crystals at near-infrared wavelengths. *Science*, 289(5479):604–606, 2000.
- [43] D.Y. Oh, S.H. Kim, J. Huang, A. Scofield, D. Huffaker, and A. Scherer. Self-aligned active quantum nanostructures in photonic crystals via selective wet-chemical etching. *Nanotechnology*, 24(26):265201, 2013.
- [44] Y. Okawachi, M.S. Bigelow, J.E. Sharping, Z. Zhu, A. Schweinsberg, D.J. Gauthier, and R.W. Boyd. Tunable all-optical delays via brillouin slow light in an optical fiber. *Phys. Rev. Lett.*, 94:153902, 2005.
- [45] R.H. Ottewill, A.B. Schofield, J.A. Waters, and N.S.J. Williams. Preparation of core-shell polymer colloid particles by encapsulation. *Colloid. Polym. Sci.*, 275:274–283, 1997.

- [46] R. Pant, A. Byrnes, Poulton C.G., E. Li, D. Choi, S. Madden, B. Luther-Davies, and B.J. Eggleton. Photonic chip-based tunable slow and fast light via stimulated brillouin scattering. *Opt. Lett.*, 37:969–971, 2012.
- [47] R. Pant, C.G. Poulton, D.Y. Choi, H. Mcfarlane, S. Hile, E. Li, L. Thevenaz, B. Luther-Davies, S.J. Maden, and B.J. Eggleton. On-chip stimulated brillouin scattering. *Opt. Express*, 19:8285–8290, 2011.
- [48] R. Pant, M.D. Stenner, M.A. Neifeld, and D.J. Gauthier. Optimal pump profile designs for broadband sbs slow-light systems. *Opt. Express*, 16:2764–2777, 2008.
- [49] O. Parriaux, A.V. Tishchenko, and F. Pigeon. *Associating a lossless polarizing function in multilayer laser mirrors by means of resonant grating*, page 61870, 2006.
- [50] C.G. Poulton, R. Pant, A. Byrnes, S. Fan, M.J. Steel, and B.J. Eggleton. Design for broadband on-chip isolator using stimulated brillouin scattering in dispersion-engineered chalcogenide waveguides. *Opt. Express*, 20:21235–21246, 2012.
- [51] M. Povinelli, M. Loncar, M. Ibanescu, E. Smythe, S. Johnson, F. Caposso, and J. Joannopoulos. Evanescent wave bonding between optical waveguides. *Opt. Lett.*, 30:3042, 2005.
- [52] M.L. Povinelli. Evanescent-wave bonding between optical waveguides. *Opt. Lett.*, 30(22):3042–3044, 2005.

- [53] M. Povinelli et al. High-q enhancement of attractive and repulsive optical forces between coupled whispering-gallery-mode resonators. *Opt. Express*, 13(20):8286–8295, 2005.
- [54] W. Qiu, P. Rakich, M. Soljacic, and Z. Wang. Stimulated brillouin scattering in slow light waveguides. page 1210.0738, 2012.
- [55] W. Qiu, P.T. Rakich, H. Shin, **Dong, H.**, M. Soljacic, and Z. Wang. Stimulated brillouin scattering in nanoscale silicon step-index waveguides: a general framework of selection rules and calculating sbs gain. *Optics Express*, 21(25):31402–31419, 2013.
- [56] W. Qiu, P.T. Rakich, H. Shin, **Dong, H.**, M. Soljačić, and Z. Wang. Stimulated brillouin scattering in nanoscale silicon step-index waveguides: a general framework of selection rules and calculating sbs gain. *Opt. Express*, 21:31402, 2013.
- [57] P. Rakich, Davids P., and Z. Wang. Tailoring optical forces in waveguides through radiation pressure and electrostrictive forces. *Opt. Express*, 18:14439, 2010.
- [58] P. Rakich, Z. Wang, and P. Davids. Scaling of optical forces in dielectric waveguides: Rigorous connection between radiation pressure and dispersion. *Opt. Lett.*, 36:217, 2011.
- [59] P.T. Rakich, J.A. Cox, H. Shin, Z. Wang, H. Mousavi, **Dong, H.**, R. Jarecki, A. Siddiqui, and R. C. Potter. Traveling-wave photon-phonon coupling

as the basis for new signal processing technologies. *Proceedings of SPIE*, 9083, 2014.

- [60] P.T. Rakich, J.A. Cox, H. Shin, Z. Wang, H. Mousavi, **Dong, H.**, R. Jarecki, A. Siddiqui, and R.C. Potter. Traveling-wave photon-phonon coupling as the basis for new signal processing technologies. In *Micro- and Nanotechnology Sensors, Systems, and Applications VI*. Proc. of SPIE, 2014.
- [61] P.T. Rakich, M.A. Popovic, and Z. Wang. General treatment of optical forces and potentials in mechanically variable photonic systems. *Opt. Express*, 17(20):18116, 2009.
- [62] P.T. Rakich, C. Reinke, R. Camacho, P. Davids, and Z. Wang. Giant enhancement of stimulated brillouin scattering in the subwavelength limit. *Phys. Rev. X*, 2:011008, 2012.
- [63] Y. Roichman, B. Sun, Y. Roichman, J. Amato-Grill, and D.G. Grier. Optical forces arising from phase gradients. *Phys. Rev. Lett.*, 100(1):13602, 2008.
- [64] Y. Roichman, B. Sun, A. Stolarski, and D.G. Grier. Influence of nonconservative optical forces and dynamics of optically trapped colloidal sphere: the fountain of probability. *Phys. Rev. Lett.*, 101(12):128301, 2008.
- [65] J. Rosenberg, Q. Lin, and O. Painter. Static and dynamic wavelength routing via the gradient optical force. *Nat. Photonics*, 3(8):478–483, 2009.

- [66] D. Royer and E. Dieulesaint. *Elastic Waves in Solids I: Free and Guided Propagation*. Springer, 2000.
- [67] D. Royer and E. Dieulesaint. *Elastic Waves in Solids II: Generation, Acousto-optic Interaction, Applications*. Springer, 2000.
- [68] M. Settnes and H. Bruus. Forces acting on a small particle in an acoustical field in a viscous fluid. *Phys. Rev. E.*, 85:016327, 2012.
- [69] H. Shin, W. Qiu, R. Jarecki, J.A. Cox, R.H. Olsson III, Starbuck A., Z. Wang, and P.T. Rakich. Tailorable stimulated brillouin scattering in nanoscale silicon waveguides. *Nat. Commun.*, 4:1944, 2013.
- [70] S. Shoji and S. Kawata. Photofabrication of three-dimensional photonic crystals by multibeam laser interference into a photopolymerizable resin. *Appl. Phys. Lett.*, 76(19):2668, 2000.
- [71] S.H. Simpson and S. Hanna. First-order nonconservative motion of optically trapped nonspherical particles. *Phys. Rev. E*, 82(3):31141, 2010.
- [72] K.Y. Song, K.S. Abedin, K. Hotate, M.G. Herráez, and L. Thévenaz. Highly efficient brillouin slow and fast light using as₂se₃ chalcogenide fiber. *Opt. Express*, 14:5860–5865, 2008.
- [73] K.Y. Song, M. Herráez, and L. Thévenaz. Observation of pulse delaying and advancement in optical fibers using stimulated brillouin scattering. *Opt. Express*, 13:82–88, 2005.

- [74] W. Suh, Z. Wang, and S. Fan. Temporal coupled-mode theory and the presence of non-orthogonal modes in lossless multimode cavities. *IEEE J. Quantum Electron*, 40(10):1511–1518, 2004.
- [75] B. Sun, J. Lin, E. Darby, A.Y. Grosberg, and D.G. Grier. Brownian vortices. *Phys. Rev. E*, 80(1):10401, 2009.
- [76] F. Svedberg, Z. Li, H. Xu, and M. Kall. Creating hot nanoparticle pairs for surface-enhanced raman spectroscopy through optical manipulation. *Nano Lett.*, 6(12):2639–2641, 2006.
- [77] M. Tomes and T. Carmon. Photonic micro-electromechanical systems vibrating at xband (11-ghz) rates. *Phys. Rev. Lett.*, 102:113601, 2009.
- [78] Alf J. van der Poorten. Some problems of recurrent interest. Technical Report 81-0037, School of Mathematics and Physics, Macquarie University, North Ryde, Australia 2113, August 1981.
- [79] R. Van Laer, D. Van Thourhout, and R. Baets. Strong stimulated brillouin scattering in an on-chip silicon slot waveguide. In *CLEO: Science and Innovations*, San Jose, CA, 9-14 June, 2013.
- [80] Y.A. Vlasov, X.Z. Bo, J.C. Sturm, and D.J. Norris. On-chip natural assembly of silicon photonic bandgap crystals. *Nature*, 414(6861):289–293, 2001.

- [81] K.X. Wang, Z. Yu, S. Sandhu, and S. Fan. Fundamental bounds on decay rates in asymmetric single-mode optical resonators. *Opt. Lett.*, 38(2):100–102, 2013.
- [82] Z. Wang, W. Qiu, P. Rakich, H. Shin, and **Dong, H.** Slow light through tightly coupled light waves and acoustic waves in nanoscale waveguides. *Advances in Slow and Fast Light VI*, 8636:863607, 2013.
- [83] Z. Wang, W. Qiu, P.T. Rakich, H. Shin, and **Dong, H.** Slow light through tightly-coupled light waves and acoustic waves in nanoscale waveguides. In *Advances in Slow and Fast Light VI*. Proc. of SPIE, 2013.
- [84] Z. Wang and P. Rakich. Response theory of optical forces in two-port photonics system: a simplified framework for examining conservative and non-conservative forces. *Opt. Express*, 19(22):22322–22336, 2011.
- [85] M.M. Wang et al. Microfluidic sorting of mammalian cells by optical force switching. *Nat. Biotechnol.*, 23(1):83–87, 2005.
- [86] J.N. Winn, Y. Fink, S. Fan, and J.D. Joannopoulos. Omnidirectional reflection from a one-dimensional photonic crystal. *Opt. Lett.*, 23(20):1573–1575, 1998.
- [87] J.Z. Wu, H.Y. Ma, and M.D. Zhou. *Vorticity and vortex dynamics*. New York:Springer, 2006.

- [88] P. Wu, R. Huang, C. Tischer, A. Jonas, and E.-L. Florin. Direct measurement of the nonconservative force field generated by optical tweezers. *Phys. Rev. Lett.*, 103(10):108101, 2009.
- [89] T. Wu et al. A photon-driven micromotor can direct nerve fibre growth. *Nat. Photonics*, 6(1):62–67, 2011.
- [90] H. Xu and M. Kall. Surface-plasmon-enhanced optical forces in silver nanoaggregates. *Phys. Rev. Lett.*, 89(24), 2002.
- [91] Zongwei Xu, Fengzhou Fang, and Zhen Yin. A review on colloidal self-assembly and their applications. *Current Nanoscience*, 12:725–746, 2016.
- [92] Z. Yu and S. Fan. Complete optical isolation created by indirect inter-band photonic transitions. *Nat. Photonics*, 3:91–94, 2009.
- [93] R. Zhang, M. Gu, X.L. Liu, and K. Hart. The investigation on the charge compensation and luminescent mechanism of rare earth luminescent material y2-x-yeuliyoa. *Mater. Sci. Tech. Equip.*, 5(4):43–45, 2008.
- [94] L. Zheng, **Dong, H.**, X.Y. Wu, Y.L. Huang, W.B. Wang, W.D. Wu, Z. Wang, and K.J. Lai. Interferometric imaging of nonlocal electromechanical power transduction in ferroelectric domains. *Proceedings of the National Academy of Sciences*, 2018.
- [95] Z. Zhu, D.J. Gauthier, and R.W. Boyd. Stored light in an optical fiber via stimulated brillouin scattering. *Science*, 318(5857):1748–1750, 2007.

Vita

Hui Dong was born in Liaoning, China. He got his B.S degree from the Department of Electronic Science and Technology of Tianjin University in 2010. He was an exchange student to the University of Hong Kong from 2008 to 2009. He got his M.S. degree from the Department of Electrical Engineering at the University of Texas at Austin in 2012, in which he was involved in the research of FEM simulations and Integrated battery-charging circuits for MEMS. During his PhD study, he developed complete temporal coupled-mode theory involving dual polarizations, response theory of acoustic force, weak-form expressions of topological optics, and parallel Helmholtz-Hodge decomposition of periodic vector fields, etc. He also programmed automatic and parallel work flow of running FEM and FDTD simulations on distributed computing system and supercomputer of Texas Advanced Computing Center for various mechanically variable systems: ranging from optical fiber, photonic crystal, optical resonator, to piezoelectric materials and mechanical systems.

Permanent email: donghui@utexas.edu

This dissertation was typed by Hui Dong.